

Czech Technical University in Prague
Faculty of Nuclear Sciences and Physical
Engineering

Department of Physics
Study programme: Nuclear and Particle Physics



Performance of plastic scintillators in particle detection

MASTER THESIS

Author: Bc. Vojtěch Zabloudil
Supervisor: Solangel Rojas Torres, Ph.D.
Year: 2023

České vysoké učení technické v Praze
Fakulta jaderná a fyzikálně inženýrská

Katedra fyziky
Studijní program: Jaderná a částicová fyzika



Výkonnost plastových scintilátorů při detekci částic

DIPLOMOVÁ PRÁCE

Vypracoval: Bc. Vojtěch Zabloudil
Vedoucí práce: Solangel Rojas Torres, Ph.D.
Rok: 2023



DIPLOMA THESIS ASSIGNMENT

Academic year: 2022/2023

Student: Bc. Vojtěch Zabloužil

Study programme: **Nuclear and particle physics**

Thesis title: Výkonnost plastových scintilátorů při detekci částic
(in Czech)

Thesis title: Performance of plastic scintillators in particle detection
(in English)

Language of the Thesis: English

Instructions:

- 1) Research the following topics:
 - properties of scintillation materials relevant for FDD at LHC
 - methods used to study plastic scintillators
- 2) Production and characterisation of polymer composites of CsPbBr₃ nanocrystals
- 3) Characterisation and performance evaluation of plastic scintillators
- 4) Performance of FDD at LHC during Run 3

Recommended literature:

- [1] G. F. Knoll, Radiation Detection and Measurement, WILEY (2010)
- [2] K. Aamodt et al. (ALICE Collaboration), The ALICE experiment at the CERN LHC, JINST 3 (2008), S08002
- [3] K. Děcká et al., Timing performance of lead halide perovskite nanoscintillators embedded in a polystyrene matrix, J. Mater. Chem. C, 2022, 10, 12836
- [4] M. Slupecki, Fast Interaction Trigger for ALICE upgrade, NIM-A, 2022, 9, 167021
- [5] J. Wetzel et al., Radiation damage and recovery properties of common plastics PEN (Polyethylene Naphthalate) and PET (Polyethylene Terephthalate) using a ^{137}Cs gamma ray source up to 1 MRad and 10 MRad, JINST 11.08 (2016), P08023

Name and affiliation of the supervisor:

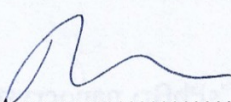
Solangel Rojas Torres, Ph.D.

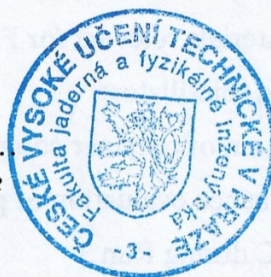
Department of Physics, Faculty of Nuclear Sciences and Physical Engineering of the CTU in Prague

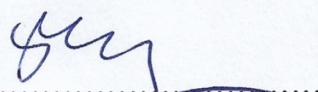
Date of the assignment: 20.10.2022

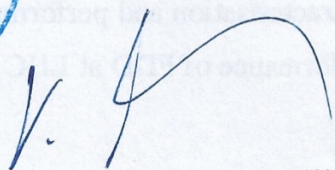
Due date of the thesis: 03.05.2023

The assignment is valid for two years since the date of the assignment.


.....
Guarantor of the study programme




.....
Department head


.....
Dean

In Prague on 20.10.2022

ZADÁNÍ DIPLOMOVÉ PRÁCE

Akademický rok: 2022/2023



Student: Bc. Vojtěch Zabloudil

Studijní program: Jaderná a částicová fyzika

Název práce: Výkonnost plastových scintilátorů při detekci částic
(česky)

Název práce: Performance of plastic scintillators in particle detection
(anglicky)

Jazyk práce: Angličtina

Pokyny pro vypracování:

- 1) Vypracujte rešerši na téma:
 - vlastnosti scintilačních materiálů relevantních pro FDD na LHC
 - metody umožňující studium plastových scintilátorů
- 2) Výroba a charakterizace polymerních kompozitů nanokrystalů CsPbBr₃
- 3) Charakterizace a stanovení výkonnosti plastových scintilátorů
- 4) Studium výkonnosti detektoru FDD na LHC při běhu 3

Doporučená literatura:

- [1] G. F. Knoll, Radiation Detection and Measurement, WILEY (2010)
- [2] K. Aamodt et al. (ALICE Collaboration), The ALICE experiment at the CERN LHC JINST 3 (2008) S08002
- [3] K. Děcká et al., Timing performance of lead halide perovskite nanoscintillators embedded in a polystyrene matrix, J. Mater. Chem. C, 2022, 10, 12836
- [4] M. Slupecki, Fast Interaction Trigger for ALICE upgrade, NIM-A, 2022, 9, 167021
- [5] J. Wetzel et al., Radiation damage and recovery properties of common plastics PEN (Polyethylene Naphthalate) and PET (Polyethylene Terephthalate) using a ^{137}Cs gamma ray source up to 1 MRad and 10 MRad, JINST 11.08 (2016), P08023

Jméno a pracoviště vedoucího diplomové práce:

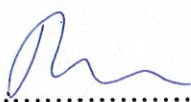
Solangel Rojas Torres, Ph.D.

Katedra fyziky, Fakulta jaderná a fyzikálně inženýrská ČVUT v Praze

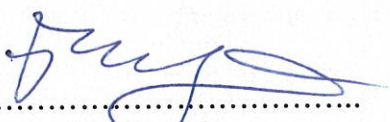
Datum zadání diplomové práce: 20.10.2022

Termín odevzdání diplomové práce: 03.05.2023

Doba platnosti zadání je dva roky od data zadání.


.....
garant studijního programu




.....
vedoucí katedry


.....
děkan

V Praze dne 20.10.2022



PROHLÁŠENÍ

Já, níže podepsaný

Jméno a příjmení studenta: Vojtěch Zabloudil
Osobní číslo: 486301
Název studijního programu (oboru): Jaderná a částicová fyzika

prohlašuji, že jsem diplomovou prací s názvem:

Výkonnost plastových scintilátorů při detekci částic

vypracoval samostatně a uvedl veškeré použité informační zdroje v souladu s Metodickým pokynem o dodržování etických principů při přípravě vysokoškolských závěrečných prací.

V Praze dne 28.4.2023

Zabloudil
.....

podpis

Acknowledgements

I would like to express my gratitude to my supervisor Solangel Rojas Torres, Ph.D. for his guidance, constructive comments and friendly attitude. I would also like to thank prof. Jesús Guillermo Contreras Nuño, Ph.D. for his valuable comments, advice and language corrections. My thanks goes also to other colleagues, namely: Dr. Ildfonso León Monzón, Ing. Jan Král, and Dr. Arvind Khuntia for fruitful discussions.

Finally, I would like to thank my family and friends for their enduring support, in particular my fiancée, my parents and my siblings.

Bc. Vojtěch Zabloudil

Title:

Performance of plastic scintillators in particle detection

Author: Bc. Vojtěch Zabloužil

Study programme: Nuclear and Particle Physics

Sort of project: Master thesis

Supervisor: Solangel Rojas Torres, Ph.D.
Department of Physics, Faculty of Nuclear Sciences and Physical
Engineering, Czech Technical University in Prague

Abstract: Plastic scintillators are widely used in high-energy physics for particle detection. One example is the Forward Diffractive Detector (FDD), a sub-system of the newly-added trigger detector Fast Interaction Trigger (FIT), which was incorporated to the ALICE apparatus during a major upgrade for Runs 3 and 4. This work discusses the commissioning of the FDD and evaluates its performance in Run 3. In order to fulfill the increasing requirements on future scintillators such as ultrafast time response, low cost and good radiation hardness, novel materials and technologies need to be developed. To this end, the production of custom-made scintillators with inorganic CsPbBr₃ nanocrystals embedded in organic polystyrene and silicone matrices is discussed. As part of this thesis, a test bench was set up to use cosmic-ray muons to characterise the samples and study their performance.

Key words: scintillator performance, FDD, trigger, ALICE, quantum dots

Název práce:

Výkonnost plastových scintilátorů při detekci částic

Autor: Bc. Vojtěch Zabloudil

Studijní program: Jaderná a částicová fyzika

Druh práce: Diplomová práce

Vedoucí práce: Solangel Rojas Torres, Ph.D.

Katedra fyziky, Fakulta jaderná a fyzikálně inženýrská, České vysoké učení technické v Praze

Abstrakt: Plastové scintilátory jsou často používány ve fyzice vysokých energií pro detekci částic. Jedním z příkladů je Dopředný Difrakční Detektor (FDD), subsystém nově přidaného spouštěcího detektoru Fast Interaction Trigger (FIT), který byl přidán k detektoru ALICE během vylepšení pro běhy 3 a 4. Tato práce pojednává o zprovoznění FDD a hodnotí jeho výkonnost v běhu 3. Aby bylo možné splnit rostoucí požadavky na budoucí scintilátory, jako je ultrarychlá časová odezva, nízká cena a dobrá radiační odolnost, je třeba vyvinout nové materiály a technologie. Za tímto účelem je diskutována výroba vlastních scintilátorů s anorganickými nanokrystaly CsPbBr_3 zabudovanými v organických polystyrenových a silikonových maticích. Námi vyrobené scintilátory jsou charakterizovány pomocí nově zřízené testovací lavice, která využívá mionů z kosmických spršek ke studiu jejich výkonnosti.

Klíčová slova: výkonnost scintilátorů, FDD, trigger, ALICE, kvantové tečky

Contents

Preface	xvii
1 The ALICE apparatus at the CERN LHC	1
1.1 The Large Hadron Collider at CERN	1
1.2 Motivation for ALICE	1
1.3 Layout	2
1.4 Upgrade for Runs 3 and 4	3
1.5 The Fast Interaction Trigger	3
1.5.1 The FT0	4
1.5.2 The FV0	4
1.5.3 The Forward Diffractive Detector	5
1.5.4 Properties of the FDD scintillators and PMTs	9
2 Scintillation materials and photodetectors	11
2.1 Organic scintillation materials	12
2.1.1 Scintillation mechanism for organic scintillators	12
2.1.2 Emission and absorption spectra	14
2.1.3 Plastic scintillators	15
2.1.4 Liquid scintillators	15
2.1.5 Crystalline scintillators	15
2.1.6 Light yield	15
2.1.7 Time response	16
2.1.8 Radiation hardness and stability	17
2.2 Inorganic scintillation materials	18
2.2.1 Scintillation mechanism for inorganic scintillators	18
2.2.2 Time response	19
2.2.3 Radiation hardness and stability	19
2.3 Nanomaterials	19
2.3.1 Quantum dots	21
2.3.2 Lead halide perovskite nanocrystals	22
2.4 Hybrid materials and nanocomposites	24
2.4.1 Introduction	24
2.4.2 Nanocomposites	24
2.4.3 Preparation of the nanocomposites	24
2.4.4 Matrix polymerisation	25
2.5 Photodetectors	26
2.5.1 Photomultiplier tubes	26
2.5.2 Time response	27
3 Custom made scintillator samples	29

3.1	CsPbBr ₃ nanocrystal production and characterisation	29
3.1.1	CsPbBr ₃ nanocrystal synthesis	29
3.1.2	Ligand exchange	31
3.1.3	CsPbBr ₃ nanocrystal characterisation	32
3.2	Composite production	34
3.2.1	Polystyrene matrix	35
3.2.2	Composites with CsPbBr ₃ nanocrystals	35
3.2.3	Silicone matrix	37
3.2.4	Silicone mould for polystyrene samples	38
3.2.5	Composites with CsPbBr ₃ nanocrystals	39
3.2.6	Composites with PPO	40
3.3	Summary of the produced samples	40
3.4	Polishing and wrapping of the samples	40
4	Design and implementation of a test bench	47
4.1	General idea and purpose	47
4.2	Description of the set-up	48
4.2.1	Custom 3D printed module	48
4.2.2	Dark box	48
4.2.3	Read-out electronics	48
4.3	Generation of the signal	51
4.3.1	Irradiation with vertical cosmic-ray muons	51
4.3.2	Irradiation with a laser	52
4.4	Set-up for a test with cosmic-ray muons	52
5	Peformance of the custom-made scintillators	55
5.1	Scintillator characterisation	55
5.2	Scintillator characterisation with cosmic-ray muons	56
5.2.1	Experimental set-up and data-taking details	56
5.2.2	Analysis of the raw data	56
5.2.3	Data analysis	58
5.2.4	Coincidence selection	58
5.2.5	Charge distribution	59
5.3	Scintillator performance based on their composition	60
5.3.1	Polystyrene matrix	61
5.3.2	Silicone matrix	62
5.4	Scintillator performance based on the PMT supply voltage	66
5.5	Summary and outlook	66
6	Peformance of the FDD	69
6.1	Commissioning of the FDD	69
6.1.1	HV calibration with cosmic-ray muons	70
6.2	Performance in proton-proton collisions	72
6.2.1	Stable-beam collisions	72
6.2.2	Bunch crossing (BC) distributions	74
6.2.3	Vertex position	76
6.3	Summary and outlook	77
	Summary and outlook	83
	Bibliography	85

Appendix	90
A Test bench: crosstalk test	91
B Custom-made scintillator characterisation: polystyrene matrix	95
C Custom-made scintillator characterisation: silicone matrix	103
D FDD performance: crosstalk test	111

Preface

This thesis reports on the status of the Forward Diffractive Detector (FDD), a sub-system of the newly-added Fast Interaction Trigger (FIT) detector. FIT was included in the ALICE apparatus and the other upgrades during the Long Shutdown 2 (LS2, 2018-2022), which prepares ALICE for Runs 3 and 4 (2022-2030). During Run 3, the interaction rate is increased to 1 MHz in pp collisions and up to 50 kHz for Pb-Pb collision. The data acquisition (DAQ) and the computing infrastructure were improved to cope with the new scenarios. The increase in interaction rate is motivated by the focus of the ALICE physics programme on rare probes at low transverse momenta. These require improvements in vertexing and tracking efficiency, and due to their very small signal-to-background ratio, they demand a greater data sample size.

In order to fulfill the increasing requirements on future scintillators such as ultrafast time response, low cost and good radiation hardness, novel materials and technologies need to be developed. To this end, this work also reports the production of custom-made scintillators with inorganic CsPbBr₃ nanocrystals embedded in organic polystyrene and silicone matrices. These nanocomposites were produced in collaboration with Universidad Autónoma de Sinaloa (UAS) in Culiacán, Mexico under the supervision of Dr. Ildefonso León Monzón. The characterisation and performance studies of the samples was done with a newly-set up test bench using cosmic-ray muons at the Department of Physics of FNSPE CTU in Prague.

Chapter 1 presents the CERN laboratory, the ALICE apparatus and its layout, highlighting the changes made during the LS2 in preparation for Runs 3 and 4. An overview of the Fast Interaction Trigger (FIT) system is included together with an in-depth description of one of its sub-systems, the Forward Diffractive Detector (FDD).

Chapter 2 brings an introduction to scintillation materials and photodetectors. It contains an overview of scintillators, both organic and inorganic, and discusses their respective scintillation mechanisms and properties such as light yield, time response or radiation hardness. It follows with a section about nanomaterials, in particular the lead halide perovskite quantum dots in which the CsPbBr₃ nanocrystals belong. The production of nanocomposites is further outlined. The chapter finishes with a section about photodetectors, mainly discussing fine-mesh photomultiplier tubes (PMTs).

Chapter 3 shows the production of the custom-made scintillator samples with CsPbBr₃ nanocrystals. It describes the synthesis of the nanocrystals, the subsequent exchange

of the surface ligands and the characterisation of the nanocrystals. The composite production is further presented and explained in more detail for both of the matrices: polystyrene and silicone. The produced samples are summarised at the end of the chapter.

Chapter 4 presents the newly-set up test bench to characterise the scintillator samples and study their performance. It displays the components used in the test bench and the idea behind the design to perform measurements using cosmic-ray muons.

Chapter 5 reports on the characterisation of the custom-made scintillator samples. It describes the used set-up in more detail and explains the techniques of the analysis. The results are presented separately for each of the scintillator matrices. The scintillator performance is studied based on the composition of the samples as well as on the PMT supply voltage.

Chapter 6 studies the FDD performance. It begins with an introduction to the commissioning of the FDD and explains the needed setting-up of the detector, e.g. the high-voltage calibration. Subsequently, the FDD performance in pp stable-beam collisions is discussed. The results include the bunch crossing (BC), charge and time distributions for the whole FDD and also for one of its channels only. An illustration of the vertex position determination is provided.

The text concludes with a summary and an outlook of plans. In addition there are several appendices discussing the crosstalk test in more detail as well as the full results of the custom-made scintillator samples.

Chapter 1

The ALICE apparatus at the CERN LHC

This chapter provides general information about the ALICE detector at the CERN LHC, mainly the ALICE upgrade for Runs 3 and 4. It includes an in-depth overview of the Forward Diffractive Detector.

1.1 The Large Hadron Collider at CERN

The European Organisation for Nuclear Research (CERN) is one of the world's largest laboratories focusing on fundamental research. This international collaboration consisting of 23 member states and several other associate member states is located in the Franco-Swiss border near Geneva. It uses powerful particle accelerators (e.g. the LHC) which accelerate beams to high energies and further collide them with either another high-energy beam or a stationary target. During and after the collision, a wide spectrum of products can be studied by particle detectors such as ALICE, ATLAS, CMS or LHCb, which are all placed along the LHC.

The Large Hadron Collider (LHC) is the world's largest and the most powerful particle accelerator. It is a 27-kilometre ring synchrotron accelerator, which consists of thousands of magnets used to steer and shape the beam as well as a number of radio-frequency cavities boosting the particle energy up to 6.8 TeV for proton beams. However, in order to achieve such high energies, the LHC is only a part of the accelerator complex at CERN, which is shown in Fig. 1.1. The energy of the particles increases gradually as they transfer from smaller accelerators up to the LHC.

1.2 Motivation for ALICE

A Large Ion Collider Experiment (ALICE) is a general-purpose heavy-ion detector, one of the four large detectors at the CERN LHC. It focuses on studies of strongly

The CERN accelerator complex *Complexe des accélérateurs du CERN*

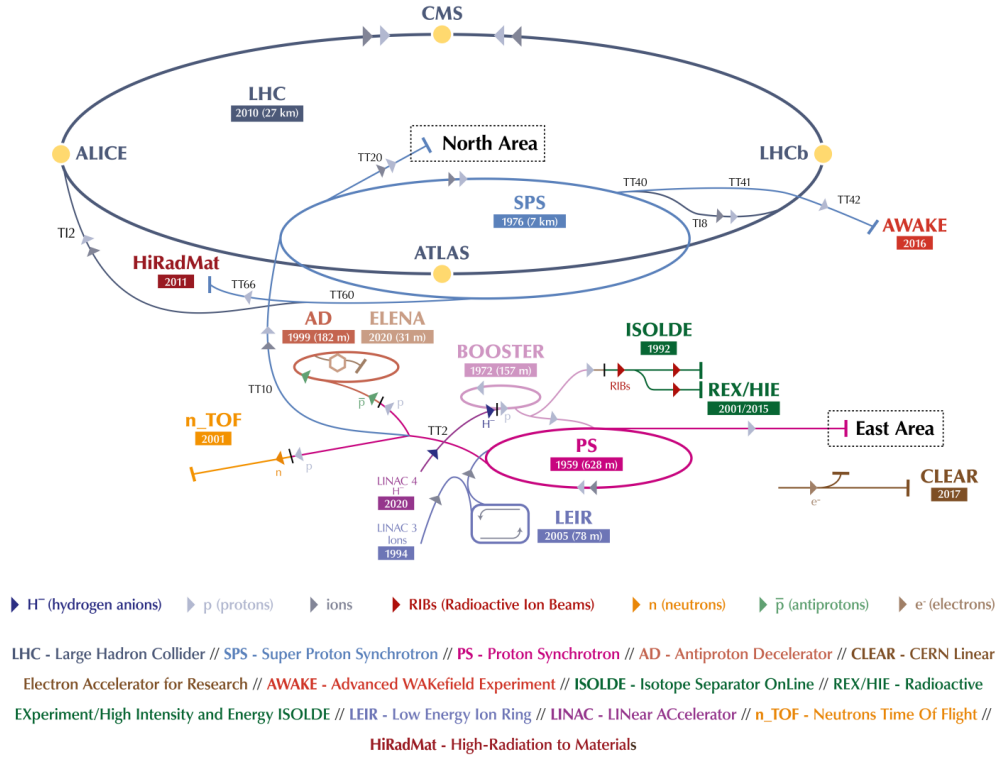


Figure 1.1: The CERN accelerator complex. Figure taken from Ref. [1].

interacting matter, i.e. quantum chromodynamics (QCD), which are performed with heavy-ion collisions of Pb-Pb or Xe-Xe, which are delivered by the LHC. In order to vary the energy density and to provide reference data, proton-proton (pp) and proton-nucleus (e.g. p-Pb) collisions are also used [2].

1.3 Layout

The layout of the ALICE detector for Run 3 is shown in Fig. 1.2. The detector consists of two main parts: a central barrel and a muon arm. The former is used to track and measure hadrons, electrons and photons. The latter, located at forward rapidities, focuses on tracking and measuring muons.

The central barrel consists of the Inner Tracking System (ITS) and Time Projection Chamber (TPC), which provide primary and secondary vertex reconstruction and particle identification. The Transition Radiation Detector (TRD) is also used for tracking as well as for particle identification (PID). Other detectors providing PID are the Time Of Flight (TOF), High Momentum Particle Identification Detector (HMPID) and Charge Particle Veto (CPV). The calorimetry is provided by the

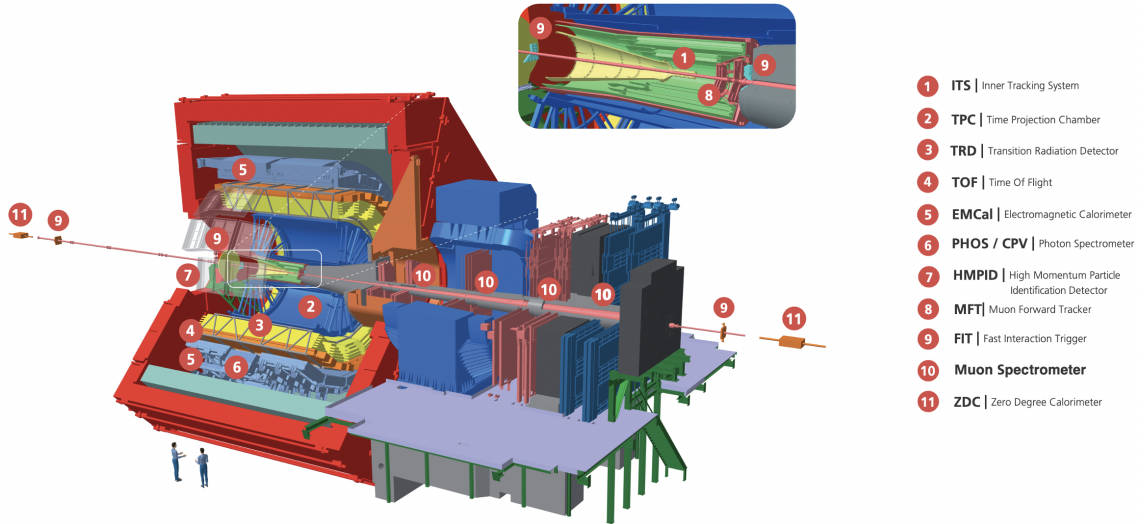


Figure 1.2: A schematic drawing of the ALICE detector layout for Run 3.

Electromagnetic Calorimeter (EMCal) and the Photon Spectrometer (PHOS).

The muon arm consists of the Muon Forward Tracker (MFT), muon absorbers and the Muon Spectrometer.

The Fast Interaction Trigger (FIT) is the main trigger system contributing to many other tasks and it is further described in the following sections.

1.4 Upgrade for Runs 3 and 4

During the Long Shutdown 2 (LS2), ALICE underwent major improvements of the system featuring the addition of the new Muon Forward Tracker (MFT) and the Fast Interaction Trigger (FIT), the upgrade of the Inner Tracking System (ITS) and the Time Projection Chamber (TPC) as well as the new Online-Offline (O2) computing infrastructure and the new Central Trigger Processor (CTP). The upgrade reflects the aims of the ALICE physics programme for Runs 3 and 4, which focuses mainly on rare probes such as heavy-flavour particles, quarkonia, photons, and jets at low momenta. Nevertheless, such events present difficulties for their selection and trigger, which drive the need for the implementation of the continuous read-out with an expected rate of 50 kHz for Pb-Pb collisions and up to 1 MHz for pp and p-Pb collisions [3].

1.5 The Fast Interaction Trigger

The Fast Interaction Trigger (FIT) is a key element in ALICE after the upgrade for Runs 3 and 4. FIT consists of three sub-systems: FT0, FV0 and FDD, each devoted to different functions and operational regimes. All FIT sub-detectors use

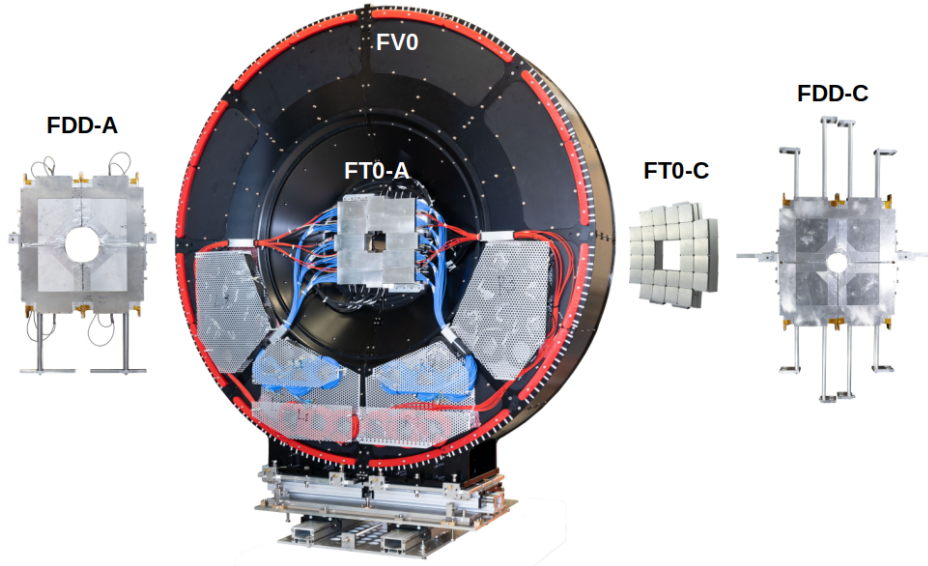


Figure 1.3: Layout of the Fast Interaction Trigger, components are not up to scale. Courtesy of W. H. Trzaska.

newly-developed common front end electronics (FEE) and detector control system (DCS). The layout of FIT is shown in Fig. 1.3.

1.5.1 The FT0

The FT0 is a set of two fast Cherenkov detector arrays FT0-A and FT0-C equipped with XP85002/FIT-Q micro channel plate photomultiplier tubes (modified Planacon XP85012) with excellent time resolution as low as 13 ps [4, 5, 6]. The detector arrays are located on both sides of the interaction point, along the beam direction, and consist of 28 detector modules for FT0-C and 24 modules for FT0-A, respectively. Each of the detector modules has 4 outputs, each collecting charge from a quarter of the sensor area, while the original Planacon XP85012 photosensor features 64 outputs. The FT0 plays a leading role in the generation of low-latency and minimum-bias trigger and in calculations of collision time and vertex [3, 7].

1.5.2 The FV0

The FV0 is a large scintillator-based detector divided into 5 rings each with 8 sectors corresponding to a total of 48 channels (each sector of the outermost ring is read out by two photosensors instead of one for the others). It is suitable for background monitoring and improves minimum-bias and centrality trigger. Pairing up with the FT0, it significantly contributes to the centrality and event plane determination [3, 7].

1.5.3 The Forward Diffractive Detector

The Forward Diffractive Detector (FDD) is a scintillation-based detector covering the forward pseudorapidity range [8]. It is a successor of the ALICE Diffractive (AD) detector [9], which was part of ALICE for Run 2. The main difference is the use of much faster materials, the implementation of the laser calibration system and the newly-developed front-end electronics and detector control system [10]. The construction of the FDD is described in detail in my bachelor thesis [11].

FDD is essential for tagging exclusive diffractive processes by providing a veto on the activity at forward rapidities [12]. It is used to tag dissociative diffractive processes by detecting activity in events with rapidity gaps. It also contributes to other technical tasks such as background monitoring using the arrival times of the particles to the detector, luminosity, and centrality determination.

Layout

FDD is divided into two stations: FDD-A and FDD-C which are located at distances of 17 m and 19.5 m from the interaction point along the beamline, respectively. The pseudorapidity coverage is from 4.8 to 6.3 for FDD-A and from -7.0 to -4.9 for FDD-C. The schematic drawing of one FDD station is shown in Fig. 1.4.

Each station is made of two layers of plastic scintillators further subdivided into four quadrants accounting for a total of 16 channels. For each quadrant, there is a plastic scintillator connected to a pair of wavelength-shifting (WLS) bars that collect the light produced by the scintillator. The light is further transferred via optical fibres to a photomultiplier tube (PMT), where it is converted into corresponding electrical signal.

The size of one scintillator pad is $216 \times 181 \times 25$ mm³. The WLS bars measure $242 \times 4 \times 25$ mm³ and $182 \times 4 \times 25$ mm³ for the FDD-A, and $242 \times 4 \times 25$ mm³ and $207 \times 4 \times 25$ mm³ for the FDD-C, respectively. The FDD-A uses optical fibres with a length of 57 cm and 1 m, while the FDD-C uses optical fibres with a length of 3 m. The length difference of the fibres arises from the difference between the positioning of the PMT boxes.

The notation of the detector channels is done according to the layout shown in Fig. 1.5. The FDD-C is divided into layers 0 and 1, while the FDD-A is divided in layers 2 and 3, each subdivided into 4 quadrants. The naming convention, which is standardised amongst ALICE, is to start from the positive values along the x and y axis with number 0 and increase the number counter-clockwise when looking from the interaction point towards the C side. On the A-side, the convention is to increase the numbering clockwise in order to obtain mirror symmetry for sub-detectors with x, y plane symmetry. In this way, each detector channel has a specific number made up from the layer number, which stands first and the quadrant number, which stands second, e.g. channel 0_1 refers to the pad in the layer 0 and in quadrant 1.

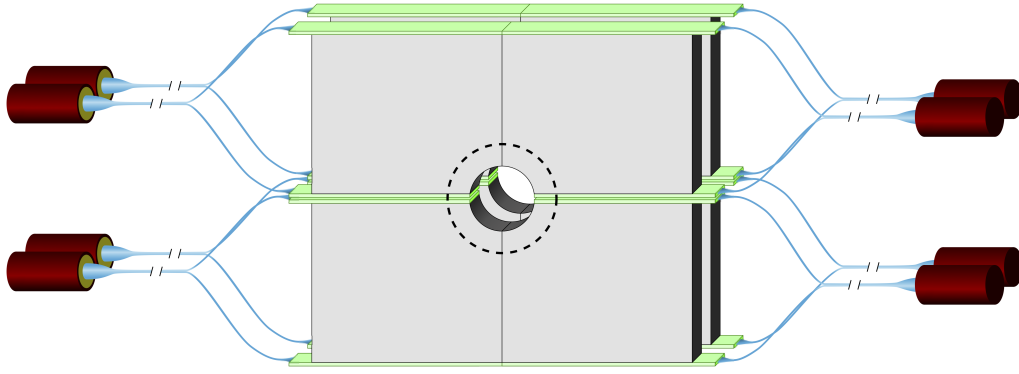


Figure 1.4: Schematic drawing of station FDD-C: the plastic scintillator pads are shown in grey, the WLS bars in green, the optical fibre bunches in blue and the PMTs in dark red. The only differences with respect to the station FDD-A are that the inner hole is larger for FDD-A as depicted by the black dashed line and the length of the fibre bunches. Figure taken from Ref. [13].

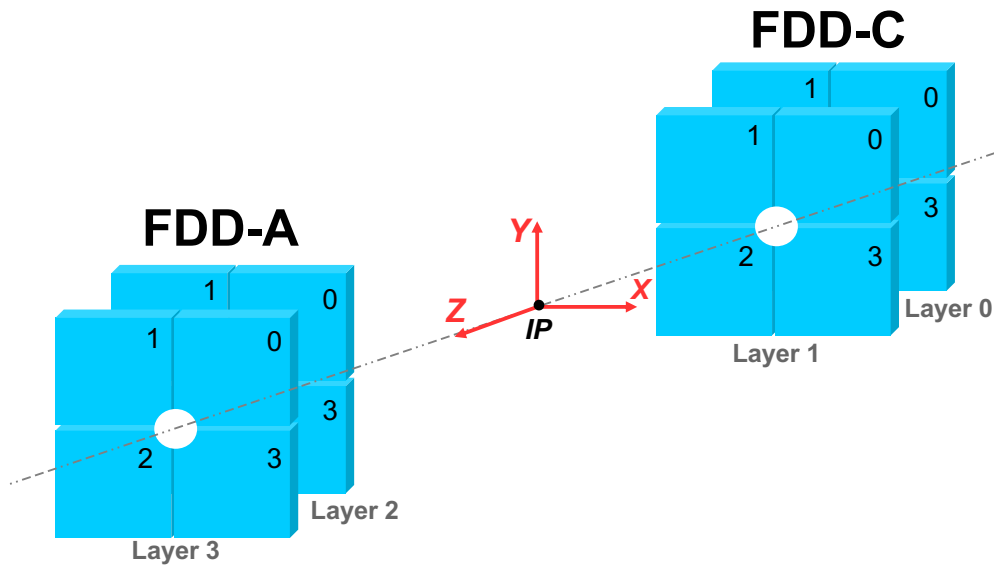


Figure 1.5: Schematic drawing of the FDD layout with the notation of the detector channels.

Laser calibration system

Plastic scintillators often suffer from performance loss when exposed to extreme radiation environments. To compensate for this, an increased high voltage can be applied to the PMTs to get a matching signal. For this purpose, the laser calibration system (LCS) was added to FIT to study the detector performance and ageing over

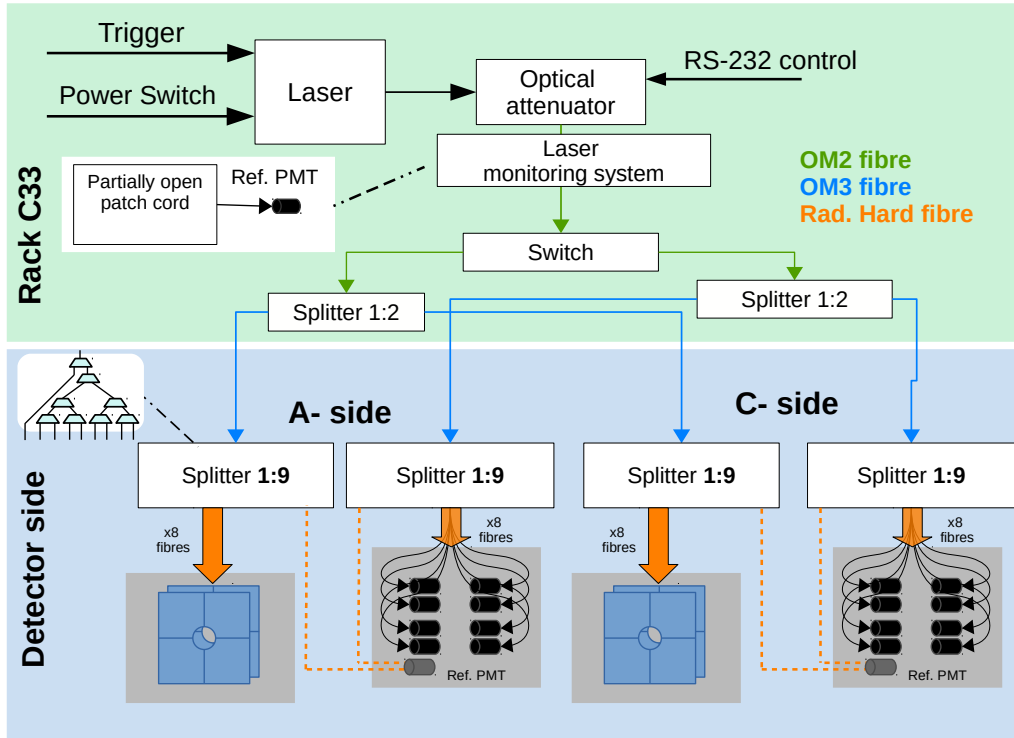


Figure 1.6: The scheme of the FDD laser calibration system.

long periods of time. It uses optical fibres connected to each of the PMTs and scintillators of the set-up. Such configuration provides a way to study the properties of the laser signal coming through the optical fibre from the scintillator and compare it with the light signal applied directly to the PMT.

The scheme of the FDD LCS is shown in Fig. 1.6. The system begins with a PLD 800-D laser driver and LDH-P-C-405-M laser head with wavelength of emission of 405 nm. The amplitude of the laser signal is lowered by a controllable optical attenuator in order to regulate the laser intensity when irradiating either the scintillator pads or directly the PMTs. A laser monitoring system consisting of a partially open fibre and a reference PMT is included to monitor the performance and stability of the laser itself. The LCS features a switch to change between the irradiation of the scintillator pads and the irradiation of the PMTs as explained above. After the switch, the laser is then split into two branches using a 1:2 optical splitter, where one of the branches travels to the A-side, while the other one travels to the C-side. The branching is the same for both the scintillators and the PMTs. Once the fibres reach the respective sides, they are finally splitted in a 1:9 way in a splitter box, whose design is the same for all 4 ends (A-side scintillators, A-side PMTs, C-side scintillators, and C-side PMTs). Eight of the 9 fibres are coupled to the corresponding channels, while the ninth is used for reference.

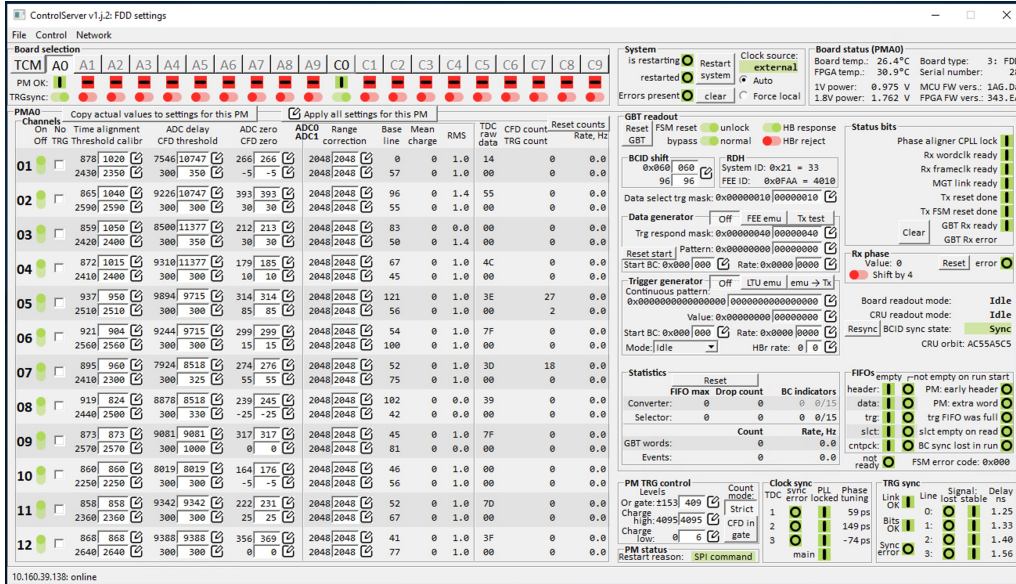


Figure 1.7: The layout of the Processing module (PM) control panel.

Front-end electronics

FDD uses the same front-end electronics (FEE) scheme as the other two FIT sub-detectors. It was designed for continuous read-out, to provide low latency trigger, and allows for excellent time resolution.

The FEE consists of Processing Modules (PM) with 12 signal inputs for fast digitisation of the charge and time, together with Trigger and Clock Modules (TCM), which are dedicated to generating the low latency trigger. The goal of the FEE is to complete the entire signal processing and to generate the trigger in under 425 ns for the level minus trigger (LM) provided by the FT0 and FV0, while FDD delivers level 0 trigger (L0) due to the distant position from the interaction point [14].

The PMs receive analog input signals from the PMTs and calculate the charge and time of the signal. The charge of the signal is calculated using two integrators (one for even bunches and the other one for odd bunches) and converted into digital information with an analog-to-digital converter (ADC). The integrators are integrating the charge in an position-adjustable 5 ns window inside a 25 ns interval defined by the LHC clock. The timing of the signal is calculated with a constant fraction discriminator (CFD) regardless of the position of the signal within the 25 ns interval. A screenshot of the PM control panel is shown in Fig. 1.7. Multiple different parameters for each channel individually can be set, namely: time alignment, threshold calibration, ADC delay, CFD threshold, ADC zero and CFD zero. Their proper setting requires multiple calibrations and understanding to achieve the correct calculation of the time and charge measured by the channel.

The information from the PM is sent to the TCM, where a Field Programmable Gate Array (FPGA) can generate five different trigger signals. If an event is registered in any PMT of FDD-A or FDD-C, the FDDorA or FDDorC trigger is formed,

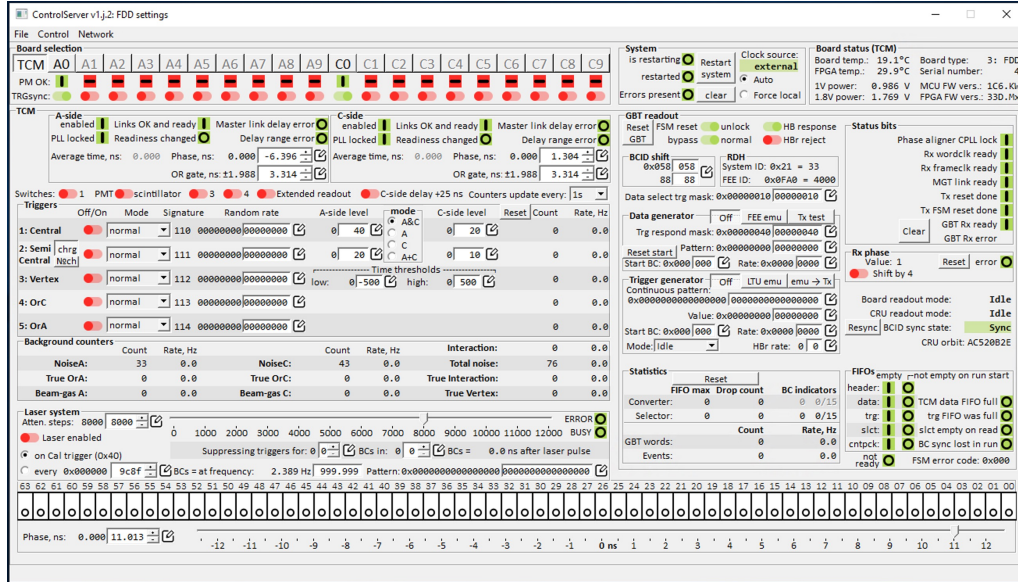


Figure 1.8: The layout of the Trigger and Clock Module (TCM) control panel.

respectively. If the signal from FDD-A and FDD-C comes within a certain time difference, a vertex trigger FDDVertex is formed. If the total measured charge value is higher than the central or semi-central threshold for one or both sides of FDD, a central or semi-central trigger is formed. A screenshot of the TCM control panel is shown in Fig. 1.8, where e.g. the rates of the formed triggers are displayed in real time.

Detector control system

FDD is operated via the Detector Control System (DCS) [10], which is integrated with the other FIT sub-detectors. It comprises control panels to configure, adjust and control the high voltage of all channels, FEE and LCS. In this way, the detector can be configured to operate accordingly to the type of run (cosmics, pp, p-Pb or Pb-Pb collisions). The main DCS control panel is shown in Fig. 1.9.

1.5.4 Properties of the FDD scintillators and PMTs

FDD uses the BC-420 scintillator by Bicron, which is specifically dedicated for ultra-fast timing and counting applications. The BC-420 has a base of polyvinyltoluene with a refractive index of 1.58. The stated rise time is 0.5 ns, the decay time is 1.5 ns, the FWHM is 1.3 ns, the wavelength of maximum emission is around 385 nm, and the attenuation length (the distance by which the light is attenuated to $1/e$) is 140 cm [15].

As for the WLS bars, FDD uses the newer and faster technology of NOL [16], as implemented in the BC-499-90 bars by Bicron that contain NOL-38 wavelength

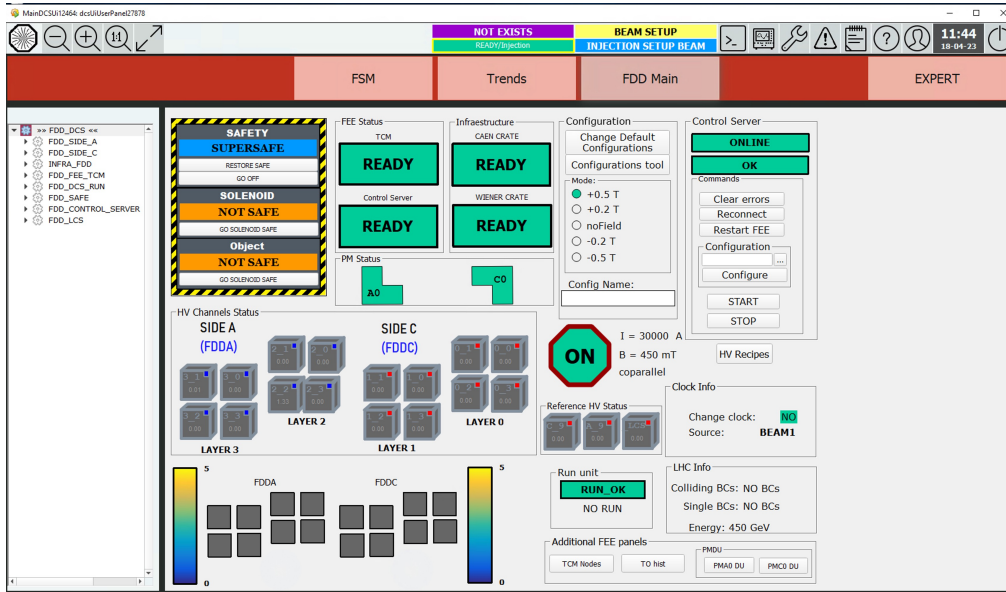


Figure 1.9: The layout of the main FDD DCS control panel.

shifter by LuminnoTech. The absorption and emission spectra of these scintillators is shown in Fig. 2.2. As can be seen in the figure, the peak of the absorption spectra of NOL-38 matches the peak of the emission spectra of BC-420 making it a highly efficient WLS. They offer a decay time of only 0.95 ns. The absorption length is 382 nm with luminescence length of 431 nm and 458 nm; FWHM is 69 nm and the photoluminescence quantum yield (PLQY) is 88 % [17].

FDD uses the Hamamatsu H8409-70 photomultiplier tube assembly with a built-in PMT R7761-70. It contains a fine-mesh dynode structure (with 19 dynode stages) designed specifically for operation in high magnetic fields, which also shows excellent output linearity. The overall gain of the PMT is 1×10^7 . Its photocathode is round with a diameter of 27 mm and made of bialkali. The absorbance spectrum ranges from 300 nm to 650 nm with a peak at 420 nm [18].

Chapter 2

Scintillation materials and photodetectors

The following chapter provides some basic information about scintillators in general and explains their division into organic and inorganic scintillators listing their pros and cons. A brief introduction into nanomaterials is included with an emphasis on quantum dots and lead halide perovskite nanocrystals. The chapter continues with a mention of photomultiplier tubes, mainly the fine-mesh type.

General properties

Scintillators are materials showing the property of luminescence when excited by ionising radiation. Luminescence corresponds to the emission of light arising from a radiative transition between an excited energy state to a less excited or relaxed state of matter. The ionising radiation can take many forms such as X-rays, γ -rays, neutrons, electrons or α particles [19]. If the material is excited by an X-ray or a γ -ray, the scintillation is referred to as radioluminescence (RL), if the excitation comes from the visible or the UV part of the spectra, it is called photoluminescence (PL). Scintillators are, in conjunction with photomultiplier tubes, widely used in high energy physics, medicine, and in other industries.

The scintillation materials can be classified into two groups: organic scintillators and inorganic scintillators. The organic scintillators are often used today for their fast response (few ns), low cost and ease of manufacture. The inorganic scintillators were historically preferred for their high light output and linearity; however, their response time is generally relatively slow (tens of ns) and the cost of their production is rather high. Due to these reasons, it is desirable to substitute them with more inexpensive alternatives.

One of such alternatives is to use relatively affordable inorganic nanoparticles that show the phenomenon of quantum confinement. Quantum confinement leads to a potential of having an extremely fast subnanosecond response, which could change many technological fields drastically. For example, the use of ultrafast inorganic scintillators could lower the coincidence time resolution of positron emission tomography

(PET) scanners to 10 ps (today’s limits are 214 ps [20]). With such resolution, it would be possible to construct a time of flight positron emission tomography (TOF-PET), which would improve the signal-to-noise ratio and the precision of today’s imaging [21]. Additionally, the cost and the time needed for this medical treatment would be significantly reduced, which leads to a much lower exposure of human tissue to ionising radiation. Furthermore, the TOF-PET could provide the possibility of real-time imaging and reduce the time-consuming algorithms for reconstruction that are used today [22].

2.1 Organic scintillation materials

Organic scintillators can be further subdivided into three main forms: plastic scintillators, liquid scintillators and crystalline scintillators. There is a high demand for plastic and liquid scintillators because of their extreme versatility regarding their size and geometry. Together with the relatively low cost, they often represent the only affordable choice for large-volume detectors [23]. Before discussing each of the three forms separately in more detail, the common scintillation mechanism for organic scintillators is discussed.

2.1.1 Scintillation mechanism for organic scintillators

The organic scintillator molecules are endowed with symmetry properties giving rise to a π -electron structure. The transitions between the energy levels of a molecule cause the material to produce visible light, also known as luminescence. A sketch of the corresponding π -electron excitation levels in an organic molecule is shown in Fig. 2.1.

Nearly all molecules occupy the S_{00} state at room temperature T due to small average thermal energies around $kT = 0.025$ eV, where k denotes the Boltzmann constant and $T = 20$ °C. These energies are much lower than the spacing between the vibrational states (around 0.15 eV) and hence they are not able to excite the molecule in a higher state. The molecules however can be excited to higher singlet states S_1 , S_2 or S_3 (for spin 0) with energy spacing in the order of few eVs by a nearby-passing ionising radiation.

After the excitation, higher singlet states rapidly de-excite to the S_1 state through internal conversions. The vibrational level states lose energy due to the establishment of thermal equilibrium. Therefore, the net effect of the excitation after a few picoseconds are excited molecules in the S_{10} state, which themselves emit the scintillation light in three ways. Due to its short decay time, prompt fluorescence is the main and the most desired way of emission. It emerges from the de-excitation of molecules in the S_{10} state to one of the vibrational states of the ground state. The intensity of the prompt fluorescence at a time t behaves as

$$I(t) = I_0 e^{-t/\tau}, \quad (2.1)$$

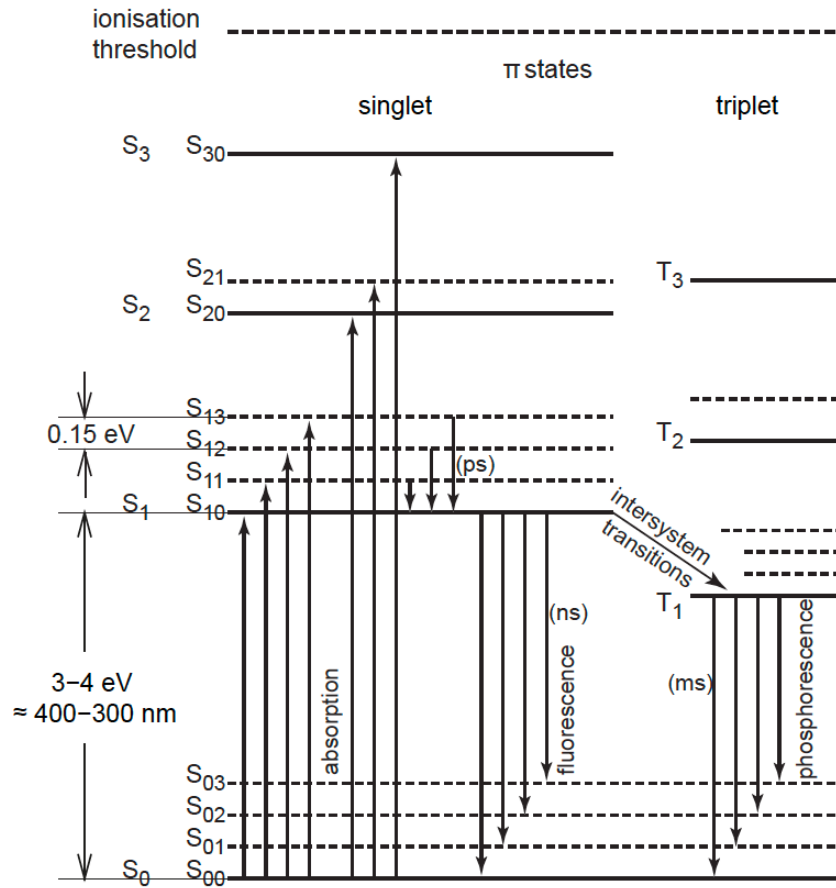


Figure 2.1: Energy levels of the π -electrons in an organic molecule. S_0 represents the ground states; S_1, S_2, S_3 are the excited singlet states and T_1, T_2, T_3 are the excited triplet states. S_{ij} and T_{ij} are vibrational sub-level states. Figure taken from Ref. [24].

where τ is the fluorescence decay time, which is for most organic scintillator molecules in the order of nanoseconds.

The other ways of emission include the singlet states conversion through inter-system crossing into triplet states, which have much longer decay times. The second way, called phosphorescence, emerges from de-excitation of T_1 triplet state to the ground singlet state S_0 with transition times as long as milliseconds. Since the triplet state T_1 lies below the singlet state S_1 , hence the energy difference between the T_1 state and the ground state S_0 is less, the phosphorescence spectrum has a longer wavelength. Due to thermal excitation, some of the molecules in T_1 state may return to the state S_1 creating delayed fluorescence. The spectrum of the delayed fluorescence remains the same as for fluorescence, but the decay time is much longer.

2.1.2 Emission and absorption spectra

An absorption spectrum of a scintillator represents the ability of incident radiation of a given wavelength to excite the scintillator. On the other hand, an emission spectra shows the distribution of the wavelengths of the emitted photons from the scintillation mechanism. The difference of the maxima of the absorption and the emission spectra is often called the Stokes shift and it represents the measure of the overlap of the spectra.

An overlap between the absorption and emission spectra of a given scintillation material is caused by the fact that the photons created by the de-excitation from the S_{10} state to the ground state provide enough energy to again excite the molecule to a higher state. For this reason, it is desired to have a scintillator with an overlap as small as possible between the emission and the absorption spectra to avoid self-absorption. A frequently used technique to increase the transparency of the emitted scintillation photons in the scintillator is to add a small amount of another scintillator component called the wavelength shifter (WLS). The molecules of the WLS, which typically show large Stokes shifts, will absorb the emitted photons and subsequently emit them with smaller energy hence longer wavelength. These are not absorbed by the material, because their energy is not sufficient to excite the molecules of the primary scintillator.

This is illustrated on Fig. 2.2, which shows the absorption and emission spectra for a plastic organic scintillator NOL-38 and the emission spectra for BC-420. In this case, BC-420 is used as a main scintillator material with the NOL-38 being added as an optimal WLS as its absorption spectra matches the emission spectra of the BC-420. Such configuration provides very high transparency and low attenuation lengths. WLS are also typically used to match the peak of the emission spectra of the scintillator detector to the peak of the absorption spectrum of the photocathode within the read-out PMT.

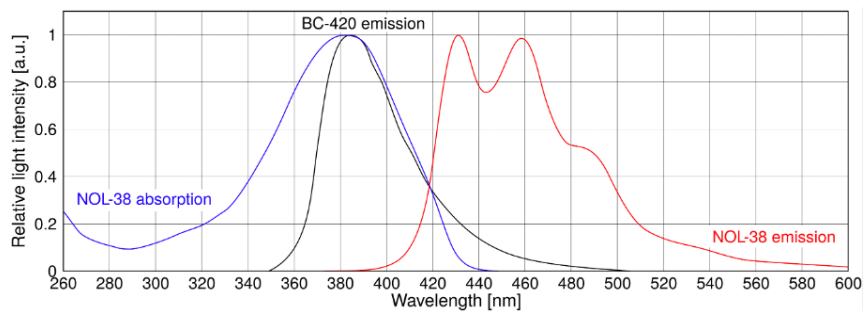


Figure 2.2: The emission spectrum for the BC-420 scintillator together with the absorption and emission spectra of the NOL-38 wavelength shifter. Figure taken from Ref. [13].

2.1.3 Plastic scintillators

The production of plastic scintillators consists of dissolving an organic scintillator in a solvent, which is then subsequently polymerised creating a solid plastic. The solvent, usually called a base or a matrix, is typically a scintillator itself, e.g. polyvinyltoluene or polystyrene and takes up a vast majority (as much as 99 % by weight) of the final product. Multiple other organic scintillator constituents are added to the base to provide the optimal balance between sufficient light yield and low self-absorbance (long attenuation length) in the material as discussed in Sec. 2.1.2. This process provides the possibility to create the scintillators in various sizes and shapes ranging from thin films (thickness of units of μm) to huge volumes (tens of cm to several metres) which are determined by the specific applications.

2.1.4 Liquid scintillators

The production of liquid scintillators is very similar to the production of plastics. Nevertheless, there are some key properties that differentiate plastics and liquids according to their application. For example, liquid scintillators require to be sealed in glass containers to avoid oxygen contamination as it would lead to quenching of the light yield. On the other hand, due to the lack of their solid structure, liquid scintillators are more resistant to ionising radiation, making them a better candidate in environments with high exposure to ionising radiation.

2.1.5 Crystalline scintillators

Pure organic crystals or crystalline scintillators are not widely used today because of their fragility and difficulty to obtain in large sizes. Their scintillation efficiency also depends on the orientation of the ionising radiation with respect to the crystal axes making them unsuitable for measurements of energy resolution. Their advantage in comparison with some pure inorganic crystals is that they are non-hygroscopic, which is the main limitation of NaI(Tl).

2.1.6 Light yield

In general scintillator terminology, the amount of photons emitted by the material is given by the light yield (LY) and the photoluminescence quantum yield (PLQY). The LY is defined as a number of photons emitted per unit of deposited energy in the material and the PLQY is given by the ratio of emitted photons to absorbed photons.

However, in order to understand the light yield of a scintillator, one has to study the energy deposition of a charged particle in the scintillation material. The majority of the kinetic energy deposited in the material is dissipated nonradiatively in the form of lattice vibrations and heat while only a small portion of the energy is irradiated in the form of photons.

The amount of the kinetic energy that is converted into fluorescent energy is called scintillation efficiency and it is in general dependent on the type of the particle interacting with the material and its energy [25]. As a consequence, the term of MeV electron equivalent is introduced to describe the absolute light yield produced by the charged particle. For organic scintillators, the light yield emerged from heavy charged particles (protons or α) is lower than the yield gained from electrons of the same energy. Furthermore, the response to heavy charged particles is nonlinear unlike the linear response for electrons above energies about 125 keV.

In order to describe the response of organic scintillators to charged particles, a relation between the fluorescent energy emitted per unit path length dL/dx and the specific particle energy loss dE/dx is used. For the assumption of no quenching, the light yield is directly proportional to the energy loss as

$$\frac{dL}{dx} = S \frac{dE}{dx}, \quad (2.2)$$

where S denotes the normal scintillator efficiency.

If one assumes that the ionisation created by the charged particle leads to quenching from the affected molecules, it decreases the scintillation efficiency as described by the Birks' formula

$$\frac{dL}{dx} = \frac{S \frac{dE}{dx}}{1 + kB \frac{dE}{dx}}, \quad (2.3)$$

where the density of the damaged molecules is represented by a proportionality constant B while a fraction k leads to quenching [26].

2.1.7 Time response

The time response of a scintillator is typically represented via its decay time τ , which defines the aforementioned intensity of the scintillator light output described by Eq. (2.1). However, such picture is fairly simplified and takes into account only the time response of one luminescence centre directly excited by PL. In reality, the time response is longer due to two other effects. Firstly, the time needed to populate the luminescent states is finite and secondly due to the presence of slower competing processes during the scintillation mechanism such as phosphorescence or delayed fluorescence.

One might assume that the population of the luminescent states is exponential, which leads to the shape of the light pulse given by

$$I(t) = I_0(e^{-t/\tau} - e^{-t/\tau_1}), \quad (2.4)$$

where τ_1 represents the rise time needed for the population and τ represents the decay time. Typical values for commercial organic scintillators are around 0.5 ns for τ_1 and 1-4 ns for τ .

Another approach is to make an assumption that the population of the luminescent states is represented by a Gaussian function $f(t)$ characterised by a standard deviation σ , then the following formula holds

$$\frac{I(t)}{I_0} = f(t)e^{-t/\tau}. \quad (2.5)$$

In consequence, the rise and fall of the light output can be experimentally measured and subsequently characterised by the full width at half maximum (FWHM) of the signal. Such parameter has become a common characteristic of ultrafast organic scintillators rather than their decay time τ . The FWHM of commercial organic scintillators lies around 1.5 ns and less.

2.1.8 Radiation hardness and stability

Organic scintillators suffer from damage caused by ionising radiation during their operation which leads to an efficiency loss of their detection. This damage includes internal effects such as polymer degradation as well as surface cracks. An example of the efficiency loss is shown in Fig. 2.3, where the mean total charge per minimum-ionising particle (MIP) for the AD detector is plotted. One can see that the mean total charge per MIP has a decreasing trend, which corresponds to the ageing of the material. However, there is a contribution from other factors such as the ageing of the photomultiplier tubes, which causes the lowering of the detector signal. On the other hand it was observed, that scintillator materials tend to recover from the efficiency loss over time. This phenomenon is called annealing.

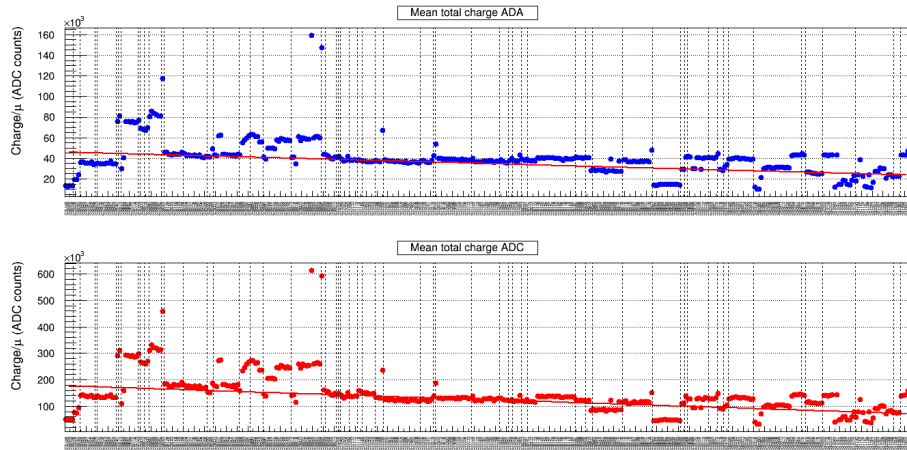


Figure 2.3: Mean total charge per minimum-ionising particle (MIP) measured by AD detector sides ADA and ADC during Run 2 (2015-2018) at ALICE. This corresponds to the lowering of the measured MIP charge, hence showing the efficiency loss of the detector over time. Courtesy of M. Broz.

2.2 Inorganic scintillation materials

With respect to organic scintillators, inorganic scintillators have a higher stopping power as they are generally more dense and have a higher atomic number, making them a suitable candidate for the detection of γ radiation. Inorganic scintillators also have a higher light output and output linearity in comparison with organic scintillator. One of the downsides is the generally longer response time that can be solved if one takes into account the quantum confinement effect for nanocrystals.

2.2.1 Scintillation mechanism for inorganic scintillators

Band structure

Crystalline materials are made of atoms in repeating structures giving rise to covalent bonds between the electrons of the mentioned atoms. This creates a two-band structure for the electron energies: the valence band and the conduction band. There is an energy gap between the two bands called the forbidden gap and its width divides materials into conductors, semiconductors and insulators [27].

At low temperatures, all of the valence electrons occupy the valence band, where they are bound in their respective positions in the lattice. If there is an energy excitation by ionising radiation of sufficient energy, the electron surpasses the forbidden gap and jumps to the conduction band making it free to move throughout the crystal. When an electron leaves its position in the valence band, an empty space is left in the lattice, which behaves as a positively-charged particle called a hole. If the energy from the ionising radiation absorbed by the molecule is not enough for the electron to jump to the conduction band, an exciton can be formed. Exciton is a bound state of the electron and the remaining hole, which is bound by the Coulomb interaction. The exciton band lies beneath the conduction band as it does not require as much excitation energy as the conduction band.

Scintillation mechanism

If a high-energy charged ionising radiation passes through a crystalline scintillator, it will form a number of electron-hole pairs in the conduction band and the valence band, respectively. The electrons which are highly excited excite other electrons from the valence band either to the conduction or the exciton band. The electrons and holes drift through the material and lose their energy through a thermalisation process.

After the energy of the electrons and holes reaches the minimum level corresponding to the lowest energy in the conduction band and to the highest energy in the valence band, respectively, they would recombine together and produce a photon with high energy during the recombination process. However, this process is inefficient in pure crystals and moreover, the energy of such a photon would be too high for it to be in the visible spectrum range.

Material impurities and lattice defects lead to the formation of recombination centres, where drifting electrons and excitons can get trapped. These traps lie in the forbidden gap. Some of the recombination centres can form luminescence centres while other may lead to non-radiative recombination of the electron-hole pairs, which represents quenching of the scintillation process. The traps have a strong influence on the time resolution of the scintillators. During the recombination of the electron-hole pairs in the luminescence centres a scintillation photon is emitted with a wavelength in or close to a visible spectrum range.

However, there exists a number of competing processes to the formation of a scintillation photon in the luminescence centre. The electron in the recombination centre can form an excited state whose transition to the lower energy level is forbidden. In such a case, the electron needs another increase of energy, e.g. thermal, to be able to recombine with the hole. A resulting scintillation photon is delayed with respect to the others and creates a slow scintillation component called phosphorescence, which worsens the scintillator time resolution. Another competing process already mentioned above is a recombination via a non-radiative process, where the energy is absorbed by the crystal lattice and no photon is emitted as a result.

2.2.2 Time response

Similarly as for organic scintillators, the time response of the inorganics cannot be described by a single decay time τ . One has to account for the drifting time of the electron-hole pairs to the luminescence centres and for the competing processes to take place. The final time response is then given by a set of different components, which are all subject to exponential decay and have their own decay times.

2.2.3 Radiation hardness and stability

The interaction of ionising radiation with inorganic scintillators has a similar effect as in organic scintillator. The inorganic scintillator might show damage via color changes and light transmission losses, if the damage is more severe, even the light production can be affected. Unlike organic scintillators, inorganic crystals are mostly hygroscopic, which imposes their sealing in air-tight containers making their use slightly unpractical. The inorganic scintillators are also liable to thermal instability, where a temperature difference of a few °C can lead to a deterioration in the light yield or timing performance.

2.3 Nanomaterials

Nanomaterials are defined as materials with at least one of their dimensions in the range of nanometres, typically less than 100 nm. Thanks to the size difference with respect to bulk materials, nanomaterials display different properties, which play a key role in their physical and chemical behaviour.

Chemical behaviour

The main difference in terms of chemical behaviour of nanomaterials comes from the increased fraction of the surface atoms N_S with respect to the atoms in the volume N_V as the dimensions of the material grow smaller as depicted in Fig. 2.4. If a homogeneous spherical material is considered, the proportion can be estimated by the formula

$$\frac{N_S}{N_V} = \frac{1}{2R}, \quad (2.6)$$

where R denotes the material radius in nm. For an object of the diameter of 5 nm comprised of 8000 atoms, the proportion of the surface atoms is around 20 %. However, if the diameter is reduced to 1 nm, the proportion of the surface increases to 50 % [28].

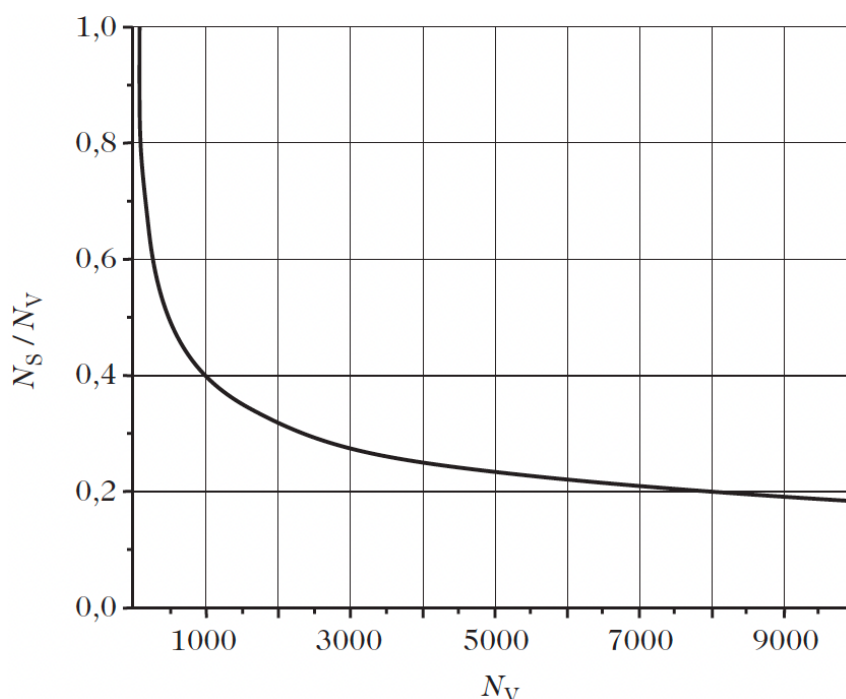


Figure 2.4: Ratio of the number of surface atoms N_S and atoms in the volume N_V in a spherical material. Figure taken from Ref. [28].

As the size of the nanomaterial is decreasing, the surface atoms have less neighbouring atoms leading to a decreased bond energy per atom. This allows the surface atoms to react easily with the aim to decrease their surface energy [29]. However, such recombination, during which larger structures are formed, is undesirable as the material loses the attractive properties because of which it was created in the first place. In order to prevent this, organic ligands are used to coat the surface of the nanoparticles, which act as a steric barrier preventing their aggregation. Nevertheless, it can be tricky to determine whether the reaction providing the coating of the nanoparticles took place successfully due to their size, hence many different methods are needed for such studies.

Physical behaviour

During the reduction of the material dimensions, the nanoparticles are affected by quantum effects making their physical properties different from the bulk materials. One of the examples might be the phenomenon of quantum confinement, during which the nanoparticle electron-hole pairs (excitons) are spatially confined and their energy levels become discrete, whereas the energy levels of a bulk material are continuous. The increase of the exciton energy is analogous to the confinement of the electron wave function in quantum mechanics.

The quantum confinement effect appears when the dimensions are reduced near to the de Broglie wavelength of the electrons. A diagram of the energy band structures in bulk materials and semiconductor nanocrystals is shown in Fig. 2.5. As one can see, the energy band gap between the conduction band (CB) and the valence band (VB) increases with the decreasing size of the particles [30].

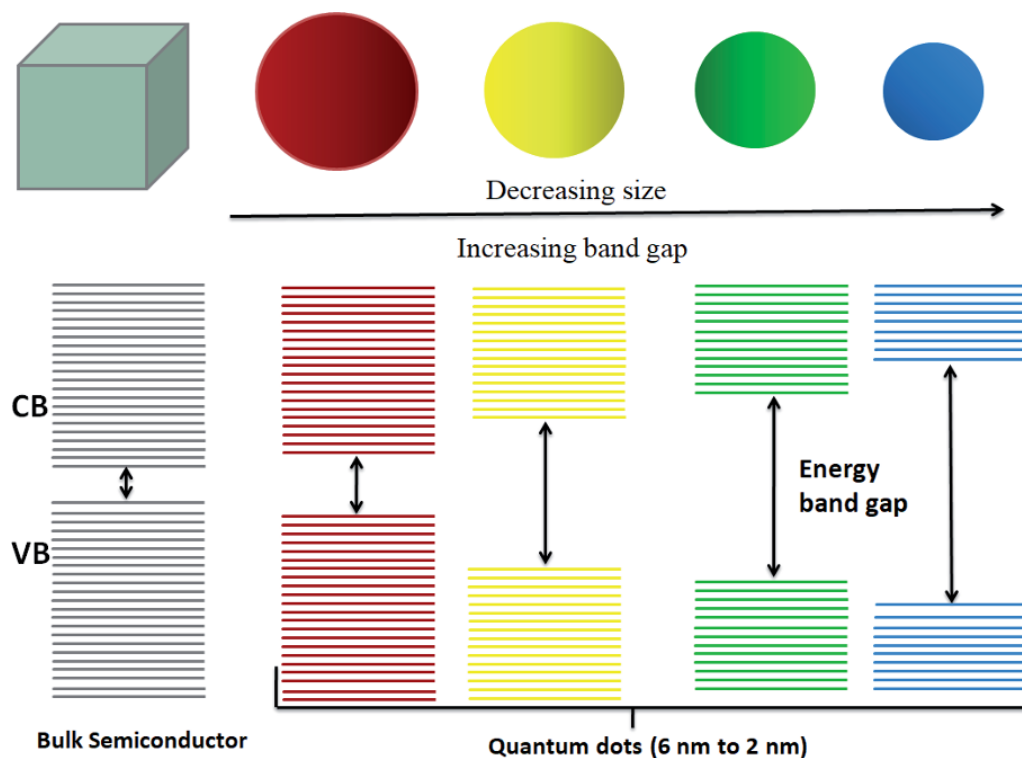


Figure 2.5: Diagram of energy bands in bulk semiconductors and semiconductor quantum dots. Figure taken from Ref. [30].

2.3.1 Quantum dots

Semiconductor crystals confined in all three dimensions below 10 nm are called quantum dots (QD). As discussed in the previous section, thanks to the phenomenon of quantum confinement, QD have very efficient and ultrafast (even subnanosecond) exciton emission. Moreover, the properties of the emission are tunable with the

crystal size, as the difference between the energy levels and the band gap increases with decreasing size of the produced crystals. However, to control the size and the size distribution of the crystals, it is required to use controlled syntheses of the crystals such as the hot-injection method discussed below.

2.3.2 Lead halide perovskite nanocrystals

Metal halide perovskites (MHPs) are studied already since the last century, but only during the late 1990s and early 2000s they showed attractive properties for applications in electronic and optical devices. However, after the colloidal synthesis of lead halide perovskite nanocrystals was introduced during the middle of 2010s, they attracted attention in many other fields and products such as photovoltaics, LEDs, displays or lasers [31].

The inorganic three-dimensional (3D) MHPs belong to crystalline compounds of a generic formula ABX_3 , where the $B = Pb^{2+}$ cations have six neighbouring anions $X = Cl^-, Br^-, I^-$ forming an octahedron. Eight of these corner-sharing octahedra are comprising a cavity in which a $A = Cs^+$ cation sits. This structure is represented in Fig. 2.6.

In 2015, a revolutionary discovery took place when a hot-injection method for the synthesis of lead halide perovskite nanocrystals was introduced, which provided excellent control over their size, size distribution and stability [33]. As discussed already in the previous section, allowing the possibility of controlling the nanocrystal size provides a way to tune the emission spectra. Nevertheless, a similar result can be achieved with the changes of the $X = Cl^-, Br^-, I^-$ anions where the resulting emission spectra cover the entire visible spectrum of 410-700 nm with FWHM of 12-42 nm. The photoluminescence quantum yield for $CsPbX_3$ nanocrystals ranges between 50-90 % and their time decays lie in the range of 1-29 ns. This is also illustrated in Fig. 2.7.

Thanks to the mentioned properties of the $CsPbBr_3$ nanocrystals, one of the emerging applications is to use them as ultrafast timing scintillation detectors for high-energy physics (HEP) and medicine, e.g. TOF-PET. However, there are several downsides, namely: poor stopping power and small Stokes shift of the absorption of emission spectra. Unfortunately, these two imperfections are contradictory since the lack of stopping power could be solved with simply having larger structure; however, due to the small Stokes shift, such structure tends to have severe issues with self-absorption making the material non-translucent.

One of the possible solutions for the insufficient stopping power of quantum dots is to use a bulk scintillator with high stopping power and providing energy resolution together with thin layers of $CsPbBr_3$ nanocrystals serving as time taggers. To improve the self-absorbance of the nanocrystals and increase the transparency of the scintillator composite, an appropriate wavelength shifters could be added to the mixture, yet this would negatively influence the ultrafast time response. Such possibilities are the subject of various studies with an ideal solution still to be provided.

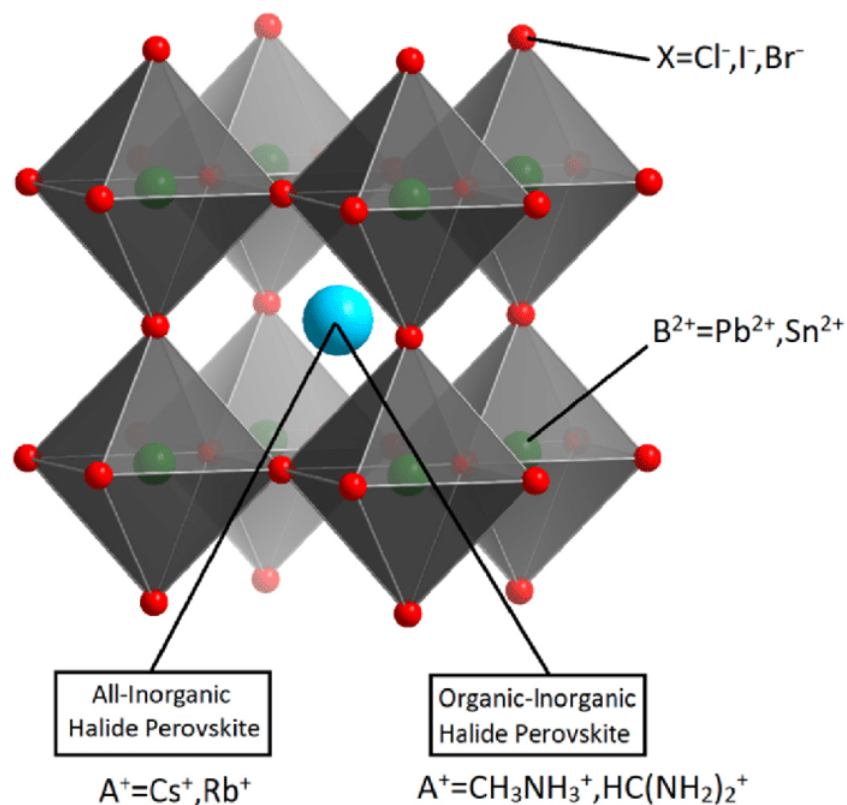


Figure 2.6: Diagram of metal halide perovskite of a generic formula ABX_3 crystal structure. Figure taken from Ref. [32].

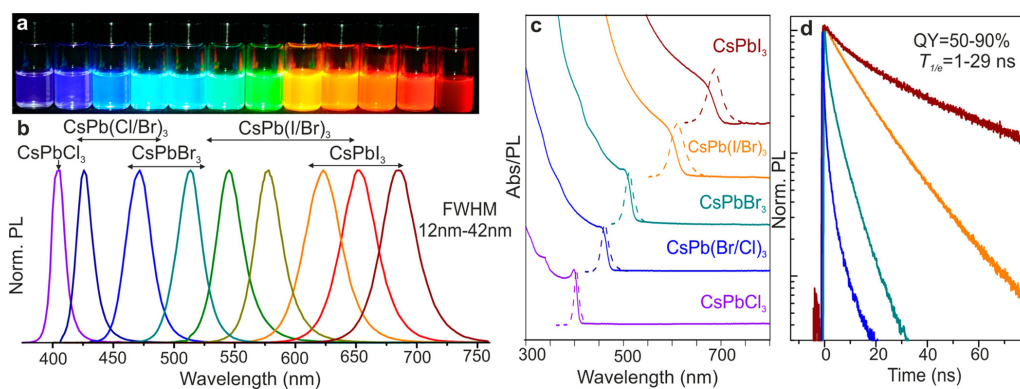


Figure 2.7: Illustration of $CsPbX_3$ nanocrystal properties regarding their emission and absorption spectra: a) different nanocrystals in toluene solutions under UV lamp ($\lambda = 365$ nm), b) PL spectra, c) absorption (full line) and PL spectra (dashed line), d) PL time decays shown for c) except $CsPbCl_3$. Figure taken from Ref. [33].

2.4 Hybrid materials and nanocomposites

2.4.1 Introduction

It is long known that properties of pure materials such as metals or plastics can be enhanced by creating mixtures of their pure forms, also called hybrid materials. These materials show superior properties with respects to the original materials separately, hence they can be exploited to fulfill the constantly increasing requirements of modern technologies on novel materials. One of the examples of hybrid materials is the mixing of inorganic components and organic polymers. Even though such combination might seem artificial, it is motivated by materials found in nature.

As the definition of hybrid materials can be quite broad, it is, in this context, subtly specified as follows: a hybrid material is a combination at least two components blended on the molecular scale. These can be further subdivided according to the interaction strength between the components into Class I and Class II materials. The former comprises materials with weak interactions between the two compounds such as van der Waals, hydrogen bonding or weak electrostatic interactions. The latter describes materials that show strong chemical interaction between the constituents such as the covalent bond.

2.4.2 Nanocomposites

A hybrid material is also referred to as nanocomposite if the size of one of the structural units is in the range of 1-100 nm. Nanocomposites are typically formed by embedding of inorganic nanoparticles into organic polymers. An important attribute of nanocomposites is their polymer-like handling during their production, e.g. the mixing of the materials does not require high temperature treatment as for solid state inorganics. Therefore the material can be shaped in various forms and sizes. Thanks to the nanoscale dimensions of the building blocks, the resulting composite can possess relatively high optical transparency making it an ideal candidate for optical applications. To preserve the nanoscale dimension of the inorganic nanoparticles, it is crucial to reduce their surface energy with ligands and avoid their agglomeration and further aggregation [34].

2.4.3 Preparation of the nanocomposites

The material composites can be produced in several ways as shown in Fig. 2.8. Either both the nanoparticles and the polymer can be prepared beforehand and then mixed; or the nanoparticles can be pre-synthesised, mixed with a monomer and further polymerised; or one or both of the components can be synthesised *in situ*.

In order to optimise the most control over the final nanocomposite and the simplicity of the production, mixing of the pre-synthesised nanoparticles together with a monomer and its subsequent polymerisation is used. In this approach, there is a

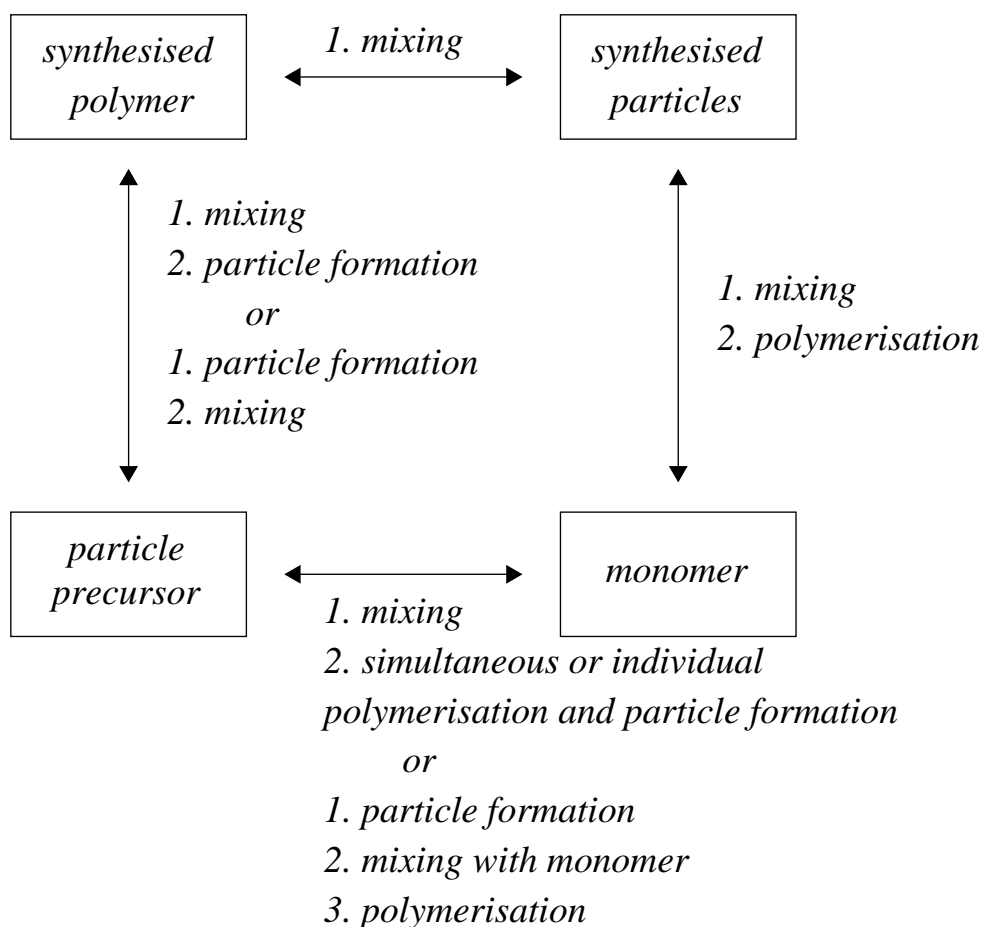


Figure 2.8: Diagram of the basic techniques used to produce nanocomposites. Reconstructed according to Ref. [34].

good chance of getting a monodisperse distribution of the NC in the final nanocomposite if a correct monomer is chosen. The monomer needs to have a similar chemical character as the colloidal solution of the NC to properly mix and disperse the NC into the monomer. Such compatibility can be also improved with the right choice of surface ligands, which prevent the NC agglomeration. Moreover, a specific surface ligand forming covalent bonds with the monomer can be chosen. In that case the NC can directly polymerise together with the matrix providing the best dispersion and preventing the NC aggregation.

2.4.4 Matrix polymerisation

A polymer is a macromolecule consisting of smaller repeating chemical units called monomers. Polymers can be either divided into condensation and addition polymers according to their structure, or they can be divided based on their polymerisation mechanism into step and chain polymers. In most cases, condensation polymers are

created by the step mechanism, while the addition polymers are produced via the chain polymerisation. However, this is not always the case and the aforementioned terms should be applied accordingly.

The commonly used polymers for scintillator production like polystyrene (PS), polymethyl methacrylate (PMMA) or polyvinyl toluene (PVT) are polymerised by the chain mechanism. For the chain polymerisation to start, an initiator is needed to produce a reactive centre. This can either be a free radical, cation or anion, which changes the π bond into the stronger σ bond and creates another reactive centre. The process then repeats itself and more monomers are added to the chain of the newly created polymer without any secondary products. The initiator can be added to the monomer in the form of a compound containing a given functional group or the polymerisation process can be induced by treatment with increased temperature or UV radiation [35].

2.5 Photodetectors

When a charged particle passes through a scintillator, it produces rather few photons of a certain wavelength according to the material of the scintillator. However, to efficiently extract, store and study the information about the particle, this light signal is typically transformed into an electrical signal. This conversion is done with a photodetector, which produces an electrical signal proportional to the amount of light it receives. A frequently used device is a photomultiplier tube (PMT).

2.5.1 Photomultiplier tubes

Photomultiplier tubes are devices made of three major components: the photocathode, the electron multiplier, and the casing, particularly the entrance window. PMTs receive the weak light intensity output from a scintillator in the form of photons of a certain range of wavelength. The incident photons kick out the electrons of the photocathode material, which includes a photosensitive layer. The created photoelectrons are accelerated from the photocathode to a chain of dynodes, which have a difference of potential that multiply and accelerate the electrons when they hit each stage. At the end, the electrons are collected in the anode of the PMT, where they form a measurable signal. The scheme of a PMT with a fine-mesh dynode structure is shown in Fig. 2.9.

The multiplication process in a single dynode is given by

$$\delta = \frac{\text{number of secondary electrons emitted}}{\text{primary incident electron}}. \quad (2.7)$$

Typically, PMTs use N dynodes achieving an overall gain, defined as

$$\text{overall gain} = \alpha \delta^N, \quad (2.8)$$

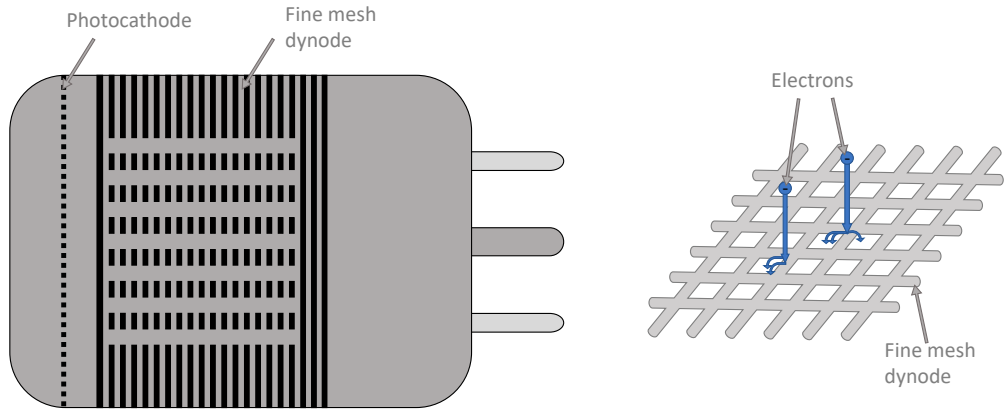


Figure 2.9: Scheme of a fine mesh photomultiplier tube (left) and the detail of its dynode structure (right).

on the order of 10^6 . The fraction of all photoelectrons captured by the electron multiplier is denoted by α . The number of dynodes N depends on the used dynode structure, but it typically ranges between 9 to 16.

The overall gain of a PMT is a function of the applied voltage V , hence it can be decreased or increased by supplying lower or higher voltage to the PMT. This is commonly used when the detector performance deteriorates, either due to the ageing of the scintillator, the PMT or other detector components. This might be caused by the ionising radiation and magnetic fields in which they operate as well as many other different factors. In case of insufficient performance, the supply voltage can be increased until a sufficient electrical signal from the PMT is achieved. However, the increase of supply voltage to the PMT can cause higher noise or dark current pulses, which in turn promote the background. Additionally, long-term supply of increased HV to the PMTs can even cause earlier ageing of the device.

2.5.2 Time response

In order to obtain an electrical signal from the scintillator, a photodetector has to be used to transform the light pulse into an electrical pulse. An example of the final electrical pulse is shown in Fig. 2.10. The pulse can be described by many characteristics, e.g.:

- the *peak amplitude*, which is the maximum amplitude of the pulse,
- the *peaking time*, which is the position of the peak amplitude in time,
- the *rise time*, which most commonly defined as the time during which the pulse rises from 10 % to 90 % of the peak amplitude,
- the *charge* Q , which corresponds to the integral of the pulse in a selected time window; Q is proportional to the primary deposited energy of the particle in the detector in systems with linear response,

- the pulse width, commonly defined as *full width at half maximum (FWHM)*,
- the *baseline* or *pedestal*, which correspond to the zero level of the signal [24].

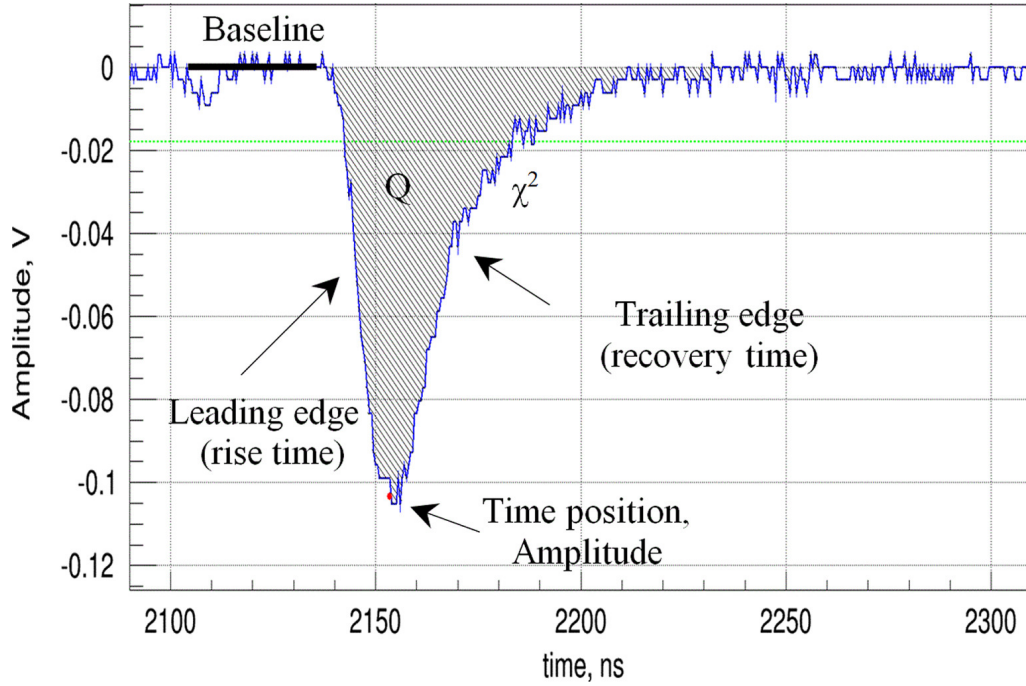


Figure 2.10: Example of a typical detector pulse generated by the photodetector. Figure taken from Ref. [36].

The pulse-time profile features a very fast leading edge followed by an exponential decay with the form of

$$I(t) = I_0 e^{-t/\tau}, \quad (2.9)$$

where τ represents the decay time. The decay time of organic scintillators is a combination of the fluorescence (fast component) and phosphorescence (slow component) decay times, which are dependent not only on the material, but also on the particle type and energy. This provides the possibility of particle identification (PID) through pulse shape discrimination.

Chapter 3

Custom made scintillator samples

This chapter describes the production of polymer composites of CsPbBr₃ nanocrystals. Firstly, the synthesis of the nanocrystals and their ligand exchange is delineated and afterwards their embedding in different matrices and subsequent polymerisation is described. The chapter includes a summary of the produced samples and discusses their polishing and wrapping for the following characterisation.

3.1 CsPbBr₃ nanocrystal production and characterisation

3.1.1 CsPbBr₃ nanocrystal synthesis

The synthesis of the CsPbBr₃ nanocrystals (NC) was performed at the Department of Chemistry of FNSPE CTU in Prague. The NC were synthesised via the hot-injection method, which requires advanced equipment such as the vacuum pump or the inert atmosphere. Fig. 3.1 shows the Schlenk line, which features all of the needed apparatus for the synthesis.

The preparation procedure of the CsPbBr₃ NC via the hot-injection method is schematically depicted in Fig. 3.2. It can be divided into three steps: pre-synthesis of cesium oleate solution, hot injection of a cesium oleate into the lead-bromide solution, and isolation of the CsPbBr₃ NC. The final step is achieved with the exchange of the surface ligands, which are bound to the surface of the nanocrystals. The nanocrystals are then dispersed in toluene.

In order to prepare the cesium oleate solution, 1.303 g of Cs₂CO₃ is added together with 12.6 ml of oleic acid (OA) and 7.37 ml of 1-octadecene (ODE) in a 100 ml 3-neck flask. Such mixture is firstly put under the argon atmosphere, and then let to degas for 5 minutes under vacuum. The argon saturation and subsequent degassing under vacuum is once repeated to exchange as many gas molecules to argon. Once the argon rinsing is finished, the mixture is then heated up to 110 °C and let to react in vacuum while being mixed. The reaction is terminated after approximately one



- 1 Argon input
- 2 vacuum pump
- 3 Argon line
- 4 vacuum line
- 5 pressure gauge
- 6 secure bubbler
- 7 control bubbler
- 8 thermometer
- 9 temperature control unit
- 10 reaction flask in a heating nest

Figure 3.1: Photograph of the Schlenk line used for the synthesis of CsPbBr_3 nanocrystals. Figure taken from Ref. [37].

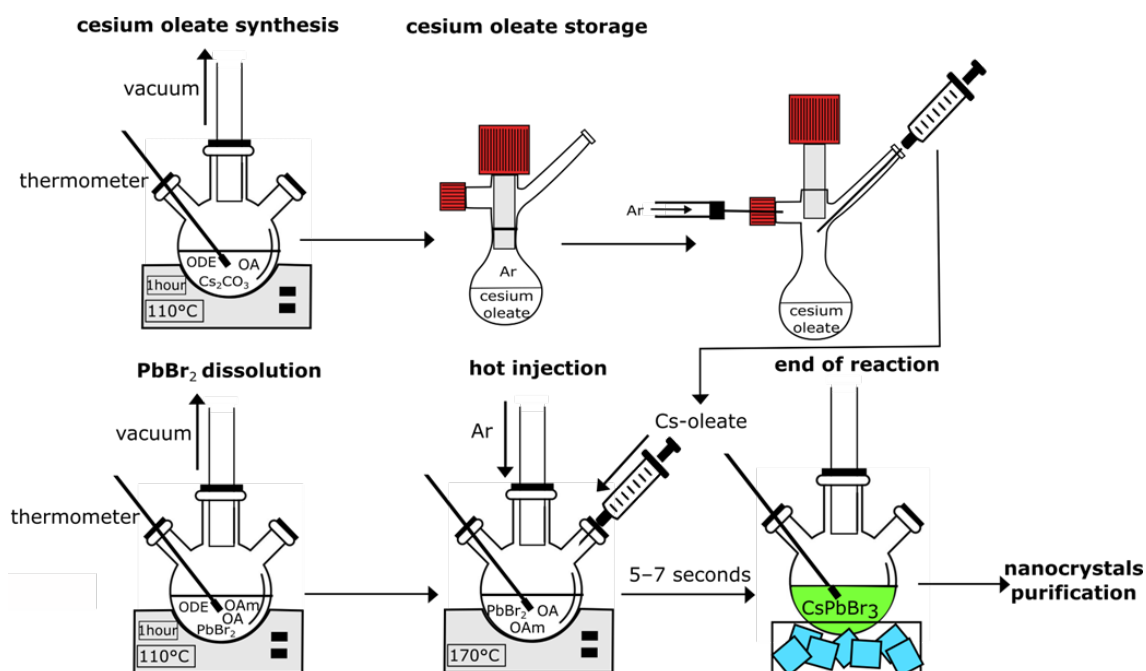


Figure 3.2: Schematic diagram of the production of the CsPbBr_3 nanocrystals using the hot-injection method. Figure taken from Ref. [37].

hour, when the Cs_2CO_3 completely dissolves. The produced cesium oleate solution is stored in an Aldrich Sure/Stor flask as depicted in Fig. 3.3a.

To prepare the main precursor, 0.276 g of PbBr_2 , 20 ml of 1-octadecene, 2 ml of oleylamine (OAm), and 1.78 ml of oleic acid is mixed in another 100 ml 3-neck

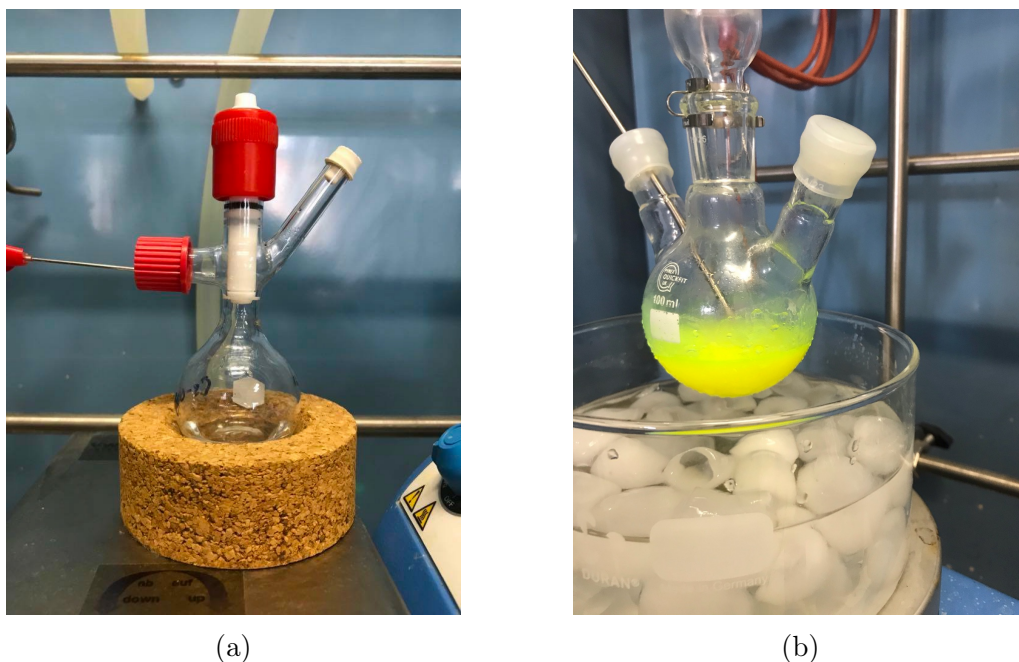


Figure 3.3: a) Cesium oleate solution stored in a Aldrich Sure/Stor flask, b) termination of the reaction after the hot injection of the cesium oleate into the reaction compound by submerging it in an ice bath. Figure taken from Ref. [37].

flask and degassed with argon and vacuum as in the previous case. After that, it is heated up to 110 °C under vacuum for one hour for the mixture to dry out and for the PbBr_2 to dissolve. The reaction solution is then put under the argon atmosphere and heated up to 180 °C. Subsequently, the heating nest is removed and the temperature of the mixture is let to reduce to 170 °C, when a 0.5 ml of the cesium oleate solution is injected into the precursor. The reaction is terminated after 5-7 seconds by cooling of the flask in an ice bath as shown in Fig. 3.3b. The produced NC are obtained by centrifugation of the reaction compound at 10950 g^1 for 5 minutes. The CsPbBr_3 solution is obtained by dispersion of the sedimented nanocrystals in toluene.

Further details about the synthesis can be found in [37], [39] and [40].

3.1.2 Ligand exchange

During the synthesis, the NC are covered by OAm and OA ligands as shown in Fig. 3.4. However, such ligands are not the most optimal option for the production of scintillators for two reasons: they are weakly bonded to the surface of the nanocrystals and they are chemically distinct from the matrices during the production of polymer composites.

The consequences of the OAm and OA not holding well to the nanocrystals might

¹g stands for relative centrifugal force and it is given as $g = 1.118 \cdot 10^{-5} r S^2$, where r stands for the radius of the rotor in cm and S denotes the speed of the centrifuge in revolutions per minute (RPM) [38]

be fatal from the point of view of the composite production. The role of the surface ligands attached to the nanocrystals is to prevent them from agglomerating and aggregating into bigger clusters (μm scale) which would lead to the vanishing of the quantum confinement effect and their excellent scintillation properties. However, the OAm and OA ligands are bound to the surface dynamically and the bond between them and the NC can be easily lost leading to the aggregation of the NC. Hence, the nanocrystal ligands can be exchanged for more suitable ones that would hold to the NC better and provide more protection against the accumulation. To this end, didodecyldimethylammonium bromide (DDAB) is used as an alternative to OAm and OA. It provides more long-term stability of the NC solution, better photoluminescence quantum yield, and lowers the non-radiative losses during the scintillation mechanism.

Another difficulty regarding the surface ligands is their chemical character, as it impacts the character of the NC heavily. If a proper surface ligand is chosen with chemical character similar to the character of the matrix, it is much easier to disperse the NC in the matrix. A homogeneous distribution of the NC in the matrix provides good optical properties and transparency of the resulting composite leading to possible higher filling of the composites (higher concentration of the quantum dots embedded in the matrix). If the ligand is not chemically similar to the matrix, the NC solution is difficult to mix in homogeneously and clusters of NC remain in the matrix. These clusters can lead to unwanted light scatterings, which degrade the light transmission in the composite making it opaque. An ideal ligand candidate could also form a covalent bond with the matrix, which would provide a way for the NC to polymerise directly with the matrix.

The ligand exchange procedure can be described as follows. A 55 mM^2 DDAB toluene solution is prepared in a beaker. The cooled reaction compound containing the CsPbBr₃ NC before centrifuging is added to the DDAB solution. After two minutes of mixing, the colloidal solution is precipitated by ethylacetate and centrifuged for 10 minutes at 4800 g. At last, the sediment is dispersed in toluene to get the final concentrated solution. The used proportions for the ligand exchange are 3 ml of the reaction compound from the HI synthesis, 2 ml of the DDAB toluene solution and 15 ml of ethylacetate.

The final solution for the purpose of producing nanocomposites had a measured concentration of 38.4 mg of nanocrystals per one ml of the solution. The QD concentration was measured via the absorbance of the solution according to Ref. [41].

3.1.3 CsPbBr₃ nanocrystal characterisation

To characterise the produced nanocrystals, emission PL, excitation PL and absorption spectra were measured using a FluoroMax Plus spectrofluorometer by Horiba. The characterisation took place right after the production of the samples and it was performed at room temperature in air. To prepare the sample containing the CsPbBr₃ NC for measurements, it was diluted by a factor as high as 3000.

²mM= 10^{-3} mol per litre

HI synthesis of NC CsPbBr₃

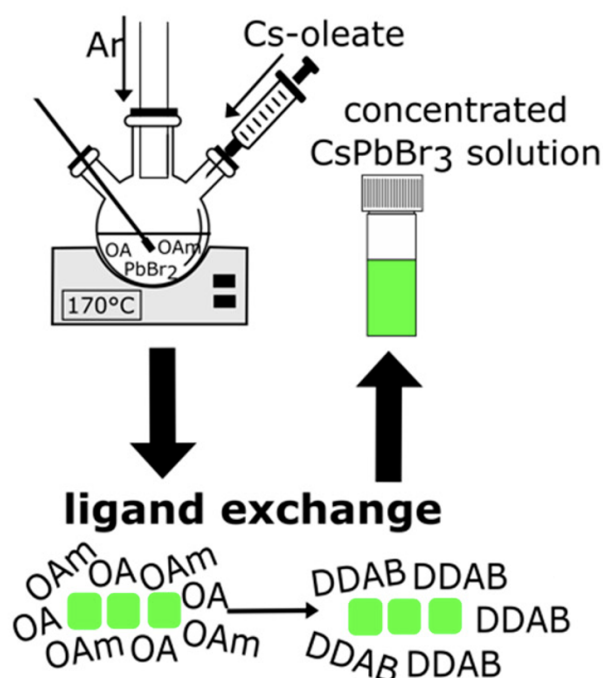


Figure 3.4: Schematic diagram of the ligands exchange from oleylamine (OAm) and oleic acid (OA) to didodecyldimethylammonium bromid (DDAB) at the surface of CsPbBr₃ nanocrystals (NC) produced by the hot injection (HI) synthesis. Figure taken from Ref. [40].

Emission and excitation photoluminescence spectra

The excitation spectrum is plotted together with the emission spectrum on Fig. 3.5a. The former shows the relative PL intensity at the maximum of the emission spectrum with respect to the excitation wavelength. The latter shows the relative PL intensity with respect to the wavelength of the emitted photons. The wavelength chosen for the excitation is the maximum of the excitation spectra, corresponding to around 300 nm. The measured interval for the excitation spectrum is 200-510 nm and 400-600 nm for the emission spectrum, respectively.

Absorption spectrum

The absorption spectrum, showing the absorbance of the sample with respect to the incident wavelength, is displayed on Fig. 3.5b. The wavelength interval for the incident photons during the measurement was set to 200-800 nm. As mentioned before, the value of the solution absorbance at 400 nm was used for the calculation of the concentration of the nanocrystals.

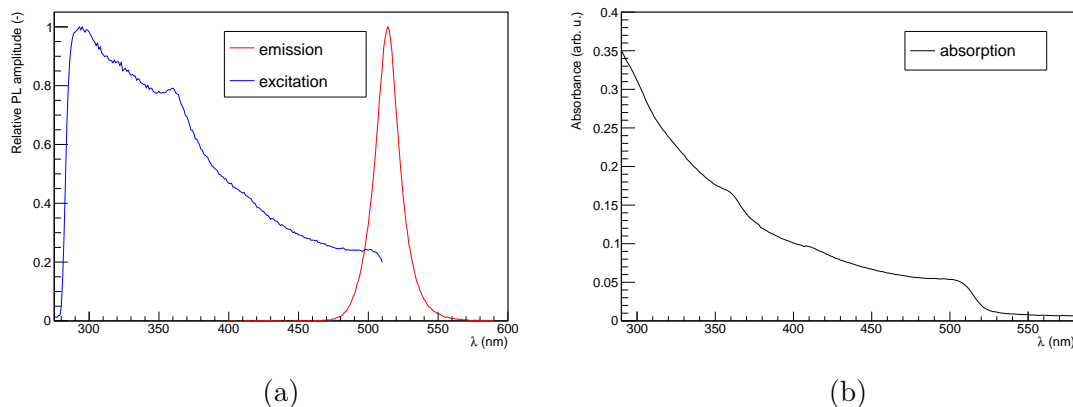


Figure 3.5: a) Emission (red) and excitation (blue) spectra of the produced CsPbBr₃ nanocrystals via the hot-injection method, b) their absorption spectrum. Figure taken from Ref. [37].

3.2 Composite production

In order to preserve the excellent scintillation properties of the CsPbBr₃ NC, it is needed to protect them from external influence such as air humidity, water, atmospheric oxygen or high temperatures. Such protection might be provided by embedding them into organic matrices and producing nanocomposite materials. Aside from the protection, the composite can afford better optical properties of the material as well as provide the needed stopping power.

However, as the nanocrystals tend to aggregate into bigger clusters (μm) before they are fixed in a matrix, it is needed to work with them swiftly. It is recommended to carry out the polymerisation within one month of the production of the dispersed NC in toluene, even after the surface ligand exchange to DDAB. It is suggested to keep the toluene solution in a dry and cold place, ideally secured with a parafilm tape to protect the NC from air humidity. The solution changes its colour to orange with time and its scintillation is attenuated, whereas a new toluene solution with NC has a yellow colour and brightly scintillates under UV light. The delay can also lead to opaque samples as the NC are not distributed homogeneously in the matrix when mixing them with the organic base, which might cause the light scattering discussed earlier.

It is important to note that this production of polymer nanocomposites was a pilot work to explore the possibilities of what can be done with the CsPbBr₃ NC. The production was mainly done in a research manner to see how to work with the inorganic NC when incorporating them into organic matrices and to investigate different methods and techniques of the production. That said, there was no common and optimised procedure for the production of all samples; on the contrary, the process and the used reactants were slightly changed for almost every production according to the outcome of the previous samples.

The whole production procedure was done at Universidad Autónoma de Sinaloa (UAS) in Culiacán, Mexico under the supervision of Dr. Ildefonso León Monzón.

It took around 4 weeks, during which I was shown how to work with the chemicals and prepare the polymer matrices. After an introduction, several composite samples with different concentrations of the NC were produced. Two organic matrices were used for the process: polystyrene and silicone. A few samples without NC were also produced in order to have control samples and to provide the possibility to study the effect of adding the NC to the pure matrix.

3.2.1 Polystyrene matrix

For the production of the polystyrene matrix, epoxy resin and styrene monomer manufactured by Reichhold were used. At first, they were mixed together in a plastic container with a plastic spoon in a ratio of 3:1 of epoxy resin:styrene. The epoxy resin and styrene were measured out with a syringe. To start their polymerisation, two catalysts, namely RP-128 [42] and MEKP by Reichhold were added to the mixture and thoroughly mixed. For the majority of the samples, we used around 8 ml of the total material, corresponding to 6 ml of epoxy resin, 2 ml of styrene and 2 and 2 drops of RP-128 and MEKP, respectively. After mixing of the components together, the compound was poured into a mould where the polymerisation took place as shown in Fig. 3.8. The mould for the polystyrene (PS) samples was made of the silicone matrix described below. Since the reaction was initiated by the catalysts, it was no longer needed to apply heat or UV radiation for the polymerisation to start.

The polymerisation was done at room temperature under no specific conditions regarding the atmospheric pressure. The total casting time was usually several hours; however it is ideal to let the mixture cure overnight ($\approx 14\text{-}20$ h). In order to obtain a homogeneous sample, it was necessary to add the RP-128 as the last component to the mixture and mix it promptly and thoroughly. The reason for this is that after the addition of RP-128, the polymerisation process starts immediately.

3.2.2 Composites with CsPbBr₃ nanocrystals

The set-up used for the composite production is shown in Fig. 3.6. The first step of the production depended on the concentration of the NC in the final sample. The amount of the toluene solution that was added to the base was calculated with respect to the weight of the final sample and the expected final concentration, e.g. for a sample with 6 g of epoxy resin and 2 g of styrene with the final concentration of 0.05 % QD, the needed weight of NC is 4 mg, which corresponds to ≈ 0.1 ml of the toluene solution.

For samples with high concentration, the QD solution was first mixed with the styrene and let to evaporate (as shown in picture D of Fig. 3.8) for a bit as described below. On the other hand, for samples with low concentration, the QD solution was first thoroughly mixed with the epoxy resin. In both cases, the compound was then mixed together with the missing part of the base, epoxy resin for high concentration and styrene for low concentration, respectively. Afterwards, the correct amount of drops of MEKP was added and mixed vigorously. As a last step, the same amount

of drops of RP-128 was added and stirred rapidly. The mixture was poured into a cuboid silicone container and let to polymerise (see Fig. 3.8).



Figure 3.6: Set-up used for the production of the styrene composites with CsPbBr_3 nanocrystals. Used materials: epoxy resin (white jug with blue cap), styrene (white bottle with blue cap), toluene solution with CsPbBr_3 nanocrystals (yellow vial), MEKP (transparent vial), and RP-128 (violet vial). Used tools: disposable syringes, plastic cups, plastic spoons, pipette, and silicone mould.

It was found out during the production, that during the polymerisation, the toluene contained in the QD solution evaporated. For composites with higher NC concentrations this lead to spoiling of the intended cuboid geometry as the toluene was not distributed only on the top layer of the composite (see picture C of Fig. 3.8). In order to solve that, the toluene solution containing the NC was first mixed only with styrene and let to evaporate for several minutes. For the high NC concentration samples the evaporation took as long as 40 minutes in an oven at $50\text{ }^\circ\text{C}$ as the toluene content needed to evaporate was higher. On the other hand, for the samples with very low NC concentration this procedure was omitted as all of the toluene content evaporated during the production and did not negatively affect the resulting composite.

It was also found out that for low concentration composites, one has to first mix the QD solution together with the epoxy resin and then add styrene and MEKP and mix again. When all of the components were mixed together at once, the yellowish colour vanished corresponding to the disruption of the nanocrystals in the mixture.

Additionally, one should take into account that the toluene might slowly evaporate

during the time interval, which changes the concentration of the solution. However, it was observed that the effect of the evaporation is not large, so it was assumed that the concentration of the NC remained the same.

Photos of the sample production are shown in Fig. 3.7 and Fig. 3.8. One can see that the composite in Fig. 3.7 shows significant inhomogeneity in nanocrystal distribution, which was probably caused by lack of thorough mixing.

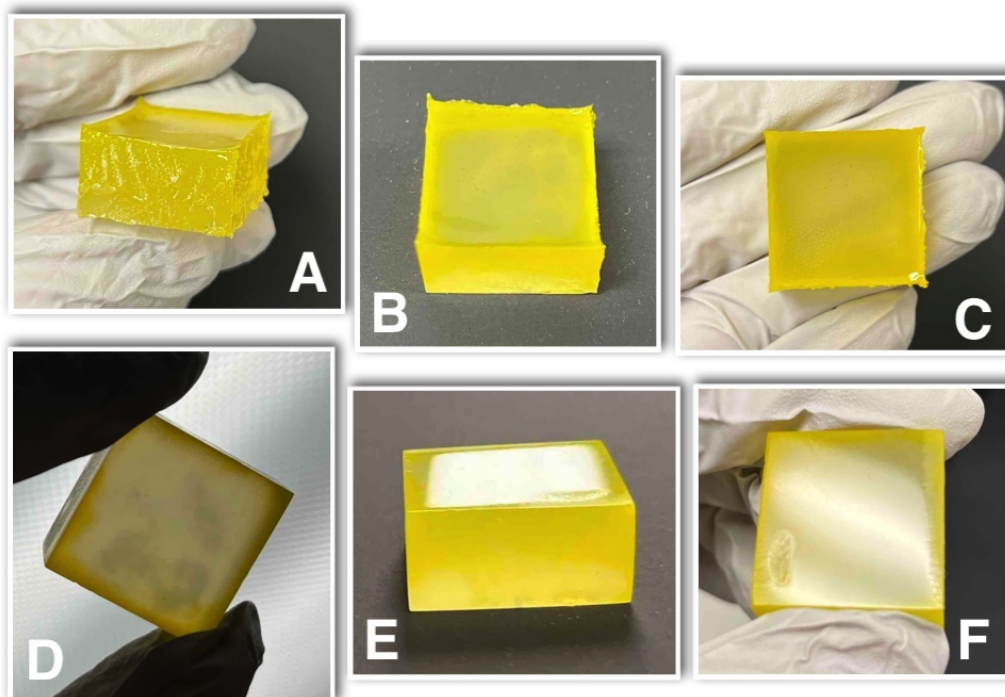


Figure 3.7: First trial of the composite production of CsPbBr₃ nanocrystals in polystyrene matrix: A), B), C) produced composite before polishing, D), E), F) produced composite after polishing. Note the inhomogeneity of the sample, which was probably caused by lack of thorough mixing.

3.2.3 Silicone matrix

The silicone matrix is made of the SILASTIC™ MS-4002 Moldable Silicone A&B kit [43]. As the name suggests, the material comes in two parts: A and B, which are ought to mix together in a 1:1 ratio and polymerise at high temperatures around 120 °C. The dosage was done with a syringe similarly to the polystyrene matrix. The two parts were mixed in a ceramic bowl vigorously, but air bubbles got inside the mixture of the silicone during this process. If the mixture would be polymerised with the bubbles, they would remain there even after the polymerisation making the sample not homogeneous and less transparent. For this reason, the mixture was poured in a dedicated mould and let to sit for the bubbles to get out overnight in an oven at 50 °C. This procedure might be sped up by placing the mixture in a

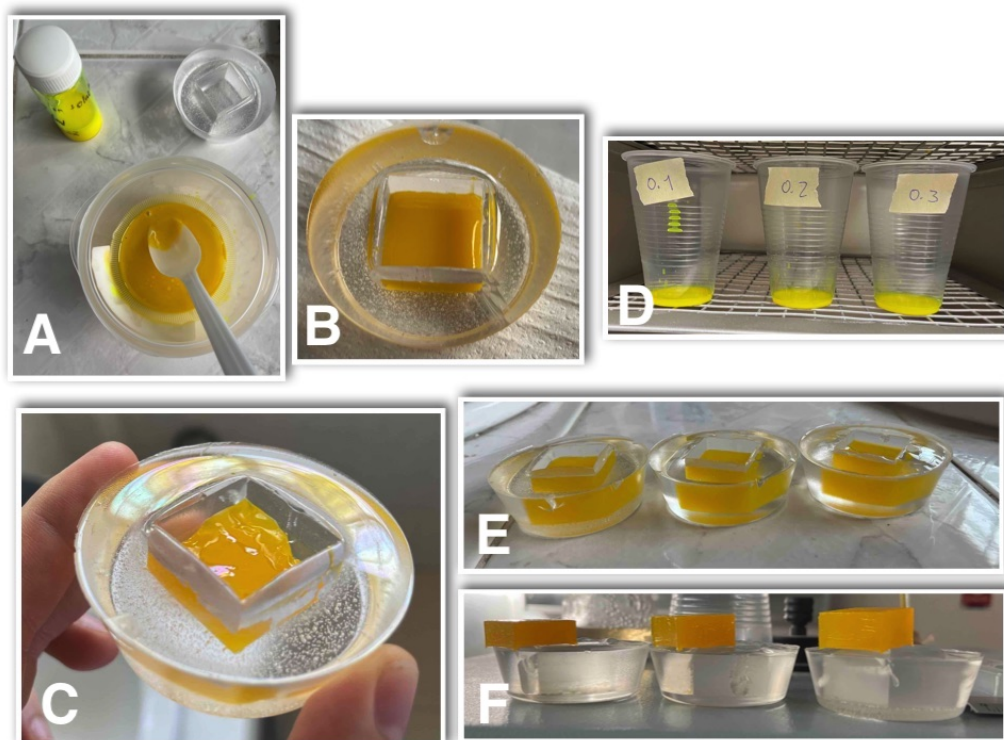


Figure 3.8: Further composite production of CsPbBr_3 nanocrystals in polystyrene matrix: A) composite mixture before polymerisation, B) composite in a silicone mould, where the polymerisation took place, C) composite after polymerisation, D) evaporation of toluene in toluene+styrene mixture at different concentrations (%) of the nanocrystals, E) composites before polymerisation, concentrations according to D), F) composites after polymerisation, concentrations according to D). Note the uneven shape in C) caused by toluene evaporation and the difference of the sample size in F), also caused by toluene evaporation.

vacuum chamber. After the majority of the bubbles escaped the mixture, it was left to polymerise in an oven at 110-120 °C for 2 hours.

As the polymerisation of the silicone matrix requires such high temperatures, it is needed to use a mould with higher resistance against temperature. To this end, an aluminium rectangular tube with a base of $2.9 \times 2.9 \text{ cm}^2$ was glued with sanitary silicone to the bottom side of a teflon sheet and used as a mould (shown in picture F of Fig. 3.9).

3.2.4 Silicone mould for polystyrene samples

As discussed above, the mould used for the production of polystyrene samples was made of the silicone matrix. The preparation of the silicone mould is depicted in Fig. 3.9. At first, a few mm thin layer of the silicone A and B mixture was poured into a teflon muffin pan and left to sit. After the bubbles escaped the silicone, it was polymerised in an oven at 150 °C. After the polymerisation, a $2.5 \times 2.5 \times 2 \text{ cm}^3$

steel cube was placed on the top of the finished layer and the silicone mixture was poured around it. It was again left to sit and then polymerised in an oven.

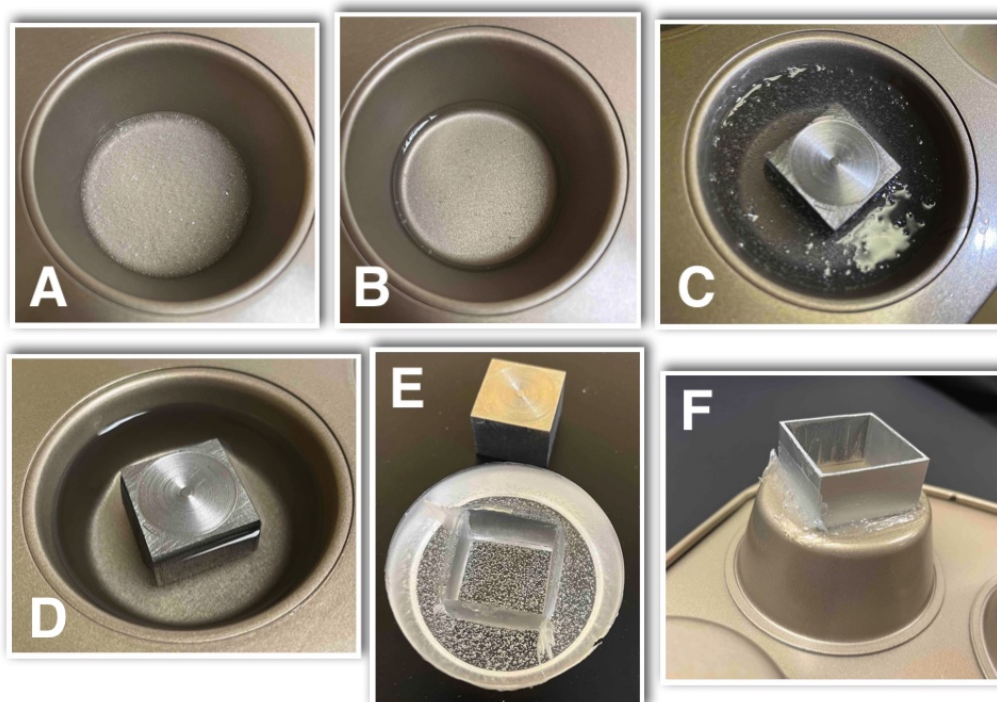


Figure 3.9: Preparation of the silicone mould for polymerisation of the polystyrene samples: A) thin layer of silicone before letting it to sit, B) thin layer of silicone after 1 h, C) silicone mould before letting it to sit, D) silicone mould before polymerisation, E) silicone mould after polymerisation in an oven at 150 °C, F) aluminium mould for preparation of composites with silicone matrix.

3.2.5 Composites with CsPbBr₃ nanocrystals

The production of CsPbBr₃ nanocomposites with the silicone matrix is captured in Fig. 3.10 and Fig. 3.11. For the production of silicone composites with the CsPbBr₃ NC, it is necessary to reduce the agglomeration and aggregation of the NC at temperatures higher than 60 °C. For this purpose, the toluene solution was first mixed with part A of the silicone kit. The idea behind this is that the toluene evaporates from the mixture and the NC have less possibilities to aggregate as the silicone material is very viscous. Such mixture is then complemented with part B of the silicone and again thoroughly mixed. It is then poured into the aluminium mould a let to sit as described before. The polymerisation process is the same as for the pure matrix.

There was an effort to produce composites with QD concentrations as low as 0.001 %, corresponding to $\approx 3 \mu\text{l}$ of the toluene solution. When this extremely small amount was combined with the silicone matrix and mixed with a plastic spoon, an amount of

the QD remained stuck on the spoon. However, for such small volumes, it could be that this amount might be a majority of the added QD, which makes it impossible to properly determine the actual concentration of the sample after the polymerisation.

3.2.6 Composites with PPO

Since the self-absorption is a serious problem for the CsPbBr₃ NC, it was decided to try to use only very small concentration of the NC and enrich the composite with 2,5-Diphenyloxazole (PPO). PPO is a commercial organic scintillating material, which is typically added to organic bases to produce scintillators. One of the most common approaches to use PPO is to dissolve it in a form of powder in a matrix and then polymerise it. The process is shown in Fig. 3.12. As part A was already used for mixing with the NC and toluene evaporation, only part B was available for PPO dissolving. In all cases, 120 mg of PPO corresponding to 1 % concentration in the final sample was mixed with 6 g of silicone part B thoroughly and let to dissolve in an oven at 100 °C for 2 hours. Both parts were then mixed together, poured into a mould and let to sit until the polymerisation. The polymerisation was done in the same manner as described above, on the next day in an oven at 110-120 °C for \approx 2 h.

3.3 Summary of the produced samples

For classification, transport, and storage of the produced composite samples, two plastic boxes with 9 spots each were prepared and filled with the samples as shown in Fig. 3.13 and Fig. 3.14 for the styrene and silicone samples, respectively. A summary of the sample properties is given in Table 3.1 for the styrene samples and in Table 3.2 for the silicone samples.

3.4 Polishing and wrapping of the samples

The scintillator samples with dimensions of $2.5 \times 2.5 \times 1$ cm³ were prepared for a measurement at the test bench described in Chapter 4. To measure them, one of the 4 faces with the smallest area was attached to the photocathode of a fine mesh PMT. To increase the transmission of the photons from the sample to the photocathode and reduce unwanted scattering of light at the protrusions of the faces, all of the sample faces were polished with sanding papers of the following grain from coarse to fine papers using the FEPA P standard: 150, 180, 400, 600, 1200, 1500 and 2000. To keep the produced light by the passing ionising radiation inside of the sample, all faces but the one attached were covered with two layers of 0.2 mm thick teflon tape RS PRO White PTFE as shown in Fig. 4.1.

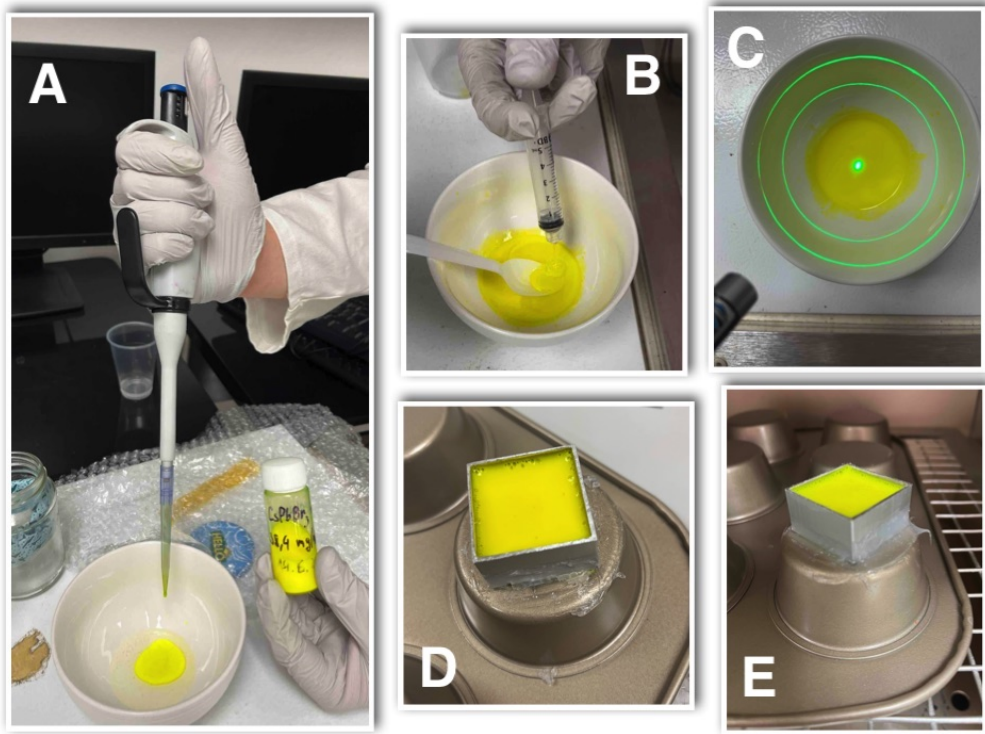


Figure 3.10: Preparation of CsPbBr₃ nanocomposites with silicone matrix: A) pipetting of the toluene solution into silicone part A, B) mixing with silicone part B, C) composite mixture before polymerisation, D) composite mixture before polymerisation in aluminium mould, E) composite mixture after polymerisation in an oven at 110-120 °C.

QD (%)	Date (2022)	Notes
0.1	27.6.	Not homogeneous
1	30.6.	Opaque
0.1	4.7.	Smaller dimension
0.2	4.7.	–
0.3	4.7.	–
0.1	7.7.	–
0.05	7.7.	–
0.05	13.7.	3&3 drops of RP-128 and MEKP
0	14.7.	3&3 drops of RP-128 and MEKP

Table 3.1: Summary of the produced CsPbBr₃ nanocomposites in a polystyrene matrix. The table contains the concentration of the NC according to the weight of the final sample, date of production and important notes. The note '3&3 drops' stands for use of 3 and 3 drops of the catalysts RP-128 and MEKP, respectively, compared to the use of 2 and 2 drops of RP-128 and MEKP for all other polystyrene samples.

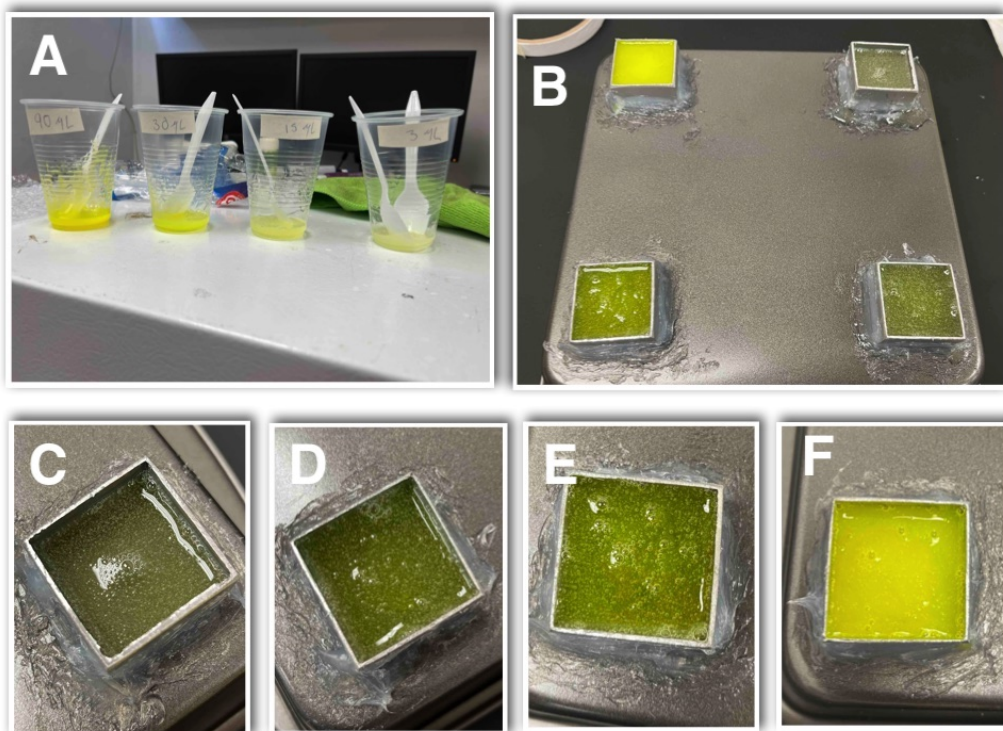


Figure 3.11: Preparation of low concentration CsPbBr_3 nanocomposites with a silicone matrix: A) mixture of toluene solution with silicone part A at different concentrations of nanocrystals, B) composites before polymerisation in aluminium moulds, C), D), E), and F) details of low concentration composite before polymerisation.

PPO (%)	QD (%)	Date (2022)	Notes
0	1	29.6.	Opaque
1	0.05	5.7.	–
1	0.03	6.7.	–
1	0.01	6.7.	–
0	0.005	7.7.	real concentration of QD lower
0	0.01	7.7.	–
0	0.03	7.7.	–
1	0	12.7.	–
0	0	12.7.	–

Table 3.2: Summary of the produced CsPbBr_3 nanocomposites in a silicone matrix. The table contains the concentration of the PPO according to the weight of the final sample, concentration of the NC according to the weight of the final sample, date of production and important notes.

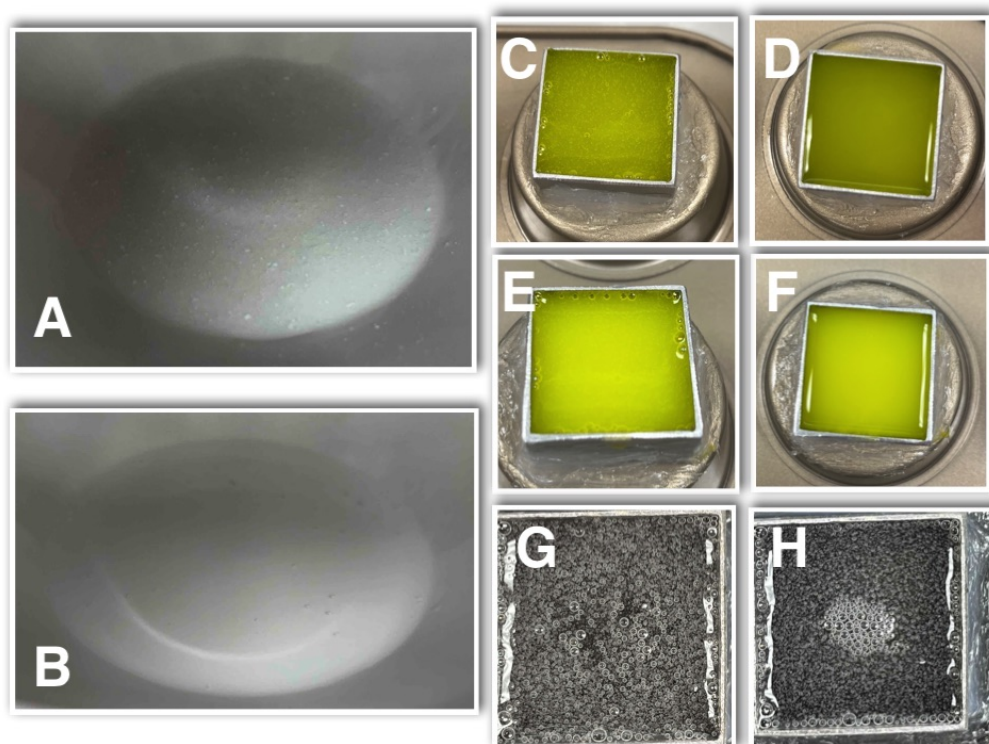


Figure 3.12: Preparation of CsPbBr₃ nanocomposites with silicone matrix enriched with commercial organic scintillator PPO: A) silicone part B) with added PPO before its dissolution, B) dissolved PPO in silicone part B, C), E) silicone composite full of bubbles after mixing of all the components, D), F) silicone composite after letting it to sit so the bubbles escape, status just before the polymerisation in an oven, G), H) details of the bubbles inside the composite before polymerisation.

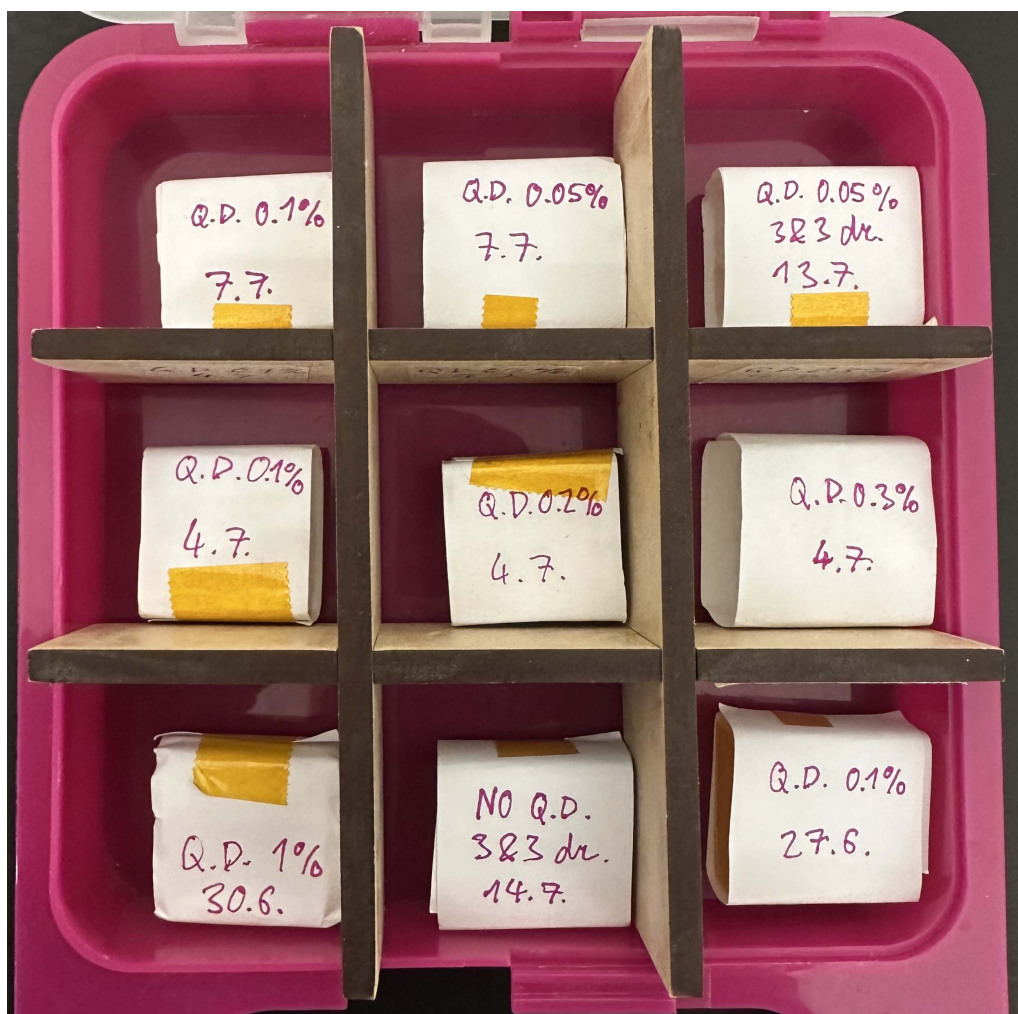


Figure 3.13: Box containing the produced CsPbBr₃ nanocomposites in polystyrene matrix for their easy classification, transport, and storage. Each sample is labelled with the concentration of the added compounds to the base according to the final weight and with the date of production of the sample during the year 2022. The label '3&3 dr.' stands for use of 3 and 3 drops of the catalysts RP-128 and MEKP, respectively, compared to the use of 2 and 2 drops of RP-128 and MEKP for all of the other samples.



Figure 3.14: Box containing the produced CsPbBr_3 nanocomposites in silicone matrix for their easy classification, transport, and storage. Each sample is labelled with the concentration of the added compounds to the base according to the final weight and with the date of production of the sample during the year 2022.

Chapter 4

Design and implementation of a test bench

This chapter presents the setting up of a test bench for the characterisation of scintillator materials. It provides a description of the set-up and suggests two options of the signal generation: vertical cosmic-ray muons and irradiation with a laser source.

4.1 General idea and purpose

The test bench serves as a set-up, where the properties of scintillation materials can be measured. It comprises a dark box, high-voltage sources and read-out electronics. The dark box contains custom designed 3D-printed modules for the scintillators (designed by us specifically for this set-up and printed in our laboratory) and the PMTs. The modules are designed to be compatible with small scintillator samples with dimensions around $2.5 \times 2.5 \times 1 \text{ cm}^3$. The main role of the test bench is to measure the performance of both commercial and custom-made scintillators. The former includes samples of BC-420 and BC-499-90 made by Bicron, which are the two scintillators used in FDD. The latter comprises scintillator composites with CsPbBr_3 nanocrystals embedded in polystyrene and silicone matrices as well as the pure matrices; all these samples were described in Chapter 3.

The idea behind the test bench is the following: generate a light signal in the scintillator, transform it into an electrical signal with the PMT and then measure the signal properties, such as the signal amplitude, signal charge, time response, or time width. These properties provide a way to characterise and compare the performance of the whole system.

4.2 Description of the set-up

4.2.1 Custom 3D printed module

The core of the set-up is a 3D printed module that encapsulates the scintillator sample and the read-out PMT. The module is shown in Fig. 4.1. Picture A shows the assembled module, which contains the PMT and the sample. In order to exchange the sample and potentially the PMT, the module can be opened as shown in picture B. Picture C displays a part of the module including an insertable piece which holds the scintillator sample. The insertable part can be made in different geometries and sizes, so the tested scintillator fits in and couples well to the photocathode of the PMT. All faces but one of the tested samples are covered with two layers of 0.2 mm thick teflon tape RS PRO White PTFE as shown in pictures D, E and F.

The module was engineered in such a way, that it is possible to stack multiple units of them on top of each other in order to be able to implement a coincidence trigger on vertical muons. The insertable part also allows to couple a laser fibre to the scintillator sample, which is a parallel for the coupling of the LCS laser fibre to the FDD scintillator pad discussed in Sec. 1.5.3. Special attention was paid during the design of the module in order to avoid any stress on the PMT because of its delicacy.

4.2.2 Dark box

Together with the 3D-printed custom module, a dark box is an essential part of the set-up. The dark box is together with the aluminium box shown in Fig. 4.2. It provides protection against incoming photons, that could eventually hit the PMT photocathode and generate unwanted background. Excellent insulation is needed in order to reduce the background to the minimum as the PMTs have the ability to detect even a single photon. To this end, multistage insulation is used starting from the 3D-printed module itself, the aluminium box, multiple layers of black felt, the dark box and again multiple layers of black felt.

The custom-made aluminium box was built in order to reduce the noise of the PMTs. As the PMTs are extremely sensitive and delicate devices, it is needed to reduce the background to the minimum so that the signal produced by the PMTs is a real signal and not noise. The aluminium box features a patch panel through which all of the cables are connected. In order to reduce the noise level of the PMTs even more and avoid electrical crosstalk between the PMTs, a metal cable mesh was used in all the cables of the PMTs as shown in picture A of Fig. 4.1.

4.2.3 Read-out electronics

In order to extract the signal from the PMTs and prepare it for subsequent analysis, read-out electronics hosted in a CAEN VME 8010 crate [44] are used. The read-out electronics is together with the HV sources listed here:

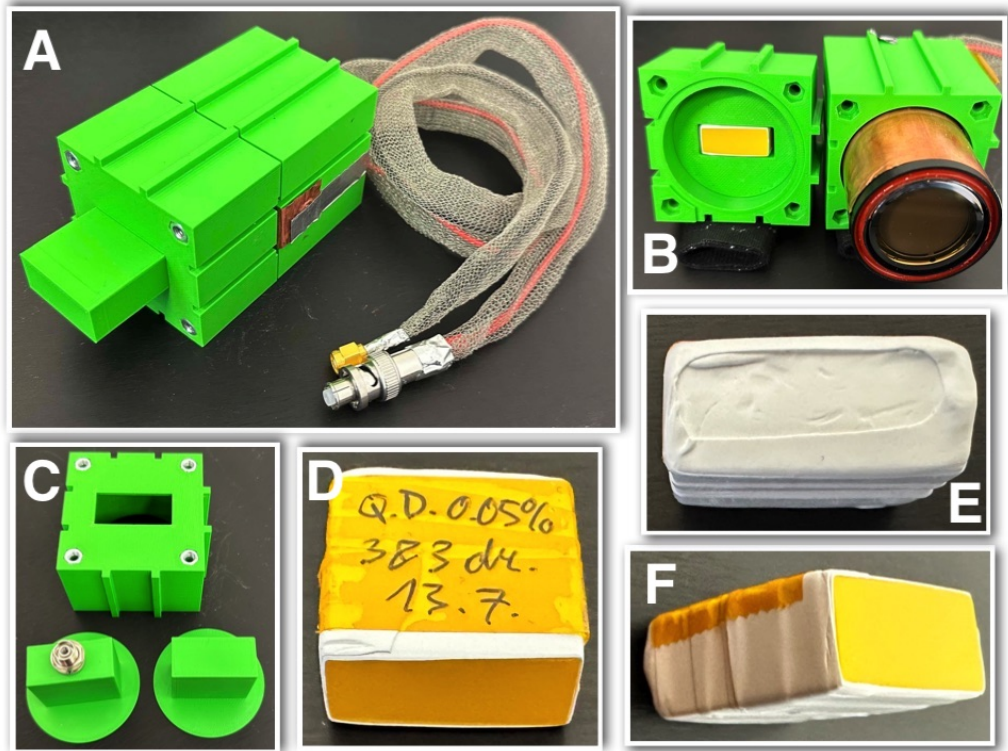


Figure 4.1: Custom 3D-printed module for scintillator characterisation: A) assembled module containing a PMT and a scintillator sample, B) open module with space for the PMT on the right-hand side and an insertable part with the scintillator sample on the left, C) detail of the insertable parts with the laser coupling of the bottom left, D), E), F) detail of the sample covered with two layers of 0.2 mm thick teflon tape RS PRO White PTFE.

- **Threshold discriminator**

A CAEN V814 16 channel low threshold discriminator (fourth from the left in Fig. 4.3) was used to trigger on signals higher than an individually adjustable threshold. The output of this discriminator is also programmable [45].

Because some problems during the data-taking occurred and they were likely caused by an error of the V814 discriminator, some of the performed runs were executed using a CAEN N840 8 Channel Leading Edge Discriminator, which served as an alternative [46].

- **Digitiser**

A CAEN V1742 digitiser (second from the left in Fig. 4.3) was used to sample the signal from the PMTs. The used sampling rate was 5 GS/s (5 giga samples per second) [47].

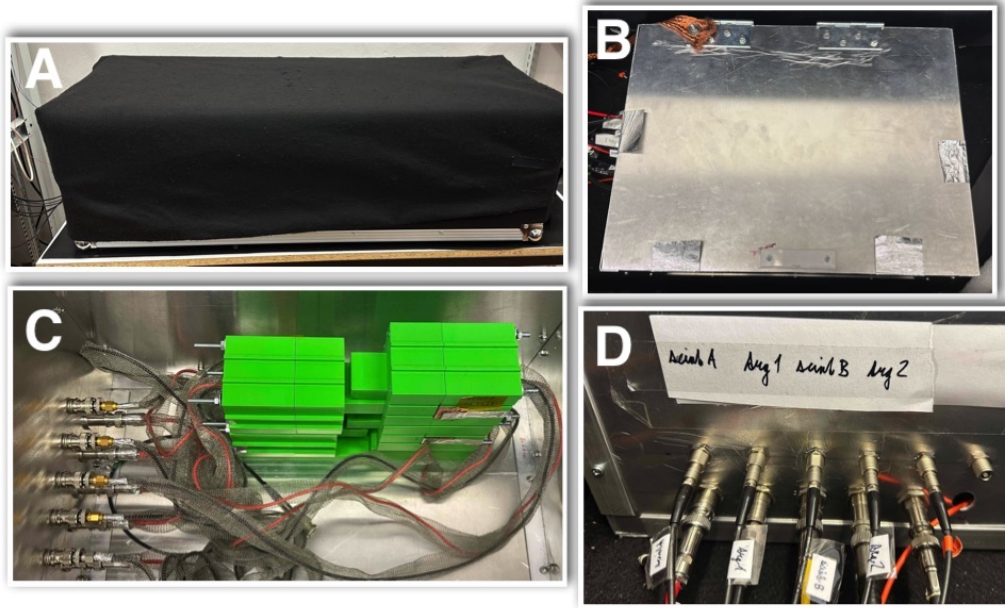


Figure 4.2: Dark box of the test bench: A) covered dark box from the outside, B) custom-made aluminium box for noise reduction, C) inside of the aluminium box containing the 3D-printed modules for scintillator characterisation, D) detail of the patch panel used for power supply of the PMTs and their signal outputs.

- **VME bridge**

As the V1742 digitiser uses the VMEbus protocol, a CAEN V1718 VME bridge (first from the left in Fig. 4.3) was used to provide the communication with the PC, where the sampled raw data is stored [48].

- **Fan-in fan-out**

A CAEN V925 Quad Linear fan-in fan-out (fifth from the left in Fig. 4.3) was used during the testing of the set-up. The signal output from the PMTs was fed to the input of the fan-in fan-out and one of the outputs was checked in the oscilloscope, while another output was coupled to the digitiser and then to the PC [49].

- **High-voltage sources**

The photomultiplier tubes were powered by independent HV sources with high voltages ranging from 1200 V to 2200 V. The used HV power supply models were 556 by ORTEC and series 225 by BERTAN [50].

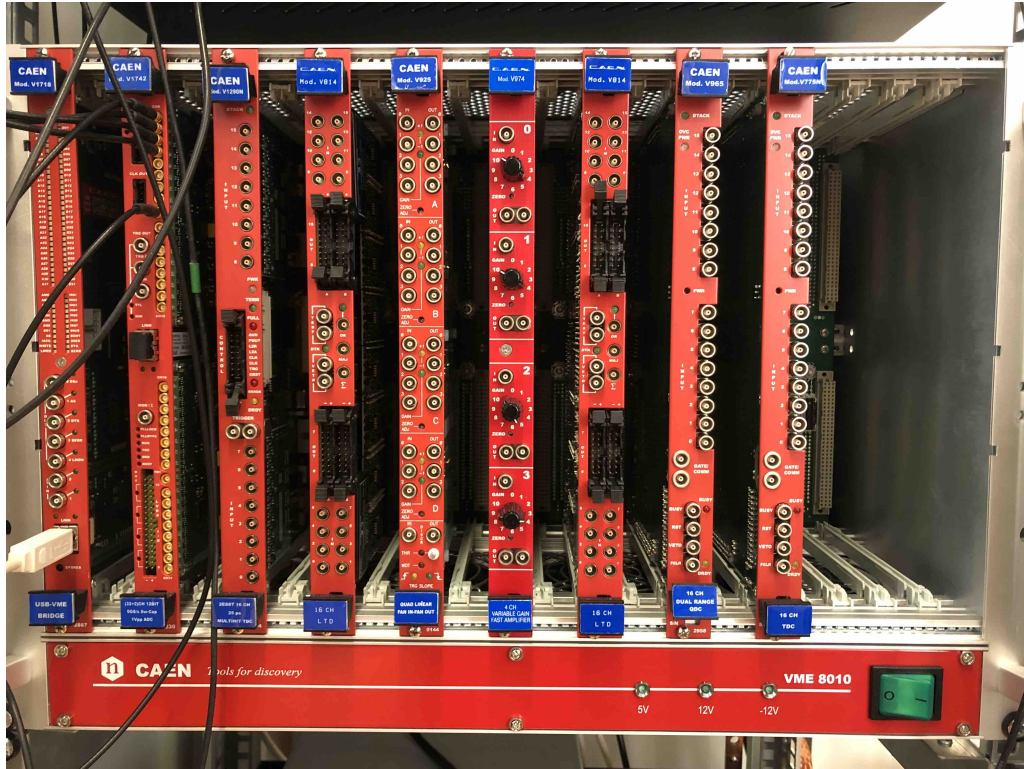


Figure 4.3: Picture of the CAEN VME crate used for the calibration. First from the left is V1718 VME bridge and second from the left is the CAEN V1742 digitiser. The rest of the components were not used in this measurement.

4.3 Generation of the signal

In order to characterise the samples, a light signal has to be generated within the scintillator and transferred to the PMT, where the electric signal is formed. For the sake of repetitiveness, the used methods for generation of the light signal are vertical cosmic-ray muons¹ and laser pulses. Each of them are further described.

4.3.1 Irradiation with vertical cosmic-ray muons

Cosmic-ray muons are widely used for calibration in HEP experiments. They provide a consistent signal if the data set is large enough and allow to be used for calibration in terms of a minimum-ionising particle (MIP). Typically, a pair of trigger scintillators is used in addition to the detector system: one above and one below the system. If one looks at events which come in the same time interval from the scintillators, i.e. coincidence, it is most likely that these are vertical cosmic-ray muons, which hit not only the trigger scintillators, but also the detector in between. In this way muon events can be selected eliminating the background.

¹Cosmic-ray muons are muons produced by the decay of products of a cosmic-ray particle colliding with the atmosphere.

4.3.2 Irradiation with a laser

Another method often used to calibrate detectors, thanks to its simplicity, fast execution, and mainly easy repetitiveness, is irradiation with a laser pulse. This configuration provides a quick way to measure data with the possibility to adjust the intensity of the laser.

Such possibility was the main motivation for the addition of the LCS to the FDD (see Sec. 1.5.3) as it can be tested and calibrated only with the laser in case of no collisions and its performance over longer time periods can be easily studied.

4.4 Set-up for a test with cosmic-ray muons

The easiest test bench set-up featuring two trigger detector consists of three 3D-printed modules: a trigger on the top, the test sample in the middle, and a trigger at the bottom. In order to test more samples simultaneously, one can add another test sample between the two triggers. However, if this configuration were used, the long distance between the top and bottom triggers would cause significant reduction of the rate of cosmic-ray muons. This problem is more serious when the area of the samples is as small as $2.5 \times 2.5 \text{ cm}^2$. To this end, the geometry of the set-up was first slightly adjusted according to Fig. 4.4, that is in a way that only one of the samples was between the triggers and the other one was put below.

Nevertheless, it was found out, that the self-absorption of the samples containing the CsPbBr_3 nanocrystals was too large, so the set-up was accordingly adapted. In pursuit of achieving more signal from such samples, the module was geometrically adjusted so more muons pass near the photocathode of the PMT. This corresponds to a change from Fig. 4.5a to Fig. 4.5b. In this way, the photons created in the sample scintillator have a higher chance of reaching the photocathode as they are created near to it. With high self-absorption, it is more probable that the photons created deeper in the sample would get absorbed and none of them would reach the photocathode, hence no signal would be produced.

There is a side effect to the set-up adjustment: there is a non-zero rate of vertical cosmic-ray muons that produce coincidence signal in the triggers, but they do not pass through the measured samples due to geometry. Such positioning introduces more background to the data, yet it helps to increase the rate of vertical muons exciting the scintillator samples near the photocathode. As will be discussed in the next chapter, it is extremely important to understand the signal from the PMTs attached to the samples being tested, as it can be produced by muons directly hitting the PMT photocathode, by dark current, electrical crosstalk, optical crosstalk, and other similar experimental issues.

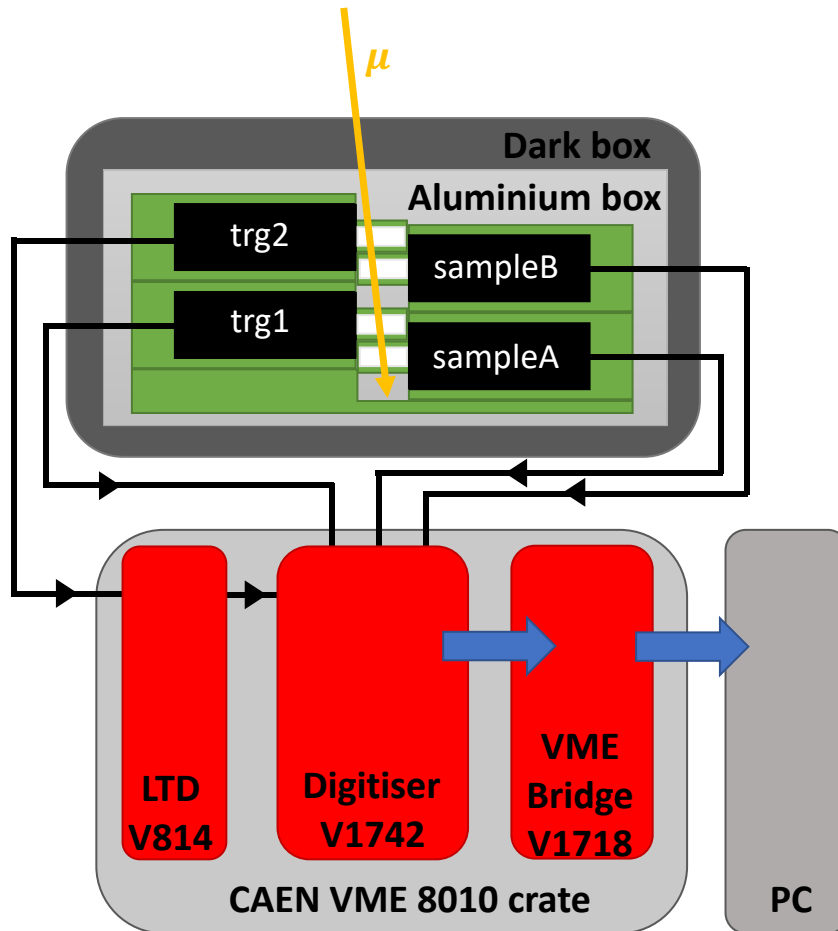


Figure 4.4: Schematic diagram of the test bench for scintillator characterisation using cosmic-ray muons.

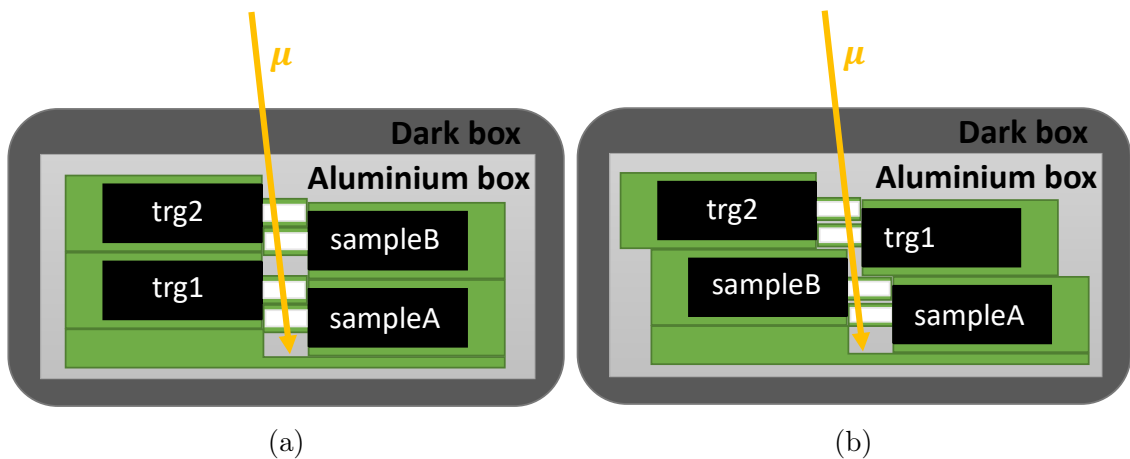


Figure 4.5: Set-up used for scintillator characterisation, detail of the sample placement: a) before and b) after the adjustments to achieve better signal. The shift of the set-up is not up to scale as it is exaggerated for illustration purposes.

Chapter 5

Performance of the custom-made scintillators

This chapter provides information about performance studies of the custom-made scintillation materials with cosmic-ray muons. The experimental set-up, data-taking and data analysis is discussed together with the results of the scintillator performance based on their composition and the supply voltage of the PMT.

5.1 Scintillator characterisation

The scintillator samples produced in Mexico during the summer of 2022 as described in Chapter 2 were characterised using the test bench described in Chapter 4. For their characterisation, only the method with vertical cosmic-ray muons was used. It was chosen as the better method to start with, as it seemed more straightforward and we already had vast experience with it. However, it turned out, that this method accepted a large quantity of background events. As these measurements take several days due to the extremely small rate of cosmic-ray muons, a large amount of time was invested to have satisfactory results. This precluded to utilise the set-up with laser pulses.

Due to the mentioned reasons, only the characterisation with cosmic-ray muons was performed and the characterisation with a laser pulse is work in progress. Unlike for the cosmic-ray muons, once the laser set-up is properly tested and adjusted, the measurement itself is quite fast as one can set the laser frequency above 1 kHz providing solid statistics in a few minutes.

5.2 Scintillator characterisation with cosmic-ray muons

5.2.1 Experimental set-up and data-taking details

The scintillator characterisation was done with the set-up introduced in Sec. 4.4. As for the triggers, two $2.5 \times 2.5 \times 1$ cm³ samples of commercial material BC-420 by Bicron were used. The used PMTs were the same as for FDD, that is Hamamatsu photomultiplier tube assembly H8409-70 with a built-in R7761-70 PMT. The details of the serial number for each module is summarised in Table 5.1. The PMT sitting on the top of the set-up (module trg2) was fed with a high voltage of 1300 V, while the lower trigger (module trg1) was fed with 1200 V. The PMTs corresponding to the tested samples were fed typically with 1800 V for samples without the CsPbBr₃ nanocrystals and 2200 V for the ones containing the NC.

Module	Serial no.
sampleA	DA1417
sampleB	DA1433
trg1	DA1432
trg2	DA1345

Table 5.1: Serial numbers of the used Hamamatsu photomultiplier tube assemblies H8409-70 with a built-in R7761-70 PMTs for the scintillator characterisation using the test bench for respective 3D-printed modules.

Regarding the data-taking, it all starts with the trg2 module, which is located on the top of the set-up. If a signal exceeding the level of 8 mV is recorded (determined by the CAEN V814 LTD as described in Chapter 4), the data from all channels is sampled by the CAEN V1742 digitiser. The reason to select 8 mV is to avoid crosstalk (see Appendix A). The sampled data is then transferred through the CAEN V1718 VME Bridge to the PC, where the raw data from the PMTs is stored.

5.2.2 Analysis of the raw data

The raw data obtained from the PMTs with the read-out electronics was analysed with a custom program. The program opens the raw-data file and produces event-by-event plots of the signals as shown in Fig. 5.1. On the left side, one can set the parameters for the data analysis: a time window, when the signal is expected and within which the charge is integrated (signal time GATE, ns) and the minimum required signal amplitude for the event to be analysed. The used parameters are summarised in Table 5.2. The time windows were selected in such a way that they cover the range where the signal was expected only. If one would cover the whole time window from 0 to 200 ns, the charge integration could be skewed by other phenomena providing misleading results of the analysis.

After setting of the parameters, one can process the data with the "CALCULATE DATA" button. A new window pops up, where one or multiple channels can be

module	t_b (ns)	t_e (ns)	A_{\min} (mV)
sampleA	65	110	0
sampleB	60	110	0
trg1	65	120	0
trg2	80	120	5

Table 5.2: Summary of the parameters used for the analysis, where t_b represents the begin time of the expected time window of the signal, t_e represents the end time of this window, and A_{\min} refers to the minimum required amplitude for the event to be analysed for the respective modules.

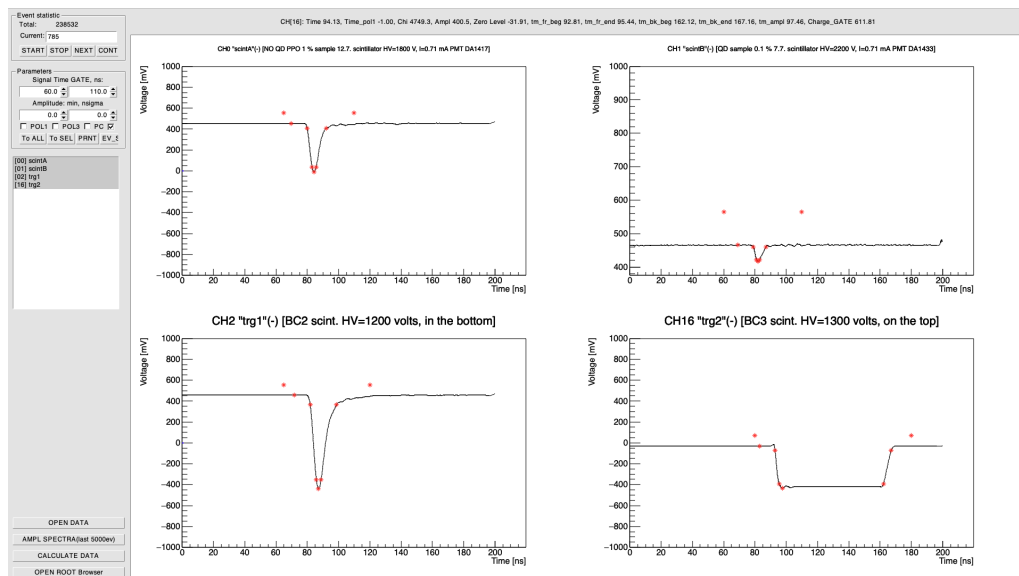


Figure 5.1: Program for the analysis of the raw data from the scintillator characterisation with cosmic-ray muons with an example of an event with coincidence in all of the channels.

chosen for the selection of the data based on A_{\min} . In this case, only the trg2 channel was chosen. Afterwards, the program goes over the data event by event to see whether they fulfill the requirement on A_{\min} and calculates the following signal properties in the selected time windows for all of the channels: time begin, time end, amplitude, and charge (integral of the area within the time window).

The output of the program is a root file, which contains signal properties for every single event. Due to the character of the measurement and the data analysis, the calculated charge is always only relative. If one wants to calculate the absolute charge produced by the minimum-ionising particle (MIP), it is required to extract the "zero level", also called the pedestal, from the data. The pedestal corresponds to the noise level, where no signal is produced by the scintillator nor the PMT. The pedestal charge corresponds to the integrated area in a given time gate, while the pedestal amplitude is the highest peak in the time gate.

The analysis of the preprocessed data files is done with another macro using the

ROOT framework [51].

5.2.3 Data analysis

Crosstalk and coincidence selections

The main interest of the analysis is the charge produced by the passing muons in the scintillator. To this end, the charge distributions of the respective samples are analysed. As discussed earlier, it is crucial to understand the background of the PMTs and subtract it from the recorded signal. To this end, two different conditions were applied to the measured distributions: the crosstalk and the coincidence selections. The crosstalk requirement selects only events, which have sufficient amplitude in order to avoid accounting for the data arising from electrical crosstalk between the channels. Thanks to the coincidence selection, only events that are registered in coincidence with both of the triggers at the same time are considered for further analysis.

A dedicated test was performed for the electrical crosstalk between the channels. It is described in detail in Appendix A. The resulting minimum signal amplitude used for the analysis was determined from the crosstalk test to 8 mV.

5.2.4 Coincidence selection

In order to select events with signal coincidence in both of the triggers, one can impose a condition on the signal properties in the trg1 module. This can be done in two ways: either a threshold for the signal amplitude or charge is used. However, as a noise event can produce a signal with a non-zero amplitude, but integrated charge close to zero, a condition on the signal charge is more suitable for event selection. To this end, one can study the charge distribution of the trg1 module, which is consistent within the runs as the trigger scintillator, the PMT (DA1432) and its voltage stay the same at all times.

The consistency of the signal lies in a similar charge distribution, e.g. if a pedestal is located at -68 fC in the charge distribution for a given scintillator coupled to a given PMT at a given voltage, it will stay at -68 fC for the other measurement under the same conditions. However, if one would look at the data from another PMT with the same sample and the same voltage, the pedestal position might be different (e.g. at -80 fC or -40 fC) as it is given only relatively.

For the case of the trg1 module, one can expect that the signal from the PMT is very clear and comes, in vast majority, from cosmic-ray muons. The reason for this is that the commercial samples of BC-420 are very efficient, so they provide good signal to the PMT. Additionally, the PMT is fed with a relatively low voltage of 1200 V, which excludes possible contamination of the data with dark current or thermal noise.

This, in combination with the same position of the pedestal within the runs, allows us to study the trg1 charge distribution in one of the runs only and based on it take a single value as the threshold of minimum charge. The resulting minimum threshold was set to -25 fC in order to include only muon-induced events as shown in Fig. 5.2

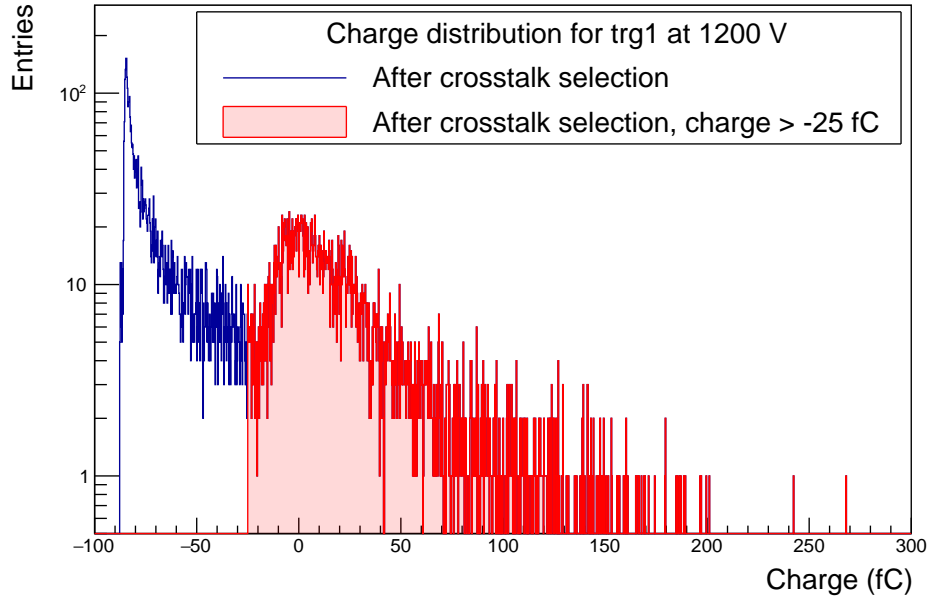


Figure 5.2: Charge distribution for BC-420 sample in module trg1 at 1200 V. The blue line represents the distribution after the crosstalk selection, the red area shows events after the crosstalk selection and with a charge higher than -25 fC.

5.2.5 Charge distribution

An example of the charge distribution for one of the produced samples is shown in Fig. 5.3. The blue line represents the charge of all of the measured events, while the filled area shows the events that remained after the aforementioned crosstalk and coincidence selections. In the right corner, the information about the measured samples is provided together with the voltage of the used PMT. Below that, the run number is specified together with its duration.

In order to achieve the final charge distribution produced by the scintillator sample, one has to subtract the charge distribution of the PMT background. For this, dedicated runs were performed with the same geometry, voltages and parameters for the data analysis. The only difference is that the scintillator samples were left out of the 3D-printed modules, only the trigger modules were complete with the BC-420 scintillators attached to the PMTs. The charge distribution from the corresponding PMT background is shown in Fig. 5.4. As the charge distributions are measured relatively, the background was always shifted so it matched the distribution of the signal runs, the shifts were performed according to the maximum value.

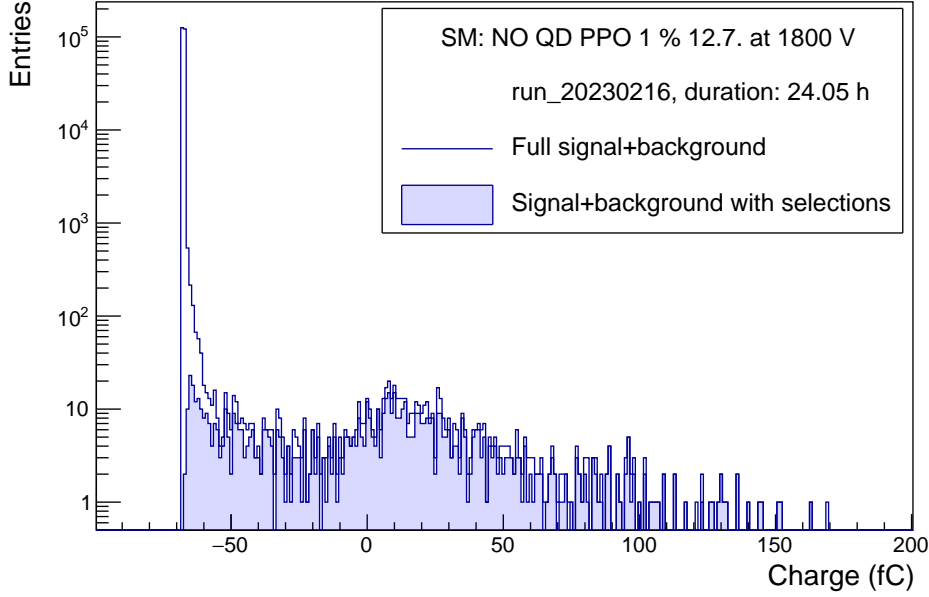


Figure 5.3: An example of a charge distribution measured with a custom-made scintillator. The blue line represents the full distribution, while the blue area shows events after the crosstalk and coincidence selections.

Background subtraction

The final charge distribution of the signal is in Fig. 5.5, where the rate per hour with respect to the charge of the signal is shown. For this particular composite of the silicone matrix (SM) with the addition of 1 % of PPO, but no added CsPbBr₃ NC (NO QD), one can see a clear MIP peak after the subtraction of the PMT background. However, this is not the case for the samples containing the QD. In order to represent the measured signal from the scintillators, the effective rate of muons R_{eff} per hour is used. The effective rate is given by the sum of the entries within a selected charge window (charges above -53 fC for this particular case) normalised with the run duration.

For the shown configuration, the effective rate of muons per hour for the signal+background is $R_{eff,S+B} = (26.5 \pm 1.0)$ 1/h, while for the background only it is $R_{eff,B} = (6.8 \pm 0.5)$ 1/h. Hence, the change in the effective ratio shows, that the scintillator coupled to the PMT detects the cosmic-ray muons.

5.3 Scintillator performance based on their composition

With multiple samples of different constitution and concentrations, one can study what is the role of the different components in the composite, mainly how it changes

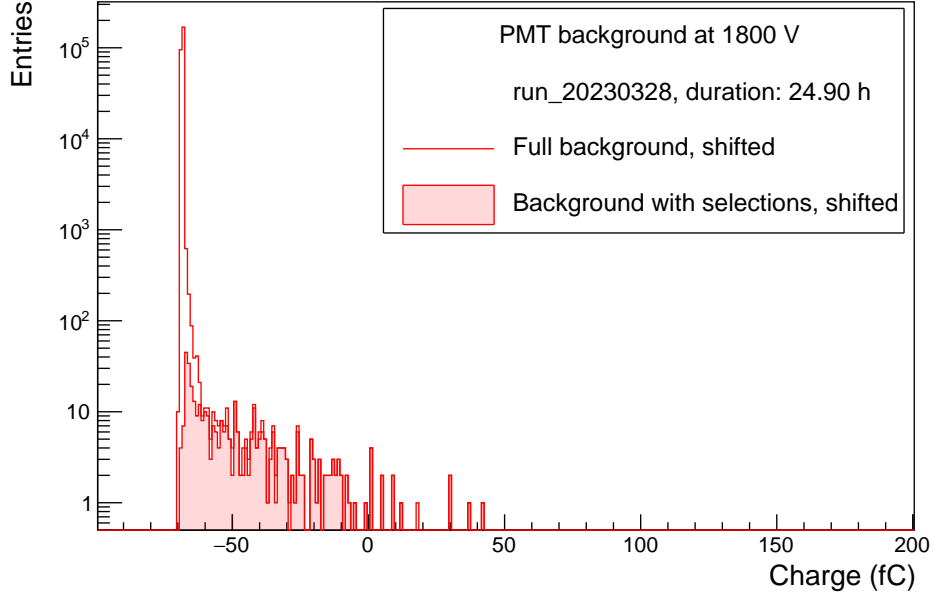


Figure 5.4: An example of a charge distribution measured with a PMT only in a background run. The red line represents the full distribution, while the red area shows events after the crosstalk and coincidence selections. The distributions are shifted using the maximum value to match the signal distribution (run with a scintillator) at the same voltage.

the effective rates R_{eff} and the respective charges of the signal.

In order to study only the effect of the sample composition, other parameters of the data-taking and the data analysis must stay as identical as possible. To this end, a number of runs with scintillator samples was performed with the same module at the same supply voltage, together with one common run studying the PMT background. The data analysis of the samples was identical amongst the runs together with the selection of the charge integration windows.

5.3.1 Polystyrene matrix

Unlike the case of the silicone matrix, the samples with the polystyrene matrix vary mainly in the different concentration of the added QD. A summary of the characterised samples is given in Table 5.3, which includes the effective rate of muons per hour for measurements with the sample $R_{\text{eff,S+B}}$, the effective rate of muons per hour for the background measurement with the PMT only $R_{\text{eff,B}}$, and the ratio of the signal to background effective rates R_{SB} . These variables provide a way to compare the enhancement of the signal when the sample is coupled to the PMT with respect to the PMT background only. A graphical representation of the signal distributions after the background subtraction is shown in Fig. 5.6. See Appendix B for all plots from the measurements and more details about the runs.

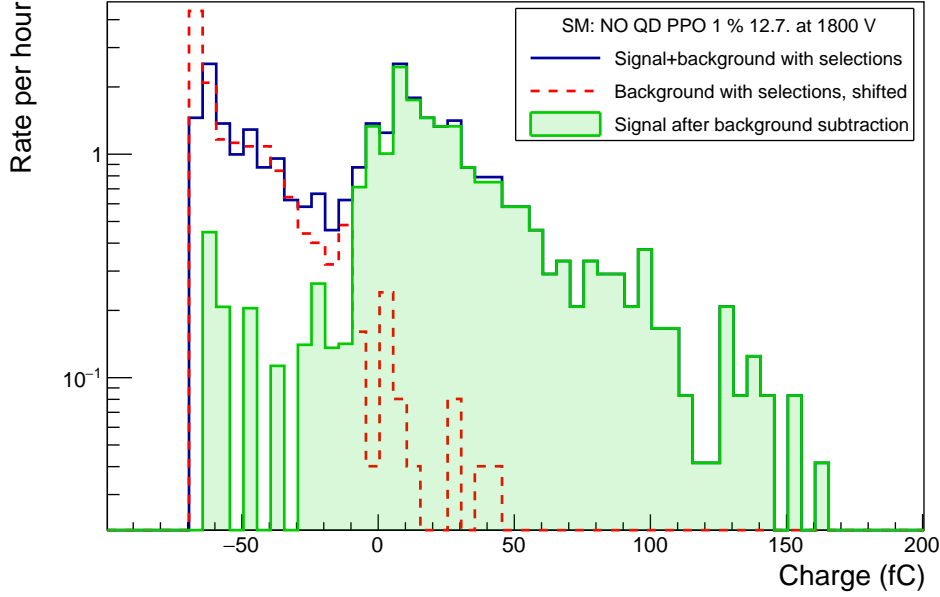


Figure 5.5: An example of a charge distribution measured with a custom-made scintillator (blue full line), PMT background (red dashed line) and their subtraction (green filled area) after normalisation with run duration.

One can see from both the effective rates and the plots, that there is only a weak enhancement of the detected signal of cosmic-ray muons with the samples containing the CsPbBr_3 nanocrystals. An only polystyrene sample that shows a noticeable difference from the PMT background is the one with no QD added (NO QD 3&3 dr.). One can see that in the region of very low charges, just next to the pedestal, there seems to be a peak arising from the cosmic-ray muons. However, the charge of these signals is very low and a further study would have to be performed to confirm this hypothesis.

It can also be noticed, that for the three polystyrene samples with the highest QD concentrations (0.1 %, 0.2 %, and 0.3 %), the R_{SB} shows an increasing trend with the increase of the QD concentration. However, if one looks at the R_{SB} of the sample with 0.05 % QD concentration, it is higher than one would expect from the observed trend. This might be an effect of the extra addition of the two catalysts, RP-128 and MEKP.

5.3.2 Silicone matrix

To study the difference in the effective rate R_{eff} and the charge distribution with respect to the silicone sample constitution, 4 samples with the following properties were chosen:

- no QD nor PPO added to the silicone matrix,

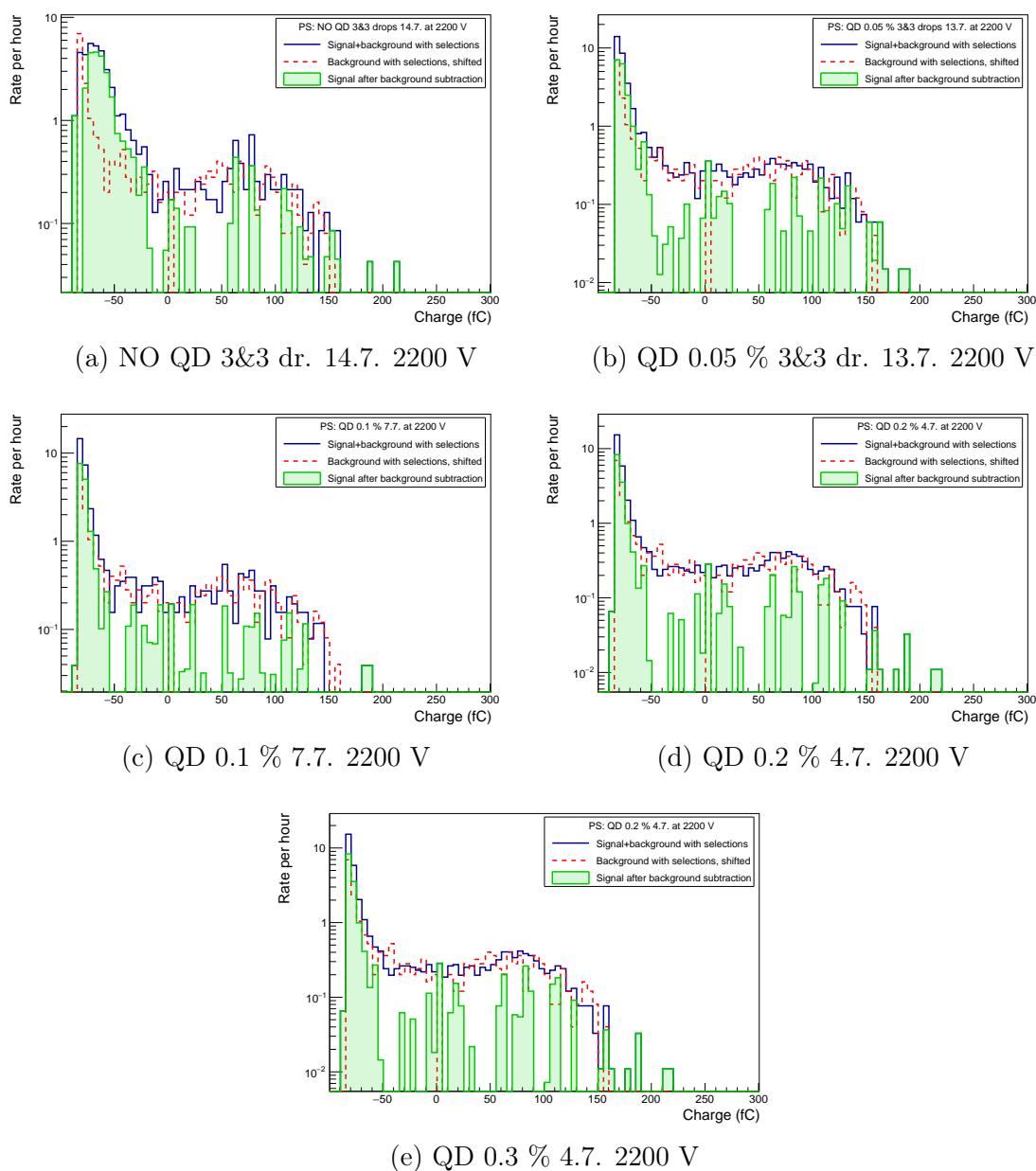


Figure 5.6: Charge distributions of the signal after background subtraction for different QD concentration of the samples with the polystyrene matrix measured with the sampleB module at 2200 V. The note '3&3 drops' stands for use of 3 and 3 drops of the catalysts RP-128 and MEKP, respectively, compared to the use of 2 and 2 drops of RP-128 and MEKP for all other polystyrene samples.

Characterised sample	$R_{\text{eff,S+B}}$ (1/h)	$R_{\text{eff,B}}$ (1/h)	R_{SB}
NO QD 3&3 dr. 14.7.	9.5 ± 0.6	7.7 ± 0.6	1.23 ± 0.12
QD 0.05 % 3&3 dr. 13.7.	9.0 ± 0.4	7.7 ± 0.6	1.17 ± 0.10
QD 0.1 % 7.7.	8.7 ± 0.6	7.7 ± 0.6	1.12 ± 0.11
QD 0.2 % 4.7.	9.0 ± 0.3	7.7 ± 0.6	1.16 ± 0.09
QD 0.3 % 4.7.	9.2 ± 0.5	7.7 ± 0.6	1.19 ± 0.11

Table 5.3: Summary of the characterisation of the polystyrene samples with different concentrations of the added QD at 2200 V, where $R_{\text{eff,S+B}}$ denotes the effective rate of muons per hour for measurement with the sample, $R_{\text{eff,B}}$ denotes the effective rate of muons per hour for the background measurement with the PMT only, and R_{SB} is the ratio of the signal to background effective rates. The note '3&3 drops' stands for use of 3 and 3 drops of the catalysts RP-128 and MEKP, respectively, compared to the use of 2 and 2 drops of RP-128 and MEKP for all other polystyrene samples. The effective rate of the background is obtained with a background run, that is common for all of the samples.

- no QD, PPO 1 %,
- QD.005 %, no PPO,
- and QD.01 %, PPO 1 %.

For the silicone samples, the charge distributions of the signal after background subtraction are shown in Fig. 5.7 and the corresponding effective rates are summarised in Table 5.4. See Appendix C for all plots from the measurements and more details about the runs. One can see, that the pure matrix effectively detects cosmic-ray muons, but due to the low light yield of the matrix itself, the signal charge is relatively low, which is close to the charge of the pedestal. However, as the PPO is added to the matrix, the $R_{\text{eff,S+B}}$ even increases and one can observe, that the charge produced by the muons is much higher, making it more distinguishable from the pedestal.

If the QD (CsPbBr_3 nanocrystals) are added to the composite, one can notice a huge drop in the $R_{\text{eff,S+B}}$ compared to the samples without them. This effect most probably arises from the self-absorption of the QD, which attenuate the light produced by the matrix. Majority of the signal events also lie in the low charges. Once the PPO is added to the composite with the QD, the $R_{\text{eff,S+B}}$ is decreased even less; however, the signal events have increased charge compared to the signal with QD only.

In general one can observe, that the R_{SB} for the pure silicone matrix is much higher than for the pure polystyrene matrix, hence the silicone matrix seems to produce much more light.

Characterised sample	$R_{\text{eff},S+B}$ (1/h)	$R_{\text{eff},B}$ (1/h)	R_{SB}
NO QD NO PPO 12.7.	25.5 ± 0.6	6.8 ± 0.5	3.74 ± 0.30
NO QD PPO 1 % 12.7.	26.5 ± 1.0	6.8 ± 0.5	3.88 ± 0.33
QD 0.005 % NO PPO 7.7.	10.1 ± 0.4	6.8 ± 0.5	1.48 ± 0.13
QD 0.01 % PPO 1 % 6.7.	8.9 ± 0.4	6.8 ± 0.5	1.31 ± 0.11

Table 5.4: Summary of the characterisation results for the silicone matrix samples with different constitution at 1800 V, where the characterised sample is described, $R_{\text{eff},S+B}$ denotes the effective rate of muons per hour for measurement with the sample, $R_{\text{eff},B}$ denotes the effective rate of muons per hour for the background measurement with the PMT only, and R_{SB} is the ratio of the signal to background effective rates. The effective rate of the background is obtained with a background run, that is common for all of the samples.

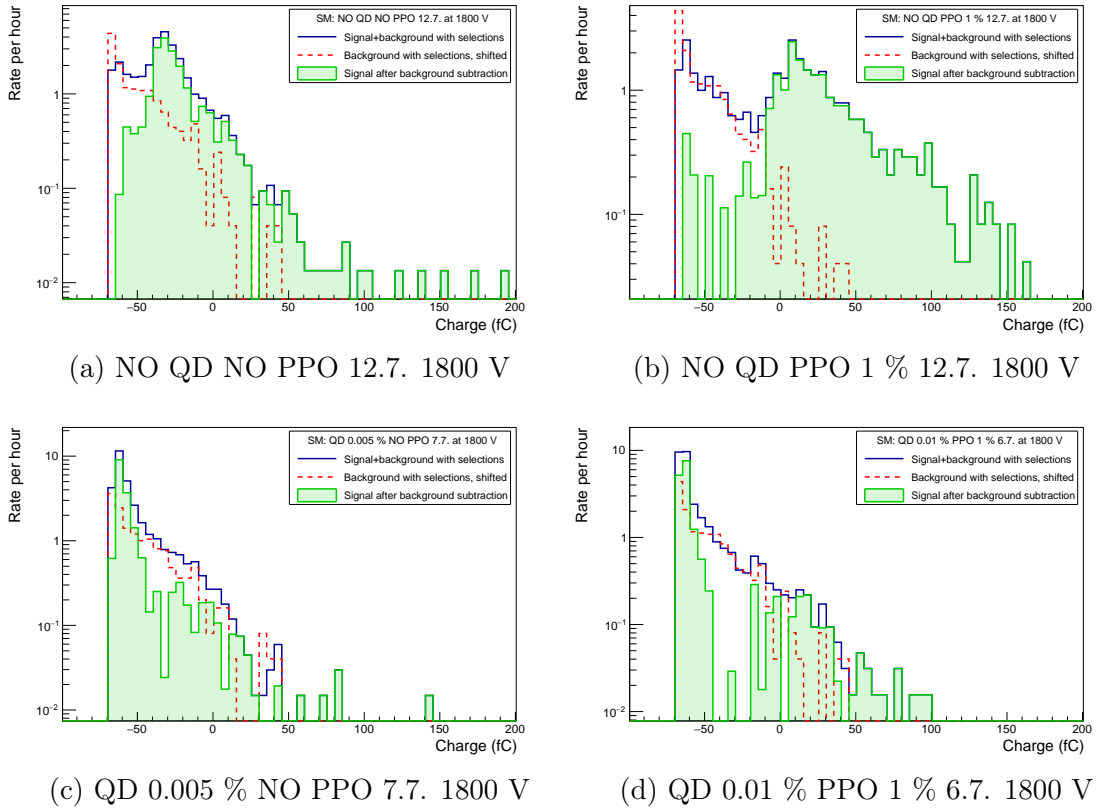


Figure 5.7: Charge distributions of the signal after background subtraction for different constitution of the samples with the silicone matrix measured with sampleA module at 1800 V.

5.4 Scintillator performance based on the PMT supply voltage

With increasing supply voltage of the PMTs, one expects an increase in the observed charge of the muon signals. A comparison of the two silicone samples without QD at voltages of 1800 V and 2000 V is given in Table 5.5 and Fig. 5.8. Clearly, there is an increase of the charge observed as well as an increase of the effective rate at higher voltage. This is a reassurance that the observed peak comes from cosmic-ray muons.

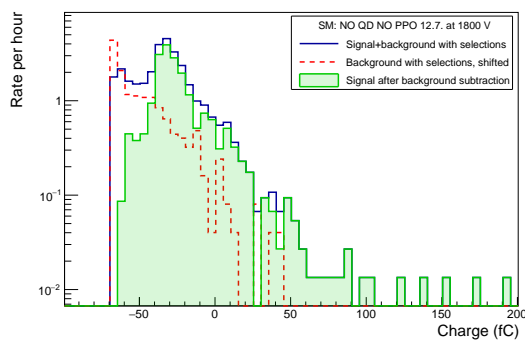
One can extract the mean charge value of the pedestal from its Gaussian distribution as $Q_{\text{ped}} = (-67.4468 \pm 0.0007)$ fC. The mean MIP relative position for the NO QD NO PPO 12.7. sample is acquired from a Landau fit as $Q_{\text{rel},1800 \text{ V}} = (-34 \pm 2)$ fC and $Q_{\text{rel},2000 \text{ V}} = (17 \pm 4)$ fC for supply voltages of 1800 V and 2000 V, respectively. This results in a total MIP charge of $Q_{1800 \text{ V}} = (33 \pm 2)$ fC and $Q_{2000 \text{ V}} = (84 \pm 4)$ fC. A similar study can be repeated for the NO QD PPO 1 % 12.7. which yields the following results: $Q_{\text{rel},1800 \text{ V}} = (-12 \pm 5)$ fC and $Q_{\text{rel},2000 \text{ V}} = (109 \pm 6)$ fC for supply voltages of 1800 V and 2000 V, respectively. The total MIP charge is then $Q_{1800 \text{ V}} = (79 \pm 5)$ fC and $Q_{2000 \text{ V}} = (176 \pm 6)$ fC. One can try to estimate a gain of the used PMT with the ratio of these two values for the different samples. For the NO QD NO PPO 12.7. sample, the ratio yields a value of $R_{\text{gain,NO PPO}} = 2.5 \pm 0.2$, while for the NO QD PPO 1 % 12.7. sample it is $R_{\text{gain,PPO 1 \%}} = 2.2 \pm 0.2$. One can see that a good agreement within the errors is obtained. Of course, comparison at 2 voltages only is insufficient for a conclusive result, but it works rather as a cross-check quite well.

Characterised sample	HV (V)	$R_{\text{eff,S+B}}$ (1/h)	$R_{\text{eff,B}}$ (1/h)	R_{SB}
NO QD NO PPO 12.7.	1800	25.5 ± 0.6	6.8 ± 0.5	3.74 ± 0.30
NO QD NO PPO 12.7.	2000	28.0 ± 1.0	8.4 ± 0.5	3.35 ± 0.21
NO QD PPO 1 % 12.7.	1800	26.5 ± 1.0	6.8 ± 0.5	3.88 ± 0.33
NO QD PPO 1 % 12.7.	2000	30.7 ± 1.1	8.4 ± 0.5	3.67 ± 0.23

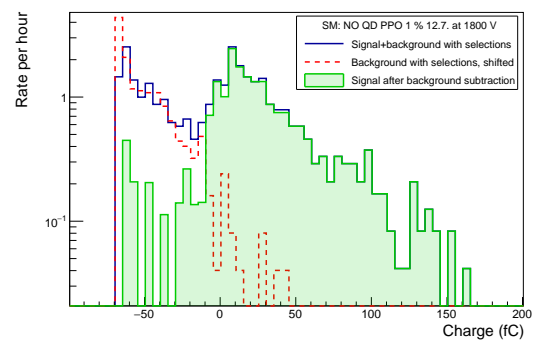
Table 5.5: Summary of the characterisation results for the silicone matrix samples with different constitution, where the characterised sample is described, $R_{\text{eff,S+B}}$ denotes the effective rate of muons per hour for measurement with the sample, $R_{\text{eff,B}}$ denotes the effective rate of muons per hour for the background measurement with the PMT only, and R_{SB} is the ratio of the signal to background effective rates. The effective rate of the background is obtained with two background runs, one for each voltage.

5.5 Summary and outlook

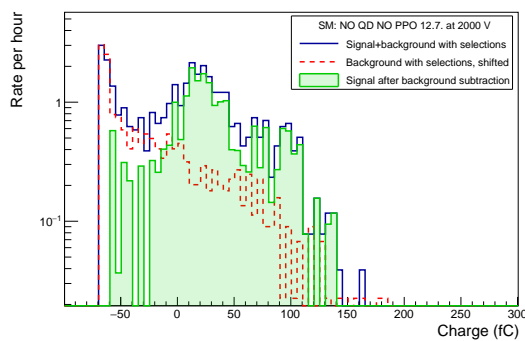
The custom-made scintillator characterisation has shown, that the signal from polystyrene samples with QD is weak probably due to self-absorption of the QD. The measurements then suffer from the small size of the data sample. In order to obtain more



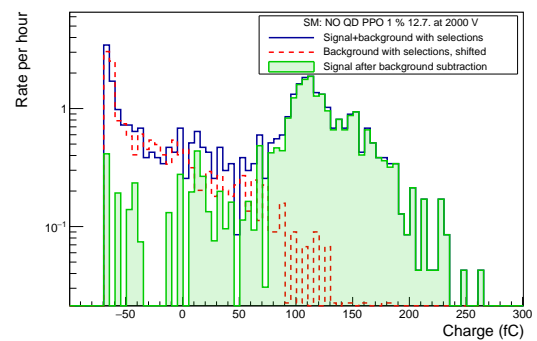
(a) NO QD NO PPO 12.7. 1800 V



(b) NO QD PPO 1% 12.7. 1800 V



(c) NO QD NO PPO 12.7. 2000 V



(d) NO QD PPO 1% 12.7. 2000 V

Figure 5.8: Charge distributions of the signal after background subtraction for different constitution of the samples with the silicone matrix.

statistics, one could use the generation of the signal with a laser. The transition to laser irradiation of the samples would be an incredible way to perform fast several-minute runs and have enough statistics to draw conclusions. It would be probably needed to design and print more suitable pieces for the custom 3D-printed modules to adjust to the high self-absorption of the samples. This is planned for the next round of measurements.

In general one can observe, that the R_{SB} for the pure silicone matrix is much higher than for the pure polystyrene matrix, hence the silicone matrix seems to produce much more light.

For the polystyrene sample with no added QD, one can observe a peak in very low charges, which probably arises from cosmic-ray muons. To confirm this, more runs at different voltages could be performed to see whether the peak changes with voltage, but as the peak is still close to pedestal at a voltage as high as 2200 V, there is not much room to go higher. Another possible way to see if the peak comes from cosmic-ray muons is to add the PPO to the polystyrene base as was done for the silicone matrix. The PPO should increase the charge of the muon signal and disentangle it from the pedestal.

Regarding the silicone samples, clear MIP peaks were observed for the scintillators with no added QD. For the pure matrix only, there is a clear MIP peak distinguishable from the pedestal; however, its charge is very low. One can see that whenever the PPO is added to the matrix, the charge produced by the muons is much higher, making it much more distinguishable from the pedestal.

If the QD are added to the composite, a large drop in the $R_{\text{eff},S+B}$ follows compared to the samples without them and the MIP peak almost completely disappears. This is most probably an effect that arises from the QD, whose addition to the composite attenuate the light produced by the matrix and the MIP peak then disappears. The majority of the signal events also lie in the low charges for the silicone sample with the quantum dots only. One can see the PPO shift the charge of the signal to higher values when it is added again, but no clear MIP peak is observed.

An increase of the mean MIP charge was successfully observed while comparing the sample performance at 2 different PMT supply voltages. The MIP peak increased consistently for two samples of the silicone matrix, namely NO QD NO PPO 12.7. sample, and NO QD PPO 1 % 12.7. sample, ensuring a correct behaviour of the set-up.

Chapter 6

Performance of the FDD

This chapter discusses the commissioning of the FDD as well as its performance. The setting up of PMT supply voltages is clarified together with the settings for the front-end electronics (FEE) of the FDD. The current status of the detector performance is mentioned together with one highlight regarding the measurement of the vertex position.

6.1 Commissioning of the FDD

After the installation of the FDD, numerous calibrations and tests were conducted prior to its commissioning. The commissioning process employed various methods, such as laser runs utilising the newly-integrated LCS, calibrations using cosmic-ray muons, or pilot beam collisions generated by the LHC. Each of these approaches allowed for the proper adjustment of the supply voltages of the PMTs, as well as the FEE parameters, which include threshold values and time gates to ensure the system operates correctly.

Tests with the laser calibration system

The integration of the LCS into the DCS system is vital for calibrating the PMTs' response to minimum-ionising particles (MIPs). It offers control over the laser's activation, as well as adjustments to the light intensity. Moreover, the LCS provides a switch to alternate between irradiating the pads and PMTs. This allows the detector to receive signals without any LHC collisions, making it possible to conduct tests and calibrations without beams. The LCS plays a crucial role in monitoring the ageing of the PMTs, scintillator pads, and optical fibers. This is important for tracking whether adjustments to the HV or FEE configuration are required to ensure stable gain and efficiency for the FDD in both pp and heavy-ion collisions. Furthermore, the LCS also conducts an electrical crosstalk test, which examines how a signal in one channel impacts the other channels. The electrical crosstalk test is further described in Appendix D.

High voltage and FEE configuration

Regarding the HV and FEE settings, proton–proton (pp) pilot beam collisions delivered by the LHC since October 2021 were used for the first calibration. During these pp collisions at various energies, FDD took part in several global runs alongside the other ALICE detectors. The high voltage was adjusted in order to get a signal of 24 ADC counts¹ per minimum-ionising particle (MIP). Due to the saturation of the signal, it was decided to lower the HV and adjust it to get a signal of 12 ADC counts per MIP. However, the adjustment of parameters at such low PMT gains was complicated, so a range of 12-16 ADC counts was chosen instead of a single value.

Nevertheless, a problem was revealed with a mezzanine board, a key part of the FDD PM module, which caused problems in the time measurement of low-charge signals. This was due to the optimisation of the PM module for FT0 detector, which features a faster PMT with a narrower time width. Consequently, the PM module was changed for a one optimised for the FV0 and FDD detectors in November 2022. However, as the PM module changed, a new set of calibrations and setting up of the parameters was needed to be performed to configure the FDD properly. A few other changes such as the addition of layer coincidence directly in the FDD firmware, which imposed recabling of the electronics connection, were performed.

The correct HV and FEE settings are valid since April 1st 2023 before the start of pp stable beam collisions.

6.1.1 HV calibration with cosmic-ray muons

In order to configure the FDD for pp or Pb-Pb collisions, first, the high voltage of the individual channels has to be set. Until February 2023, the HV calibration was done with the pilot beams delivered by the LHC in the fall of 2021. However, the high-voltage calibration with pp collisions was very difficult due to the problems while measuring time distributions at low charges caused by the non-optimised mezzanine board. As a consequence, FDD was also facing problems with high saturation of the signals because of the high supply voltages. In order to reduce this, a calibration with cosmic-ray muons with a goal to get a signal of 8 ADC counts per minimum-ionising particle (MIP) for each channel was performed. To this end, a series of cosmic runs at different high voltages was taken and analysed. The details about the runs are summarised in Table 6.1 and Table 6.2.

An example of a charge distribution for a given channel in a given run is shown in Fig. 6.1. The blue line represents all events measured by the channel PMT, the red line represents the events which are in coincidence with the second layer of the same quadrant to select vertical cosmic-ray muons and finally, the magenta line represents the layer coincidence with a condition on a minimum charge Q_{\min} in the second layer. In this way, only events arising from interaction of cosmic-ray muons with the detector are selected. A mean charge of the MIP peak is extracted for each

¹ADC unit is a digital value that corresponds to the physical measurement of the signal charge.

		FDD-C side channel HV (V)							
run ID	Q_{\min}	0_0	0_1	0_2	0_3	1_0	1_1	1_2	1_3
530631	10	1400	1400	1400	1400	1400	1400	1500	1550
530782	15	1500	1500	1500	1500	1500	1500	1600	1650
530850	20	1600	1600	1600	1600	1600	1600	1700	1750
531186	50	1700	1700	1700	1700	1700	1700	1700	1700
531185	70	1800	1800	1800	1800	1800	1800	1800	1800
531179	110	1900	1900	1900	1900	1900	1900	1900	1900
531151	150	2000	2000	2000	2000	2000	2000	2000	2000

Table 6.1: High voltage table of the respective channels of the FDD-C side for different cosmic runs denoted by run ID, Q_{\min} represents the charge selection used for the analysis. The channel notation is further described in Sec. 1.5.3.

		FDD-A side channel HV (V)							
run ID	Q_{\min}	2_0	2_1	2_2	2_3	3_0	3_1	3_2	3_3
530631	10	1420	1280	1390	1330	1310	1280	1360	1500
530782	15	1450	1450	1450	1450	1450	1450	1450	1600
530850	20	1550	1550	1550	1550	1550	1550	1550	1650
531186	50	1700	1700	1700	1700	1700	1700	1700	1700
531185	70	1800	1800	1800	1800	1800	1800	1800	1800
531179	110	1900	1900	1900	1900	1900	1900	1900	1900
531151	150	2000	2000	2000	2000	2000	2000	2000	2000

Table 6.2: High voltage table of the respective channels of the FDD-A side for different cosmic runs denoted by run ID, Q_{\min} represents the charge selection used for the analysis. The channel notation is further described in Sec. 1.5.3.

channel with a Landau fit. The analysis is repeated for all of the channels in all of the cosmic runs in order to achieve the mean MIP peak charge at each voltage.

The mean MIP peak charge with respect to voltage is shown in Fig. 6.2 and Fig. 6.3 for FDD-C side channels and FDD-A side channels, respectively. The data for each channel was fit with a power law function to acquire the mean MIP charge behaviour. This provides the possibility to choose a given value of the MIP charge in ADC counts (for our case chosen as 8) and set the corresponding high voltage to the channel.

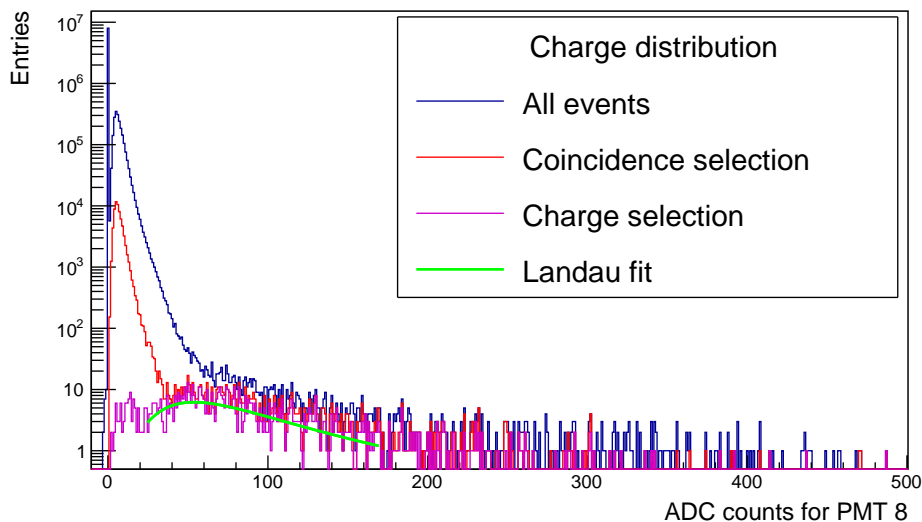


Figure 6.1: An example of a charge distribution for a given FDD channel during the HV calibration cosmic runs. The blue line represents all events measured by the channel PMT, the red line represents the events which are in coincidence with the second layer of the same quadrant and finally, the magenta line represents the layer coincidence with a condition on minimum charge Q_{\min} in the second layer. The mean MIP peak charge of the magenta distribution is extracted with a Landau fit, which is depicted by the green line.

6.2 Performance in proton-proton collisions

6.2.1 Stable-beam collisions

After commissioning of the detectors with pilot beams at various energies and optimising the acceleration procedure, the LHC delivers stable-beam collisions to all of the experiments. A part of FDD data from one such run at 900 GeV was analysed and its performance is presented in the following section. The details about this run (534265) are shown in Fig. 6.4. The filling scheme of this particular run consisted of 12 single pp bunches, out of which 8 collided in ALICE.

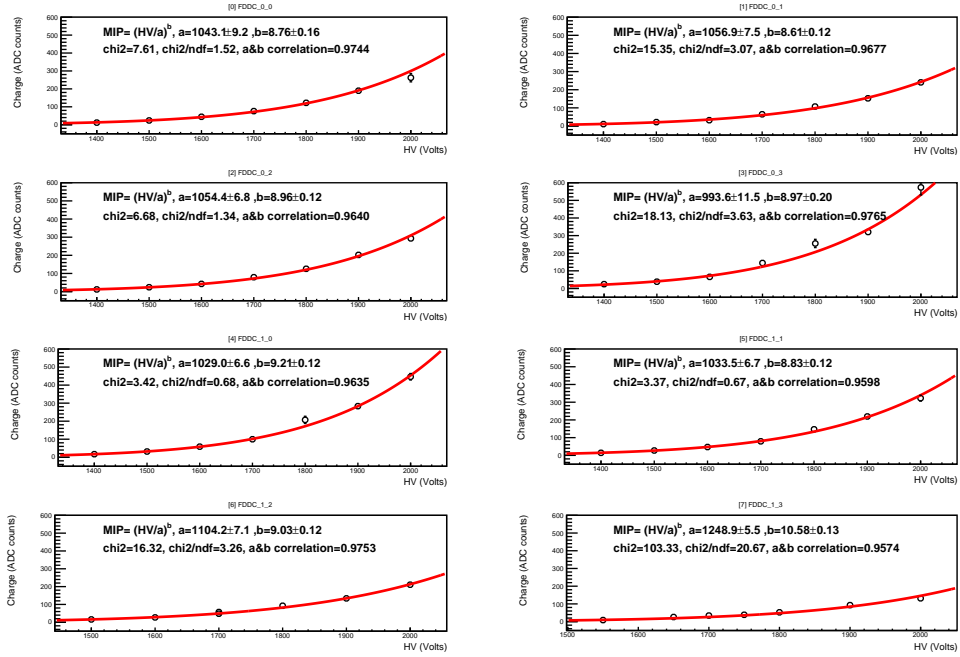


Figure 6.2: Gain curves of the FDD-C side obtained with the HV calibration with cosmic-ray muons at different supply voltages of the PMTs.

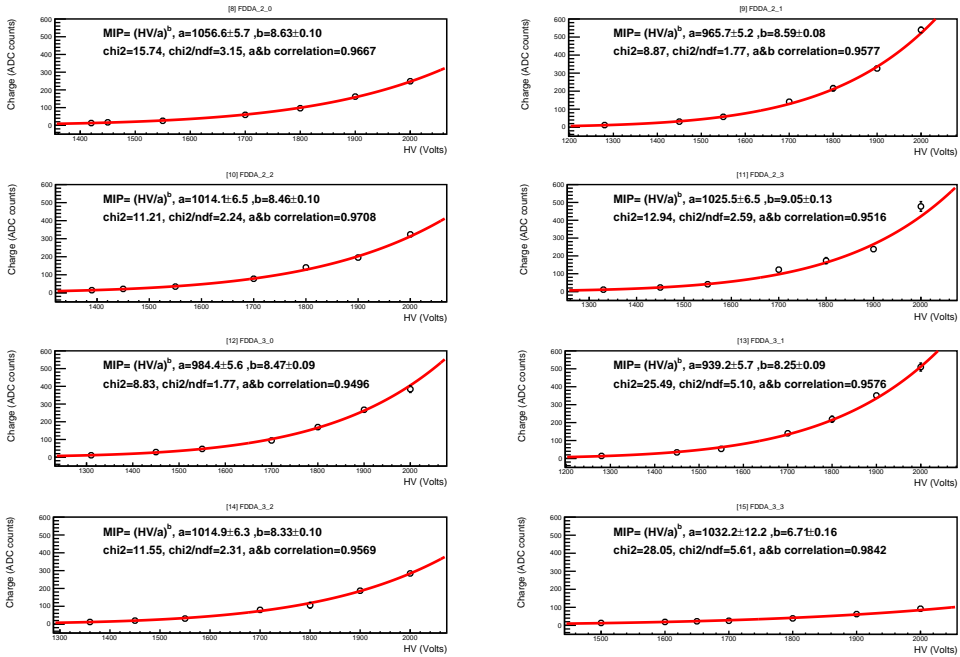


Figure 6.3: Gain curves of the FDD-A side obtained with the HV calibration with cosmic-ray muons at different supply voltages of the PMTs.

Run #534265

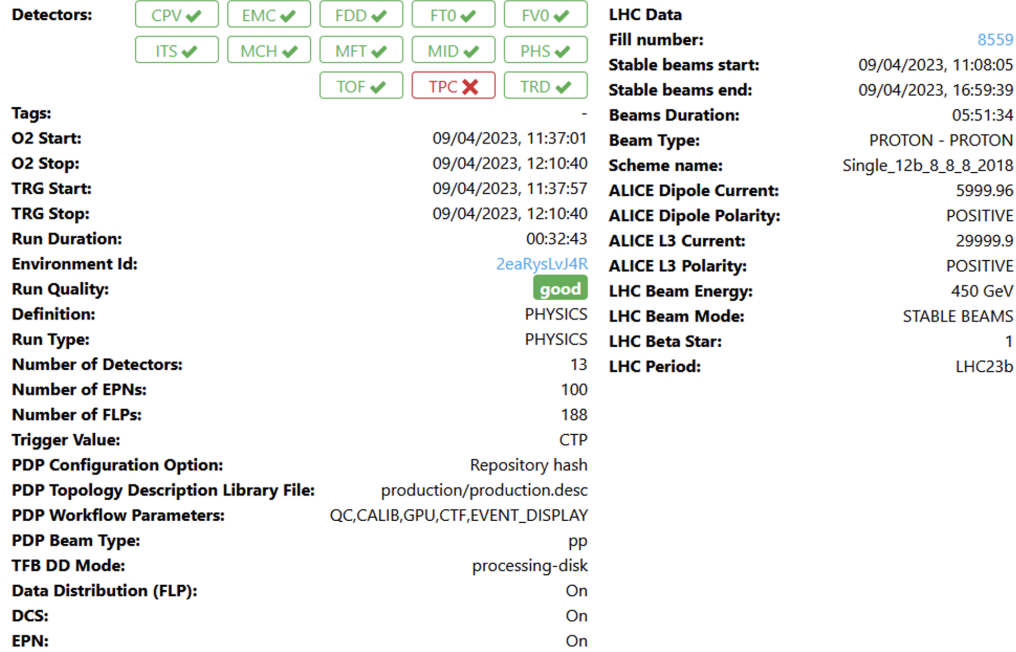


Figure 6.4: Details of run 534265.

6.2.2 Bunch crossing (BC) distributions

Each orbit made by the particle in the LHC is divided into 3564 25-ns time intervals called bunch crossings (BC). One of the most important plots from the FDD data is the BC distribution shown in Fig. 6.5, which shows the number of entries in each BC for three different selections: FDDAll, FDDOr and FDDVertex.

An entry in the FDDAll distribution comes from a registered event in any of the channels of the FDD in a certain BC with contribution from the background. An entry in the FDDOr distribution is added if the event is considered as valid, i.e. the registered event comes in the defined 5 ns window for the charge integration in any of the FDD channels. The FDDVertex distribution shows events where the signal is registered in at least one channel of FDD-A and at the same time in at least in one channel of FDD-C in the same BC. To summarise, if e.g. a noise signal is registered in any of the channels and it is outside the 5 ns integration window, it is only added to the FDDAll selection; if a signal is inside the 5 ns integration window in at least one channel on either side, it is added to the FDDOr selection; and finally, if a signal falls into the 5 ns integration window and it is registered by at least one channel on both sides of FDD in the same BC, it contributes to the FDDVertex selection.

Fig. 6.5 shows eight clear peaks in the BC distribution, which correspond to the eight colliding bunches at ALICE during the said run. In the zoomed region around BC 344 for the FDDAll selection, a structure with multiple peaks after the main peak can be distinguished. There is no final explanation for this structure yet, but there are some candidates: saturation of the signal causing afterpulses in the following BC or reflections of the signal in the cables. One can notice that at this collision

energy, the FDDVertex selection cleans the data tremendously with only eight clear peaks with no entries in any other BCs.

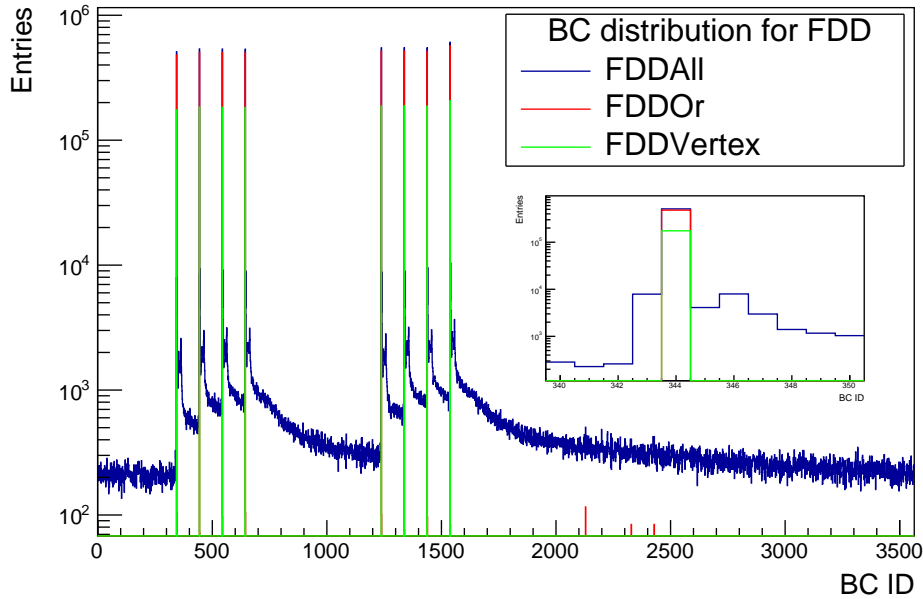


Figure 6.5: Bunch crossing (BC) distribution for FDD during run 534265 with a close-up on the first collision of the orbit. The selection FDDAll refers to any registered event, FDDOr refers to events registered within a certain time window, and finally, events registered in the time window by both sides of the detector in the same BC contribute to FDDVertex.

Distributions for a single FDD channel

Fig. 6.6 shows the BC distribution for only one of the FDD channels: the PMT 0, which is a PMT connected to the pad located in the first layer of the C side. The plot shows four different distributions depending on the event selection: all, inGate bit, inTime and layer coincidence. The first one, all, refers to any registered event by this channel regardless of the information about the charge. The inGate bit refers to events, which were registered in the 5 ns (± 192 TDC, 1 TDC= 13 ps) integration window. The inTime bit accounts for events in restricted time interval of ± 2 ns (total time interval of 4 ns corresponding to ± 153 TDC) around the main peak. The layer coincidence shows only events, where the signal was registered in both layers of the same quadrant, providing the opportunity to extremely clean the data from background effects.

Fig. 6.7 and Fig. 6.8 show the charge and time distributions of the PMT 0. The four distributions in each plot include the same event selections as described above: all, inGate bit, inTime and layer coincidence. Once again it can be seen, that with the use of the layer coincidence, the data from the FDD can be extremely cleaned of the background effects.

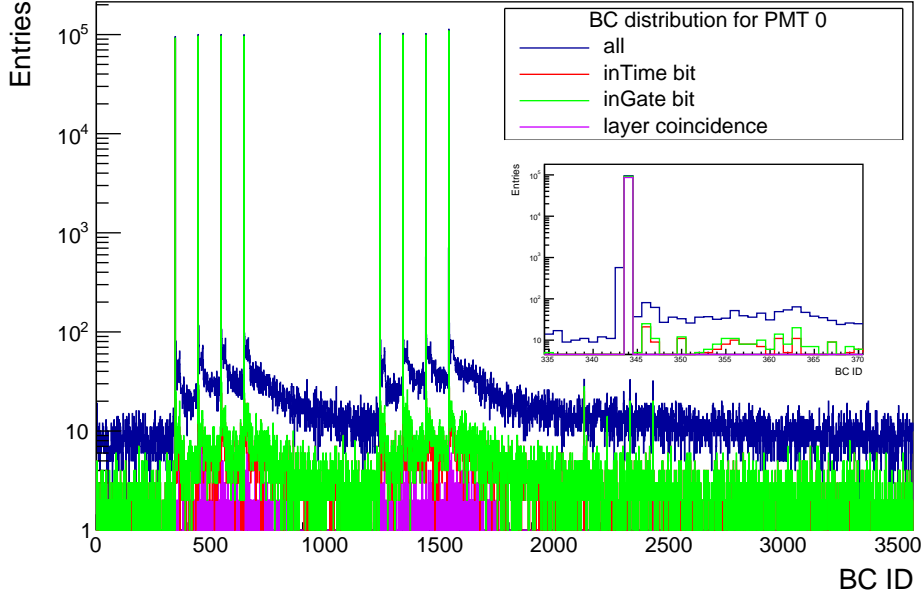


Figure 6.6: Bunch crossing (BC) distribution for a single FDD channel during run 534265 with a close-up on the first collision of the orbit. The selections are: all, inGate bit, inTime and layer coincidence. All refers to any registered event by this channel, the inGate bit refers to events registered in the integration time window, the inTime bit accounts for events with restricted time interval of 4 ns around the main peak, and the layer coincidence shows events, where the signal was registered in both layers of the same quadrant.

Charge and time distribution for individual BC

Another set of plots of charge and time is shown in Fig. 6.9 and Fig. 6.10. These plots show the charge and time distributions for each of the BC individually in a 3D histogram for a single channel. This provides an opportunity to study the distributions in each of the BC separately, e.g. to see whether there is an influence of a saturated signal in one BC on the next few BCs. The distributions were produced with no condition on the signal, which corresponds to the 'all' selection discussed previously.

6.2.3 Vertex position

The presence of FDD on both sides of the IP makes it possible to estimate the collision time and reconstruction of the primary vertex. The FDD vertex position vs FDD collision time correlation in a stable-beam pp run 526689 at 13.6 TeV from 2022 is shown in Fig. 6.11. Fig. 6.12 shows the coordinates of the vertex along the beamline (z) for different stable-beam pp runs at 13.6 TeV from 2022, where one can observe small shifts in the vertex position. This shift was consistently observed by other detectors of ALICE, e.g. the FT0.

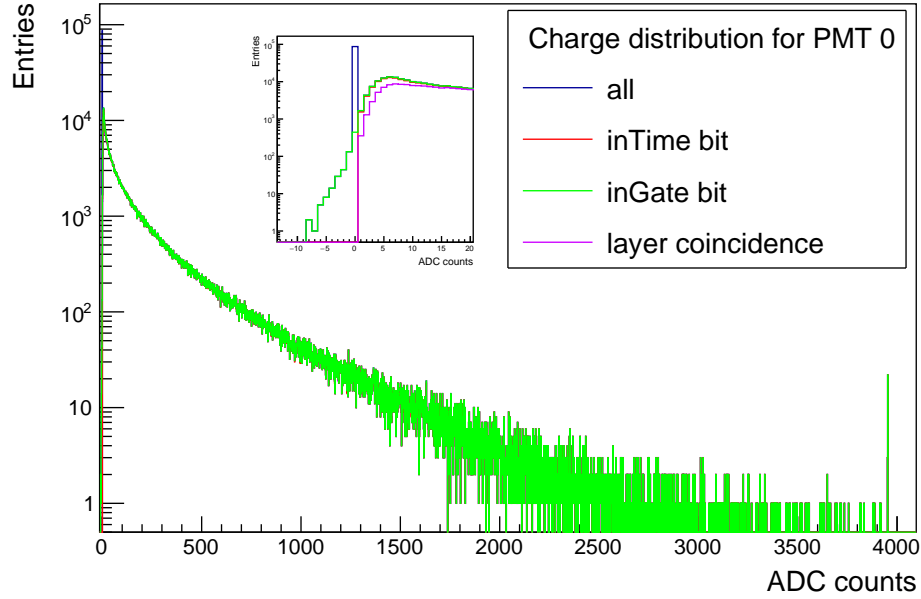


Figure 6.7: Charge distribution for a single FDD channel during run 534265. The selections are: all, inGate bit, inTime and layer coincidence. All refers to any registered event by this channel, the inGate bit refers to events registered in the integration time window, the inTime bit accounts for events with restricted time interval of 4 ns around the main peak, and the layer coincidence shows events, where the signal was registered in both layers of the same quadrant.

6.3 Summary and outlook

Since the beginning of Run 3 in summer 2022, FDD has been successfully integrated with the ALICE systems and it is taking part in the data-taking together with the other detectors. The FDD was already configured for pp collisions and shows good performance. However, the understanding of the detector is still work in progress and the final configuration for pp and Pb-Pb collisions is yet to be set.

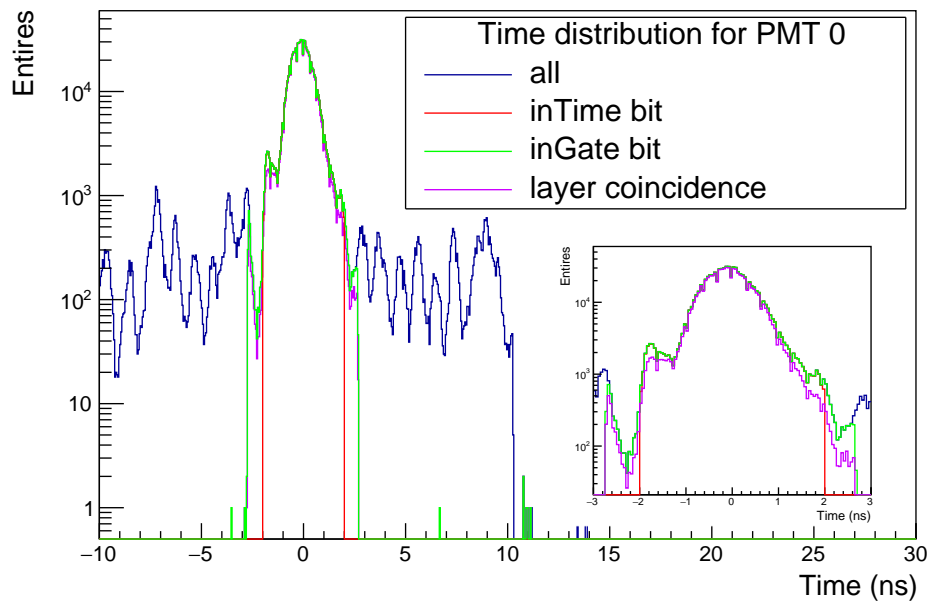


Figure 6.8: Time distribution for a single FDD channel during run 534265. The selections are: all, inGate bit, inTime and layer coincidence. All refers to any registered event by this channel, the inGate bit refers to events registered in the integration time window, the inTime bit accounts for events with restricted time interval of 4 ns around the main peak, and the layer coincidence shows events, where the signal was registered in both layers of the same quadrant.

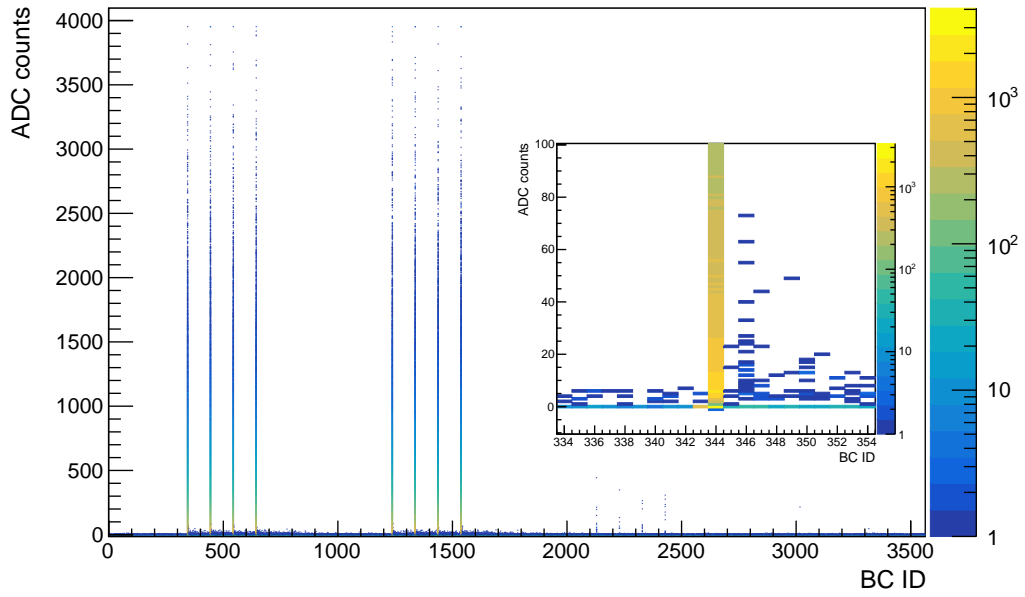


Figure 6.9: 3D histogram of the charge distribution for all BCs for a single FDD channel during run 534265. The distribution was produced with no selection condition on the signal, hence taking into account all events registered by the channel.

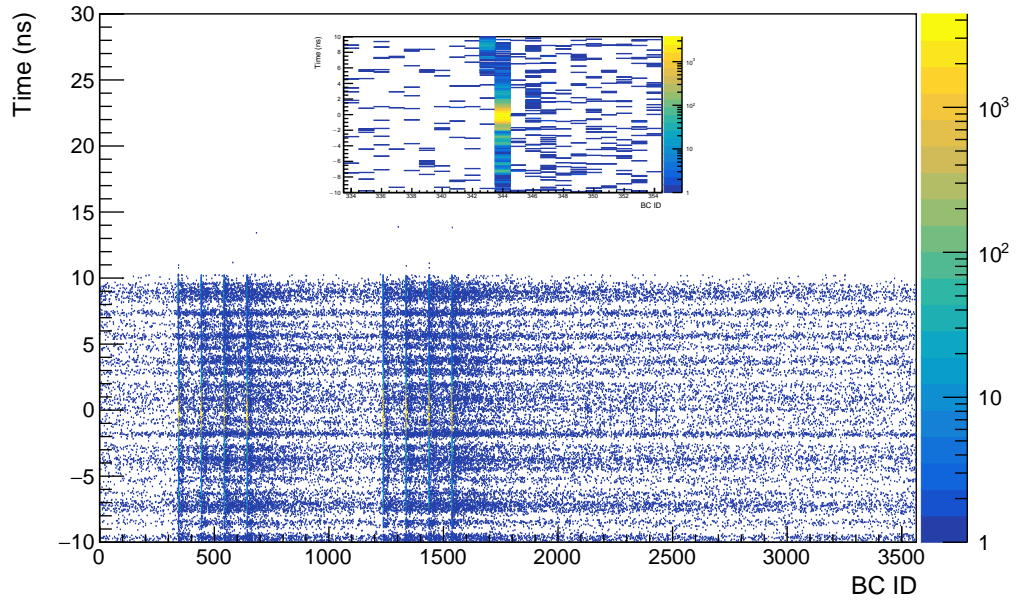
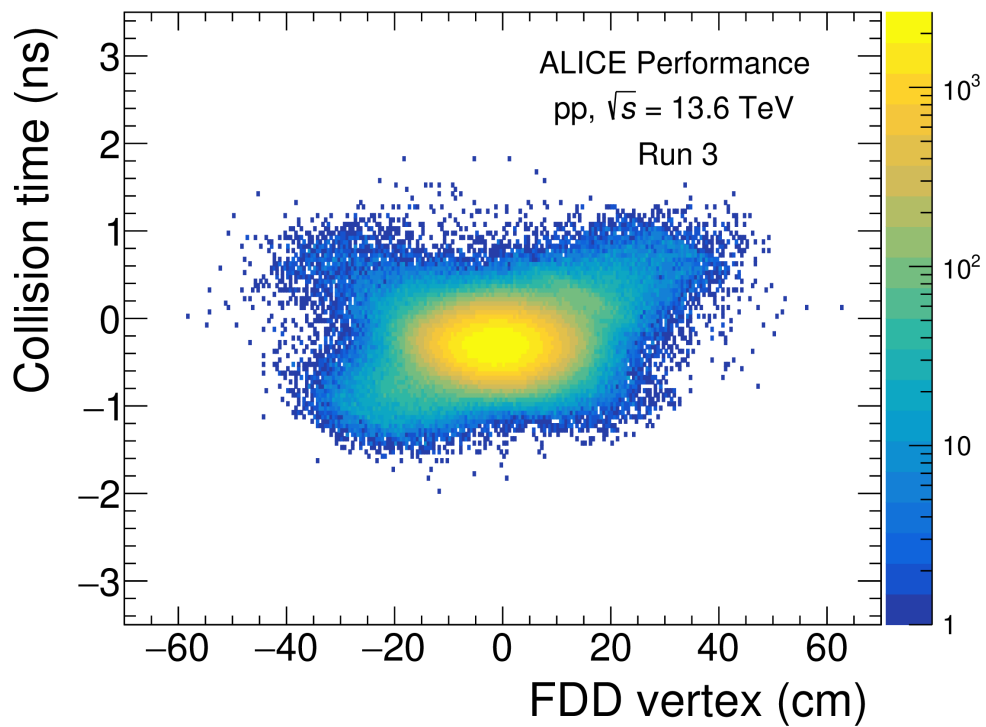


Figure 6.10: 3D histogram of the time distribution for all BCs for a single FDD channel during run 534265. The distribution was produced with no selection condition on the signal, hence taking into account all events registered by the channel.



ALI-PERF-534063

Figure 6.11: FDD vertex vs FDD collision time correlation in stable-beam pp collisions at 13.6 TeV. Data from run 526689 (2022) using a filling scheme consisting of 12 single pp bunches, out of which 8 collided in ALICE. Courtesy of A. Khuntia.

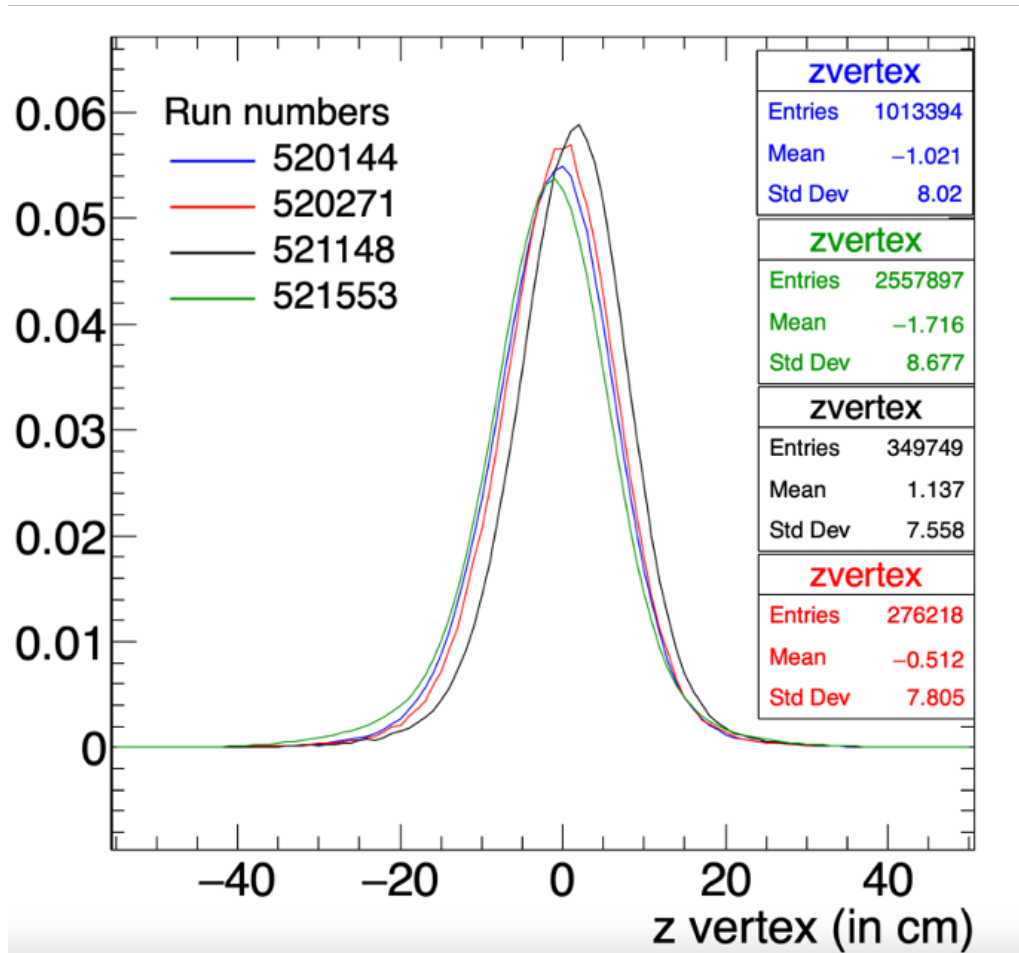


Figure 6.12: FDD z vertex position for different stable-beam pp runs at 13.6 TeV from 2022. One can notice a small shift in the position for each run, consistently observed with other ALICE detectors. Courtesy of A. Khuntia.

Summary and outlook

This thesis covered the studies of the performance of scintillator detectors for particle detection. The studies were done with the Forward Diffractive Detector (FDD), which was added to the ALICE apparatus at the CERN LHC during the upgrade for Runs 3 and 4, and also with custom-made scintillators containing inorganic CsPbBr₃ nanocrystals embedded in organic polystyrene and silicone matrices. These nanocomposites were prepared in order to study their properties and performance as they are one of the scintillator prospects for future high-energy physics experiments, which demand improvements on the detector time response, cost and radiation hardness due to the increase of collision energies and interaction rates.

During the production of the custom-made samples, different techniques and methods to produce the nanocomposites with inorganic nanocrystals embedded in organic matrices were tested and evaluated. In order to study the performance of the samples, a test bench using cosmic-ray muons was set up.

Summarising the custom-made scintillator characterisation, it was observed, that there is a very clear experimental signal of cosmic-ray muons measured with the pure silicone matrix distinguishable from the PMT background. The signal remains clear and the effective rate of muons per hour stays similar after the addition of a commercial scintillator (PPO) into the silicone matrix. However, when the CsPbBr₃ nanocrystals (QD) are added to the matrix, the detection efficiency of cosmic-ray muons is reduced, even with PPO present in the sample. This is a sign of the high self-absorption of the QD.

For the pure polystyrene matrix, one can observe a peak in very low charges, which probably arises from cosmic-ray muons. To confirm this, further investigation, such as measurements at different supply voltages or addition of the PPO to the polystyrene base, is needed. When QD are added to the polystyrene matrix, there is only a weak enhancement of the signal over the background. The measurements show an increasing trend of the detected signal with the increase of the QD concentration in the sample. However, this holds only for the samples with QD concentrations of 0.1 %, 0.2 %, and 0.3 %. The samples with lower QD concentrations show higher ratio of the signal with respect to the background, but their production included the use of 3 and 3 drops of the catalysts RP-128 and MEKP, respectively, compared to the use of 2 and 2 drops of RP-128 and MEKP for all other polystyrene samples. This influences the polymerisation process of the nanocomposites, which can lead to better optical properties providing better signal.

There are many things to be learned from the scintillator characterisation, which

can be used for better understanding of the sample performance and in consequence improving their production. It was observed, that the addition of the QD into the composites makes the scintillators less efficient. This is most probably an effect of the high self-absorption of the nanocrystals. In order to address this, one of the possibilities is to find a suitable wavelength-shifting scintillator and add it to the composite. This would result in less self-absorption, making the detection of cosmic-ray muons efficient. Another possibility is to add optical fibres to the samples, which would transfer the created scintillation photons to the photodetector before their absorption. Additionally, it is foreseen to design and use a modified test bench, which uses laser pulses to irradiate the samples. This would speed up the studies and provide the possibility to easily obtain measurements with enough statistics.

Some aspects of current performance of FDD in pp stable-beam collisions from April 2023 were presented. Several plots including the bunch crossing, time and charge distributions were shown together with background rejection possibilities that the FEE and the detector geometry allows us to do. An example of the measurement of the vertex position was given for pp runs at 13.6 TeV from 2022 data. To conclude, the detector is taking data already for several months and our understanding of its performance is increasing with time. The final operational parameters for the pp and Pb-Pb data-taking periods will be fine-tuned in the following months using similar techniques as those presented here.

Bibliography

- [1] *The Large Hadron Collider*. <https://home.cern/science/accelerators/large-hadron-collider>. Accessed: 2021-08-07.
- [2] The ALICE Collaboration et al. “The ALICE experiment at the CERN LHC”. In: *Journal of Instrumentation* 3.08 (Oct. 2008), S08002–S08002. DOI: 10.1088/1748-0221/3/08/s08002. URL: <https://doi.org/10.1088/1748-0221/3/08/s08002>.
- [3] W. H. Trzaska. “New ALICE detectors for Run 3 and 4 at the CERN LHC”. In: *Nuclear Instruments and Methods in Physics Research Section A: Accelerators, Spectrometers, Detectors and Associated Equipment* 958 (2020). Proceedings of the Vienna Conference on Instrumentation 2019, p. 162116. ISSN: 0168-9002. DOI: <https://doi.org/10.1016/j.nima.2019.04.070>. URL: <https://www.sciencedirect.com/science/article/pii/S0168900219305443>.
- [4] Y. A. Melikyan et al. “Characteristic properties of Planacon MCP-PMTs”. In: *Journal of Instrumentation* 16.12 (Dec. 2021), P12032. DOI: 10.1088/1748-0221/16/12/P12032. URL: <https://dx.doi.org/10.1088/1748-0221/16/12/P12032>.
- [5] Y. A. Melikyan. “Performance of Planacon MCP-PMT photosensors under extreme working conditions”. In: *Nuclear Instruments and Methods in Physics Research Section A: Accelerators, Spectrometers, Detectors and Associated Equipment* 952 (2020). 10th International Workshop on Ring Imaging Cherenkov Detectors (RICH 2018), p. 161689. ISSN: 0168-9002. DOI: <https://doi.org/10.1016/j.nima.2018.12.004>. URL: <https://www.sciencedirect.com/science/article/pii/S0168900218318023>.
- [6] Y. A. Melikyan et al. “Performance of the cost-effective Planacon® MCP-PMTs in strong magnetic fields”. In: *Nuclear Instruments and Methods in Physics Research Section A: Accelerators, Spectrometers, Detectors and Associated Equipment* 983 (2020), p. 164591. ISSN: 0168-9002. DOI: <https://doi.org/10.1016/j.nima.2020.164591>. URL: <https://www.sciencedirect.com/science/article/pii/S0168900220309888>.
- [7] M. Slupecki. “Fast Interaction Trigger for ALICE upgrade”. In: *Nuclear Instruments and Methods in Physics Research Section A: Accelerators, Spectrometers, Detectors and Associated Equipment* 1039 (2022), p. 167021. ISSN: 0168-9002. DOI: <https://doi.org/10.1016/j.nima.2022.167021>. URL: <https://www.sciencedirect.com/science/article/pii/S0168900222004466>.

- [8] V. Zabloudil et al. “Detektor pro CERN”. In: *Pražská technika* (2021). ISSN: 1213-5348.
- [9] M. Broz et al. “Performance of ALICE AD modules in the CERN PS test beam”. In: *Journal of Instrumentation* 16.01 (Jan. 2021), P01017–P01017. DOI: 10.1088/1748-0221/16/01/p01017. URL: <https://doi.org/10.1088/1748-0221/16/01/p01017>.
- [10] J. M. Mejía et al. “Forward Diffractive Detector control system for Run 3 in the ALICE experiment”. In: *Nuclear Instruments and Methods in Physics Research Section A: Accelerators, Spectrometers, Detectors and Associated Equipment* 1050 (2023), p. 168146. ISSN: 0168-9002. DOI: <https://doi.org/10.1016/j.nima.2023.168146>. URL: <https://www.sciencedirect.com/science/article/pii/S0168900223001365>.
- [11] V. Zabloudil. *Construction and commissioning of the FDD detector*. 2021.
- [12] J. Contreras et al. “Ultra-peripheral heavy-ion collisions at the LHC”. In: *International Journal of Modern Physics A* 30 (Mar. 2015), p. 1542012. DOI: 10.1142/S0217751X15420129.
- [13] M. Slupecki. “The Fast Interaction Trigger for the ALICE Upgrade”. Presented 12 Jun 2020. PhD thesis. June 2020. URL: <https://cds.cern.ch/record/2741462>.
- [14] D. A. Finogeev. “Fully integrated digital readout for the new Fast Interaction Trigger for the ALICE upgrade”. In: *Nuclear Instruments and Methods in Physics Research Section A: Accelerators, Spectrometers, Detectors and Associated Equipment* 952 (2020). 10th International Workshop on Ring Imaging Cherenkov Detectors (RICH 2018), p. 161920. ISSN: 0168-9002. DOI: <https://doi.org/10.1016/j.nima.2019.02.047>. URL: <https://www.sciencedirect.com/science/article/pii/S0168900219302359>.
- [15] *BC-418, BC-420, BC-422 Premium Plastic Scintillators*. <https://www.crystals.saint-gobain.com/sites/imdf.crystals.com/files/documents/bc418-420-422-data-sheet.pdf>. Accessed: 2021-05-05.
- [16] S. A. Ponomarenko et al. “Nanostructured organosilicon luminophores and their application in highly efficient plastic scintillators”. In: *Scientific Reports* 4 (2014).
- [17] *Nanostructured organosilicon luminophores (NOLs)*. <https://www.luminnotech.com/products/luminophores>. Accessed: 2021-05-05.
- [18] *Photomultiplier tube assembly H8409-70*. <https://www.hamamatsu.com/eu/en/product/type/H8409-70/index.html>. Accessed: 2021-10-06.
- [19] C. Dujardin. “Matériaux scintillateurs inorganiques”. In: *Techniques de l’ingénieur Optique Photonique* base documentaire : TIP520WEB.ref. article : e6347 (2017). fre. DOI: 10.51257/a-v1-e6347. eprint: basedocumentaire:TIP520WEB.. URL: <https://www.techniques-ingenieur.fr/base-documentaire/electronique-photonique-th13/materiaux-pour-l-optique-et-les-lasers-42450210/materiaux-scintillateurs-inorganiques-e6347/>.

- [20] *Biograph Vision*. <https://www.siemens-healthineers.com/molecular-imaging/pet-ct/biograph-vision>. Accessed: 2023-03-01.
- [21] P. Lecoq. “Pushing the Limits in Time-of-Flight PET Imaging”. In: *IEEE Transactions on Radiation and Plasma Medical Sciences* 1.6 (2017), pp. 473–485. DOI: 10.1109/TRPMS.2017.2756674.
- [22] C. Dujardin et al. “Needs, Trends, and Advances in Inorganic Scintillators”. In: *IEEE Transactions on Nuclear Science* 65.8 (2018), pp. 1977–1997. DOI: 10.1109/TNS.2018.2840160.
- [23] C. Grupen et al. *Particle Detectors*. 2nd ed. Cambridge Monographs on Particle Physics, Nuclear Physics and Cosmology. Cambridge University Press, 2008. DOI: 10.1017/CB09780511534966.
- [24] H. Kolanoski et al. *Particle Detectors: Fundamentals and Applications*. Oxford University Press, 2020. ISBN: 9780198858362. URL: <https://oxford.universitypressscholarship.com/view/10.1093/oso/9780198858362.001.0001/oso-9780198858362>.
- [25] S. N. Ahmed. In: *Physics and Engineering of Radiation Detection (Second Edition)*. Elsevier, 2015. ISBN: 978-0-12-801363-2. DOI: <https://doi.org/10.1016/B978-0-12-801363-2.00006-1>. URL: <https://www.sciencedirect.com/science/article/pii/B9780128013632000061>.
- [26] G. F. Knoll. *Radiation Detection and Measurement, third edition*. New York: John Wiley and Sons, 2000. ISBN: 978-0-471-07338-3.
- [27] G. Lutz. *Semiconductor Radiation Detectors*. Springer Berlin, Heidelberg, 2007. ISBN: 978-3-540-71679-2. DOI: <https://doi.org/10.1007/978-3-540-71679-2>. URL: <https://link.springer.com/book/10.1007/978-3-540-71679-2>.
- [28] C. Henry. “Size Effects on Structure and Morphology of Free or Supported Nanoparticles”. In: *Nanomaterials and Nanochemistry*. Berlin, Heidelberg: Springer Berlin Heidelberg, 2007, pp. 3–34. ISBN: 978-3-540-72993-8. DOI: 10.1007/978-3-540-72993-8_1. URL: https://doi.org/10.1007/978-3-540-72993-8_1.
- [29] E. Roduner. “Size matters: why nanomaterials are different”. In: *Chem. Soc. Rev.* 35 (7 2006), pp. 583–592. DOI: 10.1039/B502142C. URL: <http://dx.doi.org/10.1039/B502142C>.
- [30] R. Gopal et al. “Quantum Confinement Effect of 2D Nanomaterials”. In: Aug. 2020. ISBN: 978-1-83880-918-8. DOI: 10.5772/intechopen.90140.
- [31] A. Dey et al. “State of the Art and Prospects for Halide Perovskite Nanocrystals”. In: *ACS Nano* 15.7 (July 2021). Accessed: 2023-03-17., pp. 10775–10981. ISSN: 1936-0851. DOI: 10.1021/acsnano.0c08903. URL: <https://doi.org/10.1021/acsnano.0c08903>.
- [32] T. Dai et al. “Strategies for High-Performance Large-Area Perovskite Solar Cells toward Commercialization”. In: *Crystals* 11 (Mar. 2021), p. 295. DOI: 10.3390/cryst11030295.

- [33] L. Protesescu et al. “Nanocrystals of Cesium Lead Halide Perovskites (CsPbX₃, X = Cl, Br, and I): Novel Optoelectronic Materials Showing Bright Emission with Wide Color Gamut”. In: *Nano Letters* 15.6 (June 2015), pp. 3692–3696. ISSN: 1530-6984. DOI: 10.1021/nl5048779. URL: <https://doi.org/10.1021/nl5048779>.
- [34] G. Kickelbick. “Introduction to Hybrid Materials”. In: *Hybrid Materials*. John Wiley & Sons, Ltd, 2006. ISBN: 9783527610495. DOI: <https://doi.org/10.1002/9783527610495.ch1>. eprint: <https://onlinelibrary.wiley.com/doi/pdf/10.1002/9783527610495.ch1>. URL: <https://onlinelibrary.wiley.com/doi/abs/10.1002/9783527610495.ch1>.
- [35] G. Odian. “Principles of Polymerization”. In: John Wiley & Sons, Ltd, 2004. ISBN: 9780471478751. DOI: <https://doi.org/10.1002/047147875X.ch1>. URL: <https://onlinelibrary.wiley.com/doi/abs/10.1002/047147875X.ch1>.
- [36] N. Dinu et al. “Studies of MPPC detectors down to cryogenic temperatures”. In: *Nuclear Instruments and Methods in Physics Research Section A: Accelerators, Spectrometers, Detectors and Associated Equipment* 787 (2015). New Developments in Photodetection NDIP14. ISSN: 0168-9002. DOI: <https://doi.org/10.1016/j.nima.2014.12.061>. URL: <https://www.sciencedirect.com/science/article/pii/S0168900214015174>.
- [37] J. Král. *Synthesis and characterisation of scintillating nanocomposites based on CsPbBr₃ nanocrystals*. <https://dspace.cvut.cz/handle/10467/105397>. Accessed: 2023-03-17. 2022.
- [38] *G Force Calculator — RCF to RPM*. <https://www.sigmaaldrich.com/CZ/en/support/calculators-and-apps/g-force-calculator>. Accessed: 2023-04-21.
- [39] K. Děcká et al. “On the Role of Cs₄PbBr₆ Phase in the Luminescence Performance of Bright CsPbBr₃ Nanocrystals”. In: *Nanomaterials* 11.8 (2021). ISSN: 2079-4991. DOI: 10.3390/nano11081935. URL: <https://www.mdpi.com/2079-4991/11/8/1935>.
- [40] K. Děcká et al. “Scintillation Response Enhancement in Nanocrystalline Lead Halide Perovskite Thin Films on Scintillating Wafers”. In: *Nanomaterials* 12.1 (2022). ISSN: 2079-4991. DOI: 10.3390/nano12010014. URL: <https://www.mdpi.com/2079-4991/12/1/14>.
- [41] J. Maes et al. “Light Absorption Coefficient of CsPbBr₃ Perovskite Nanocrystals”. In: *The Journal of Physical Chemistry Letters* 9.11 (June 2018), pp. 3093–3097. DOI: 10.1021/acs.jpcllett.8b01065. URL: <https://doi.org/10.1021/acs.jpcllett.8b01065>.
- [42] *REICHHOLD® PROMOTOR RP-128*. <https://www.reichhold.com/en/composites-product-detail.aspx?pid=1244>. Accessed: 2023-04-09.
- [43] *SILASTIC™ MS-4002 Moldable Silicone A&B Kit*. <https://www.dow.com/en-us/pdp/silastic-ms-4002-moldable-silicone-ab-kit.04125048z.html>. Accessed: 2023-03-16.

- [44] *CAEN VME8010: 7U 21 Slot VME64 Low Cost Crate*. <https://www.caen.it/products/vme8010/>. Accessed: 2023-04-14.
- [45] *CAEN V814: 16 Channel Low Threshold Discriminator*. <https://www.caen.it/products/v814/>. Accessed: 2023-04-14.
- [46] *CAEN N840: 8 Channel Leading Edge Discriminator*. <https://www.caen.it/products/n840/>. Accessed: 2023-04-15.
- [47] *CAEN V1742: 32+2 Channel 12bit 5 GS/s Switched Capacitor Digitizer*. <https://www.caen.it/products/v1742/>. Accessed: 2023-04-14.
- [48] *CAEN V1718: VME-USB2.0 Bridge*. <https://www.caen.it/products/v1718/>. Accessed: 2023-04-14.
- [49] *CAEN V925: Quad Linear FAN-IN FAN-OUT*. <https://www.caen.it/products/v925/>. Accessed: 2023-04-14.
- [50] *ORTEC: 556 and 556H High Voltage Power Supply*. <https://www.ortec-online.com/products/electronics/power-supplies-and-nuclear-instrument-module-nim-bins/556-and-556h>. Accessed: 2023-04-15.
- [51] R. Brun et al. "ROOT: An object oriented data analysis framework". In: *Nucl. Instrum. Meth. A* 389 (1997). Ed. by M. Werlen and D. Perret-Gallix, pp. 81–86. DOI: 10.1016/S0168-9002(97)00048-X.

Appendix A

Test bench: crosstalk test

In order to reject the background from the measurements with the test bench, a crosstalk test was performed, which explored whether a very high signal in one of the trigger PMTs could induce a signal in one of the other PMTs. The crosstalk test was performed with a set-up shown in Fig. A.1. The signal in the top trigger PMT was generated by a laser with a tunable attenuator, which was continuously altered during the measurement. In this way, the signal detected by the PMT ranged within no signal at all and total saturation. The remaining PMTs were fed by high voltages of 2000 V.

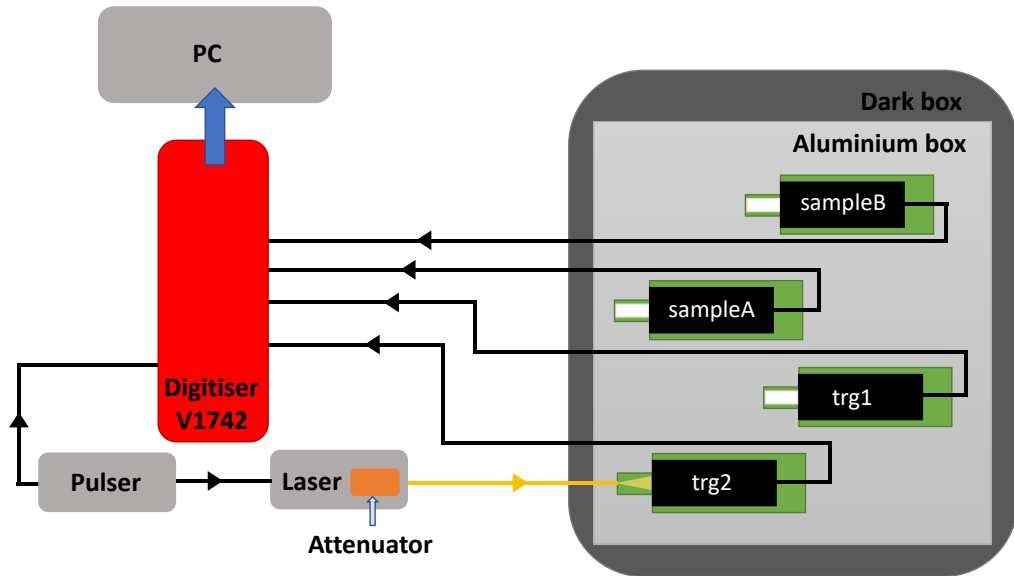


Figure A.1: Set-up used for the electrical crosstalk test for measurements with cosmic-ray muons at the test bench.

The resulting amplitude distributions for PMTs corresponding to sampleA and sampleB are shown in Fig. A.2 and Fig. A.3, respectively. As one can see, the distribution for laser off contains a single Gaussian peak that corresponds to the noise level. However, if the laser is switched on, the original distribution distorts its shape

slightly and another peak at ≈ 6 mV appears. This corresponds to a noise introduced by the electrical crosstalk.

One can also have a look at the correlation of the irradiated trigger amplitude with the amplitude of the other channels. As can be seen from Fig. A.4, Fig. A.5 and Fig. A.6, there is no correlation observed whatsoever. For the trg1 channel, the distribution is slightly more noisy compared to the sample channels. This is a consequence of the sample present in the 3D-printed module.

To conclude, a safe threshold of minimal signal amplitude of 8 mV for each of the channels can be adopted to exclude the crosstalk events.

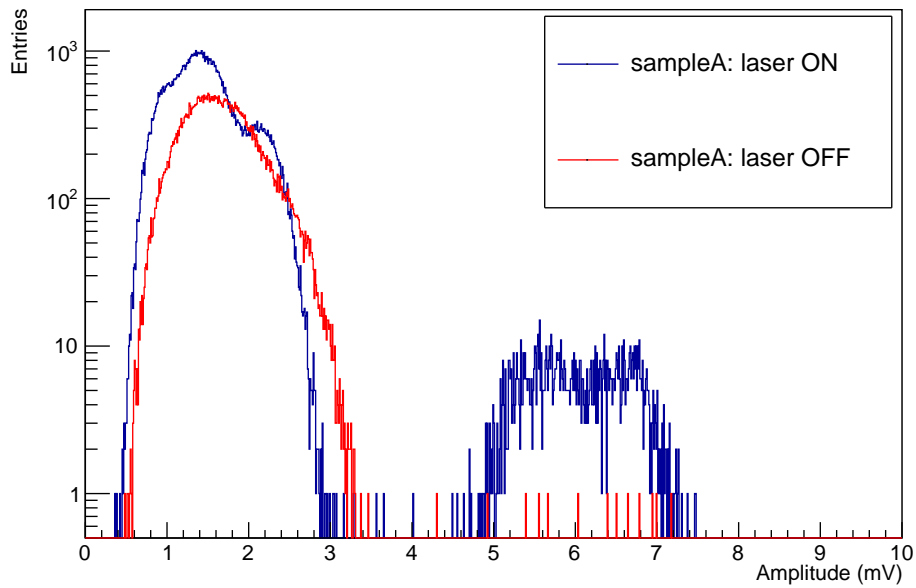


Figure A.2: Amplitude distribution for sampleA during the crosstalk test. Red line corresponds to the distribution measured with the laser not irradiating the trg2 channel (laser OFF), blue line shows the distribution with the laser irradiating the trg2 channel (laser ON).

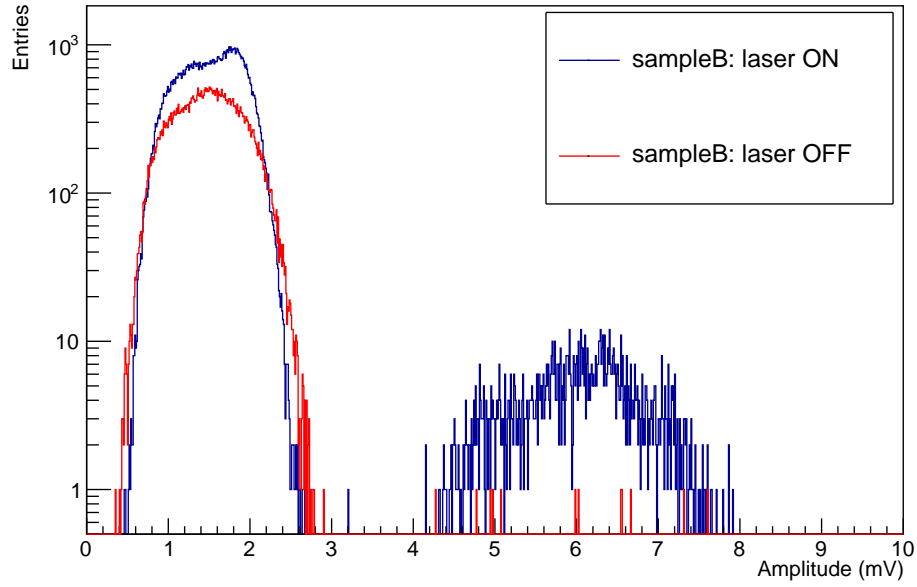


Figure A.3: Amplitude distribution for sampleB during the crosstalk test. Red line corresponds to the distribution measured with the laser not irradiating the trg2 channel (laser OFF), blue line shows the distribution with the laser irradiating the trg2 channel (laser ON).

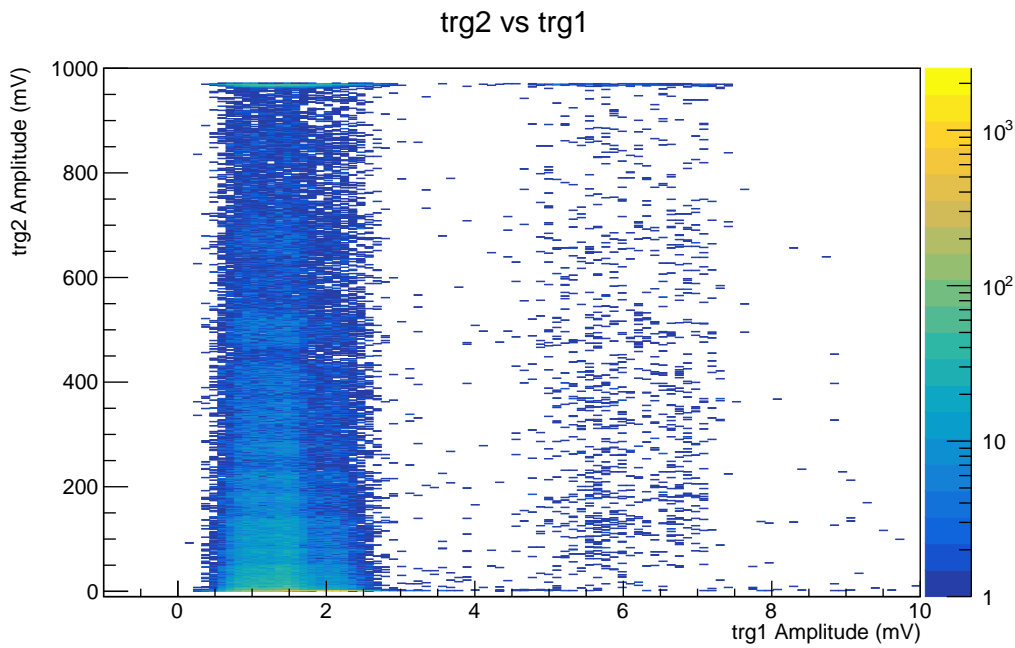


Figure A.4: Amplitude correlation of trg2 vs trg1 channels during the crosstalk test.

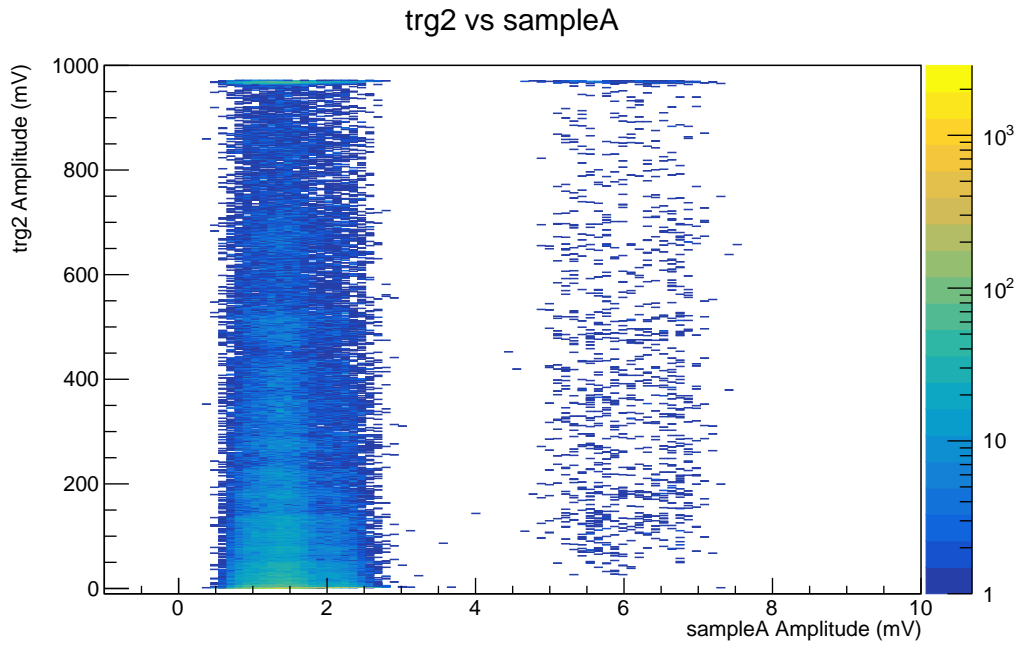


Figure A.5: Amplitude correlation of trg2 vs sampleA channels during the crosstalk test.

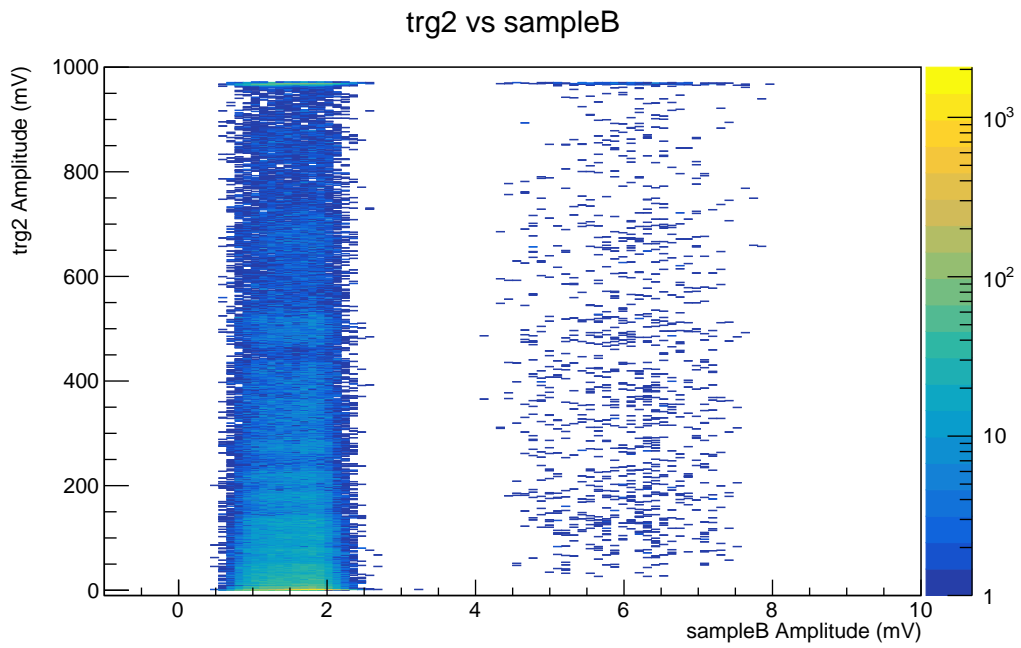


Figure A.6: Amplitude correlation of trg2 vs sampleB channels during the crosstalk test.

Appendix B

Custom-made scintillator characterisation: polystyrene matrix

Table B.1 contains the full data of the characterisation of the silicone matrix samples. For the measurement of the silicone samples, the module sampleA with the PMT DA1417 was used. The supply voltage of the PMT was either 1800 V or 2000 V as denoted in the table. Depending on the supply voltage, a different set of parameters was used for the data analysis, such as the background run, the binning, and the charge window used for the integration of the events relevant for the effective rate calculation.

For runs at 1800 V, the used background run that was subtracted from the data was the run 0328. The charge interval for the analysis was chosen as $[-99.5, 200.5]$ with 300 bins. In order to count the number of entries and subsequently the effective rate, a charge window of $[-53, 200]$ was used. To show the resulting signal spectra after the background subtraction, the distributions were rebinned with $N_{rebin} = 5$.

Regarding the measurements at supply voltages of 2000 V, the used background run was 0322. The charge interval for the analysis was increased to $[-99.5, 300.5]$ with 400 bins. As the pedestal charge measured by the PMTs at higher voltages is wider, the charge window for integration was shifted to $[-42, 300]$. The rebinning constant stayed the same as for 1800 V, i.e. $N_{rebin} = 5$.

For the samples with the polystyrene matrix (PS), the following samples have been chosen for analysis:

- NO QD 14.7.
- QD 0.05 % 3&3 drops 13.7.
- QD 0.1 % 7.7.
- QD 0.2 % 4.7.
- QD 0.3 % 4.7.

Characterised sample	HV	run ID	$R_{\text{eff,S+B}}$ (1/h)	$R_{\text{eff,B}}$ (1/h)	R_{SB}
NO QD 3&3 dr. 14.7.	2200	0419	9.5 ± 0.6	7.7 ± 0.6	1.23 ± 0.12
QD 0.05 % 3&3 dr. 13.7.	2200	0331	9.0 ± 0.4	7.7 ± 0.6	1.17 ± 0.10
QD 0.1 % 7.7.	2200	0420	8.7 ± 0.6	7.7 ± 0.6	1.12 ± 0.11
QD 0.2 % 4.7.	2200	0413	9.0 ± 0.3	7.7 ± 0.6	1.16 ± 0.09
QD 0.3 % 4.7.	2200	0417	9.2 ± 0.5	7.7 ± 0.6	1.19 ± 0.11

Table B.1: Characterisation results of the polystyrene matrix samples, where the characterised sample is described, HV denotes the supply voltage (module sampleA), run ID marks the identification of the run with the sample, $R_{\text{eff,S+B}}$ denotes the effective rate of muons per hour for measurement with the sample, $R_{\text{eff,B}}$ denotes the effective rate of muons per hour for the background measurement with the PMT only, and R_{SB} is the ratio of the signal to background effective rates. The note '3&3 drops' stands for use of 3 and 3 drops of the catalysts RP-128 and MEKP, respectively, compared to the use of 2 and 2 drops of RP-128 and MEKP for all other polystyrene samples.

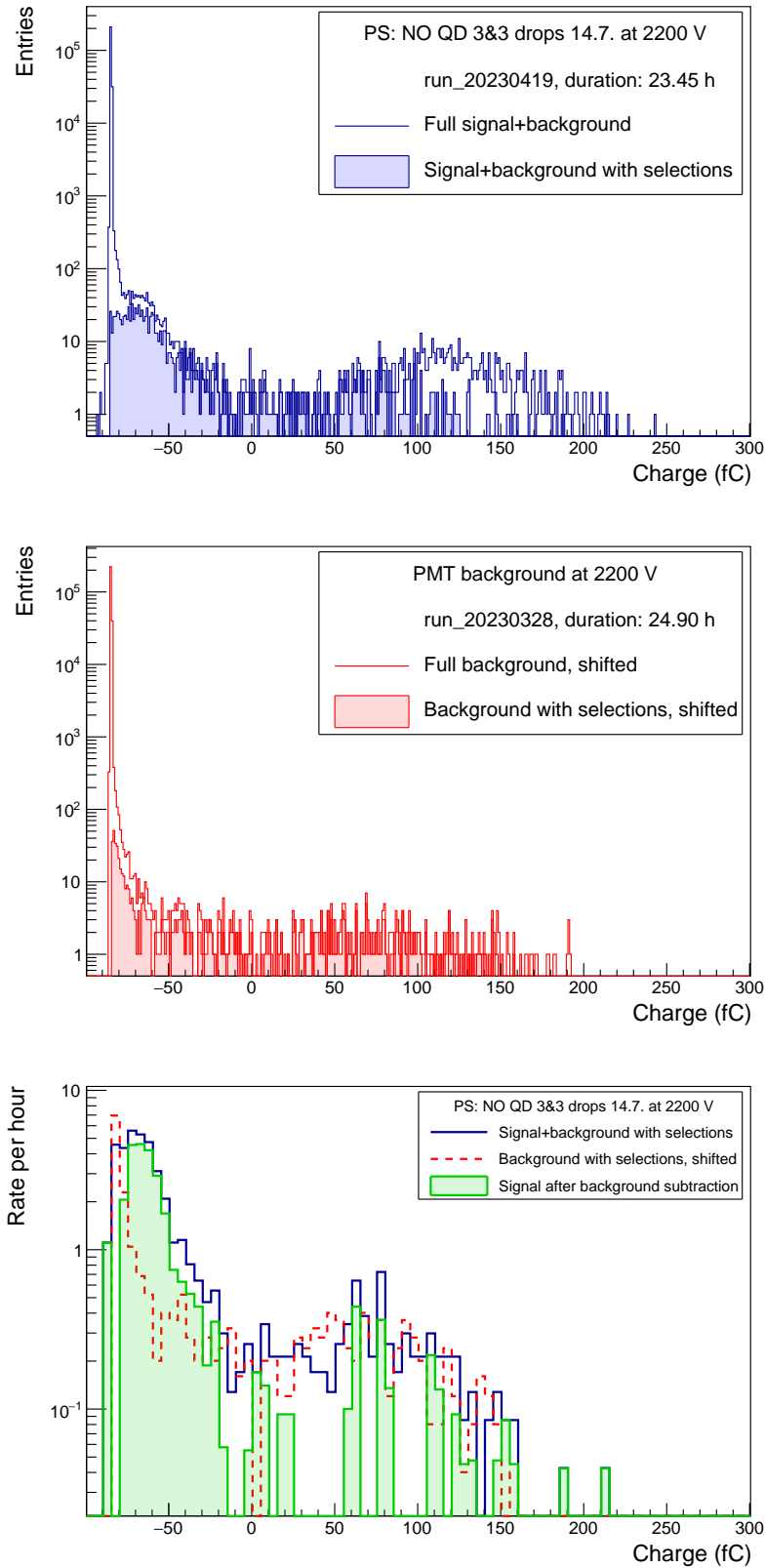


Figure B.1: Charge distribution for the NO QD 3&3 drops 14.7. sample at 2200 V: signal+background (top), PMT background only (middle), charge distribution of the signal after PMT background subtraction (bottom). The note '3&3 drops' stands for use of 3 and 3 drops of the catalysts RP-128 and MEKP, respectively, compared to the use of 2 and 2 drops of RP-128 and MEKP for all other polystyrene samples.

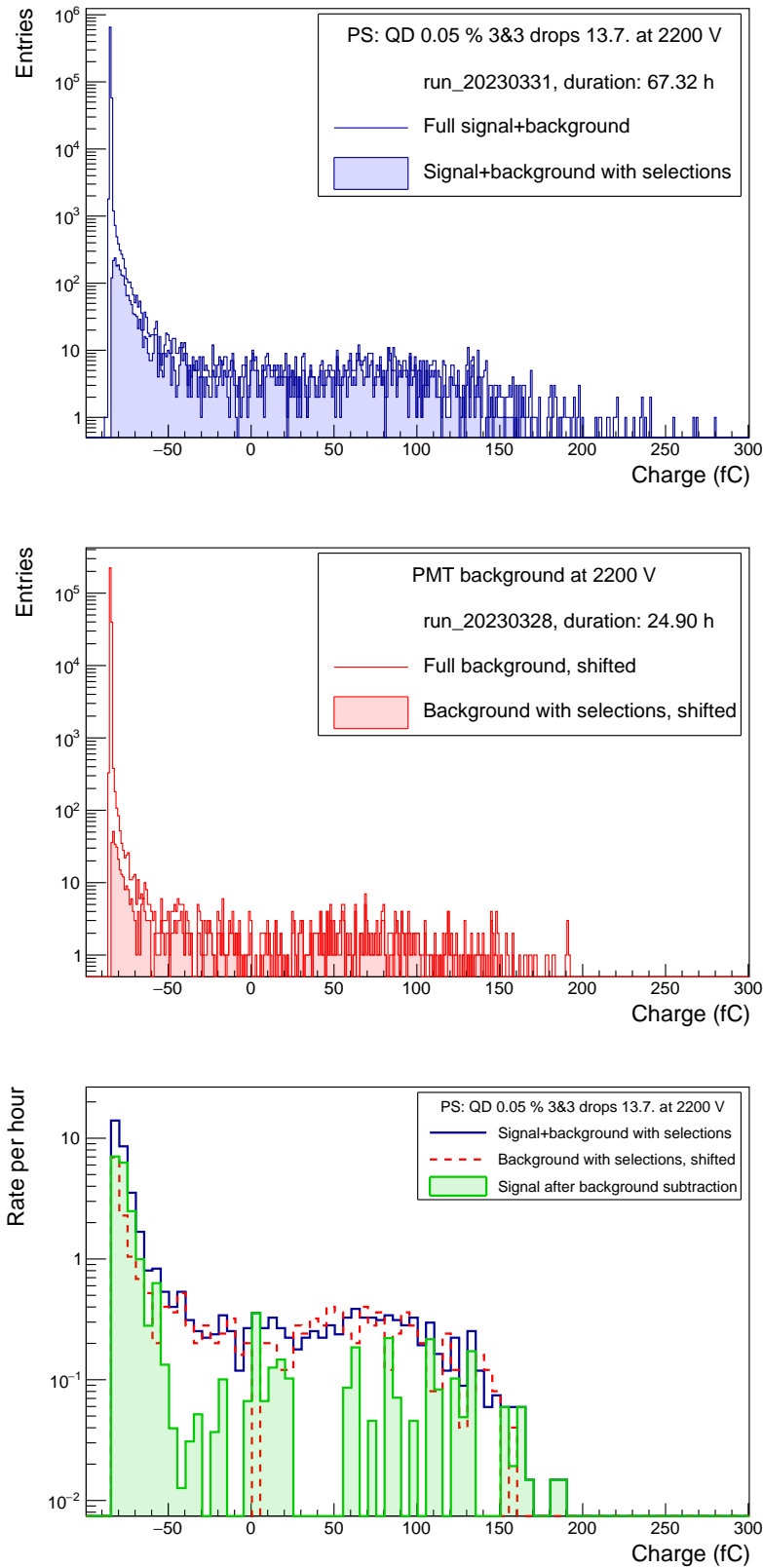


Figure B.2: Charge distribution for the QD 0.05 % 3&3 drops 13.7. sample at 2200 V: signal+background (top), PMT background only (middle), charge distribution of the signal after PMT background subtraction (bottom). The note '3&3 drops' stands for use of 3 and 3 drops of the catalysts RP-128 and MEKP, respectively, compared to the use of 2 and 2 drops of RP-128 and MEKP for all other polystyrene samples.

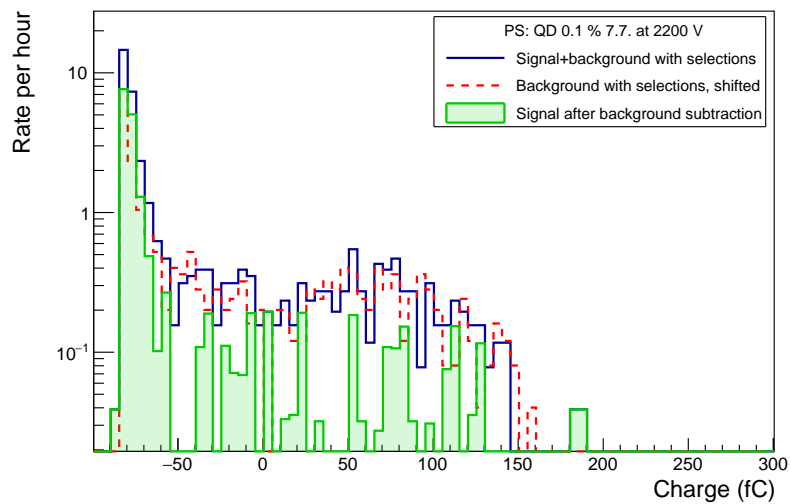
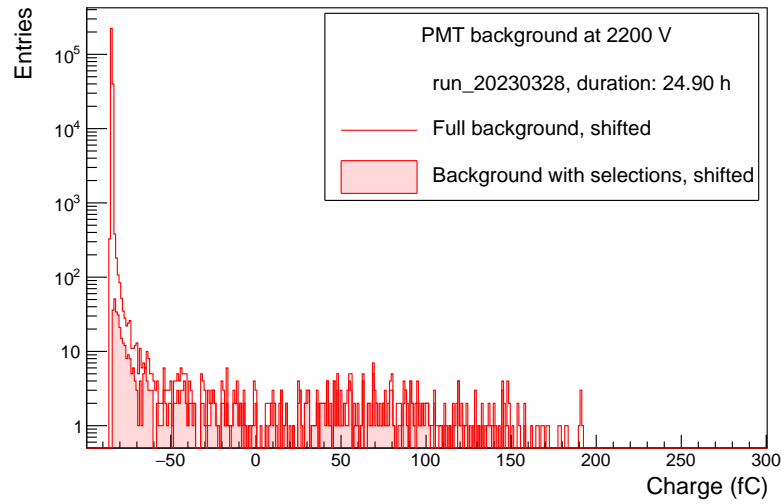
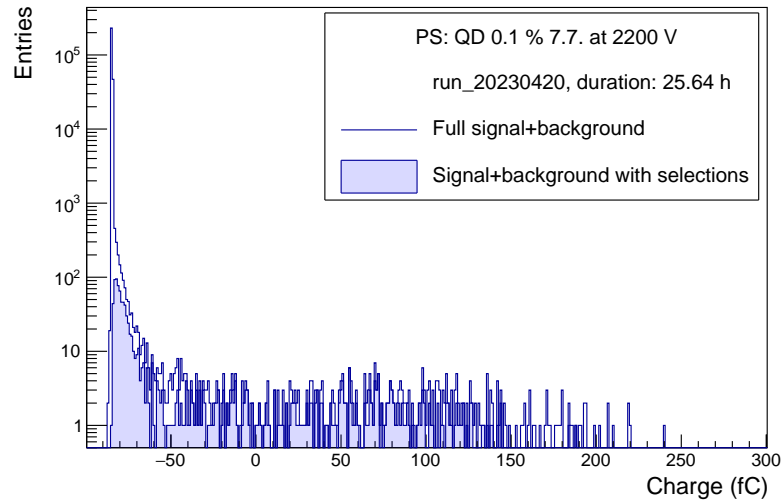


Figure B.3: Charge distribution for the QD 0.1 % 7.7. sample at 2200 V: signal+background (top), PMT background only (middle), charge distribution of the signal after PMT background subtraction (bottom).

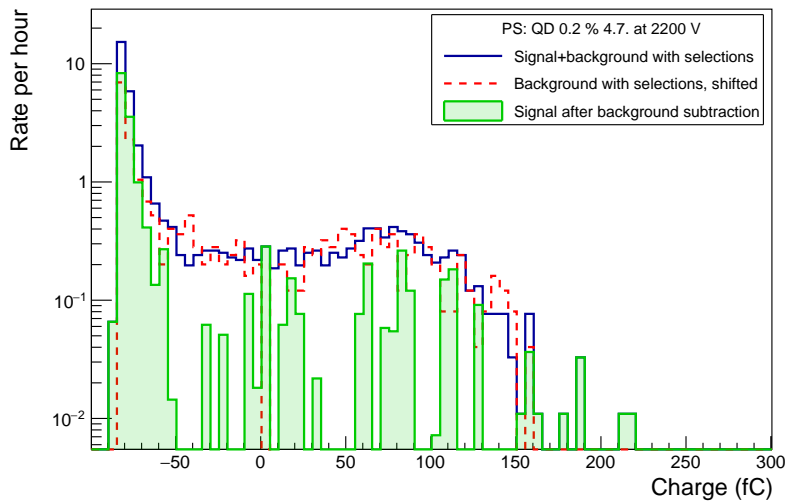
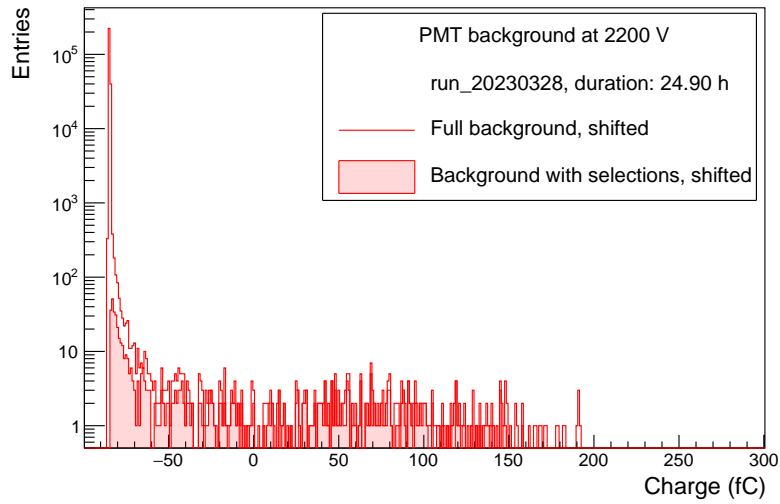
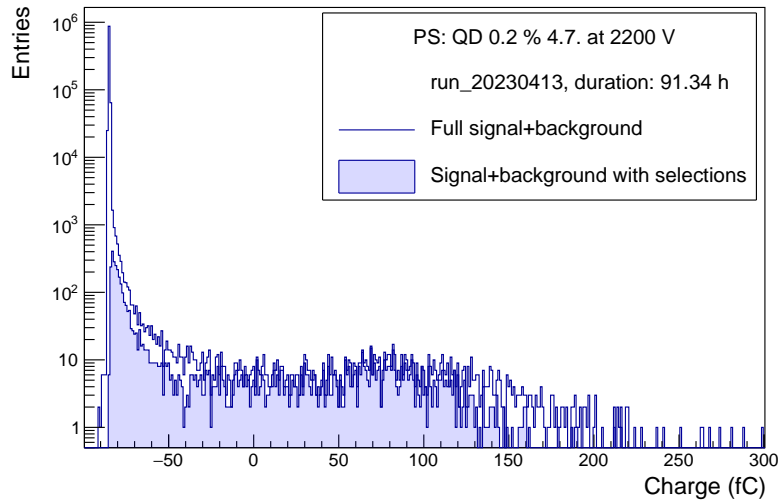


Figure B.4: Charge distribution for the QD 0.2 % 4.7. sample at 2200 V: signal+background (top), PMT background only (middle), charge distribution of the signal after PMT background subtraction (bottom).

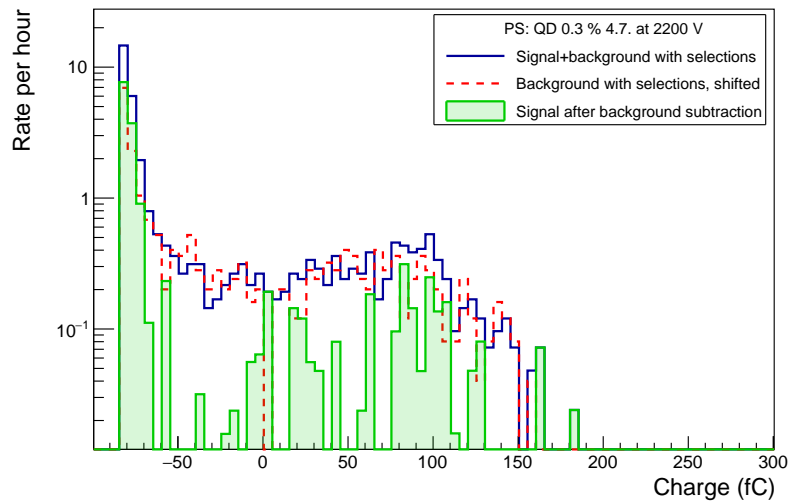
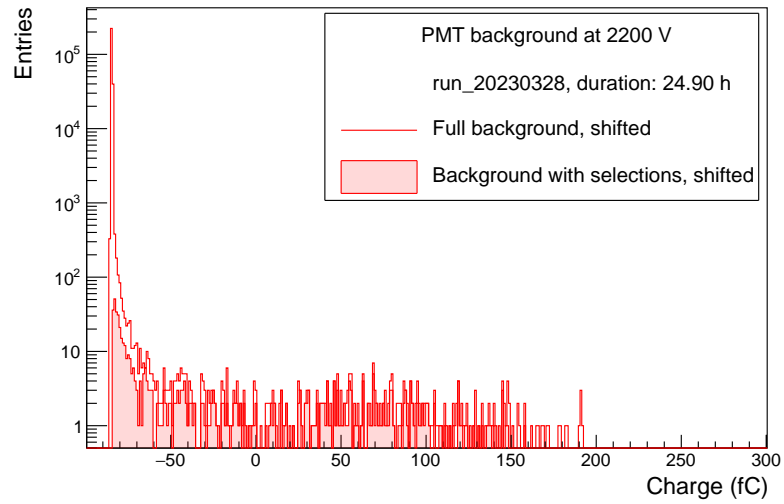
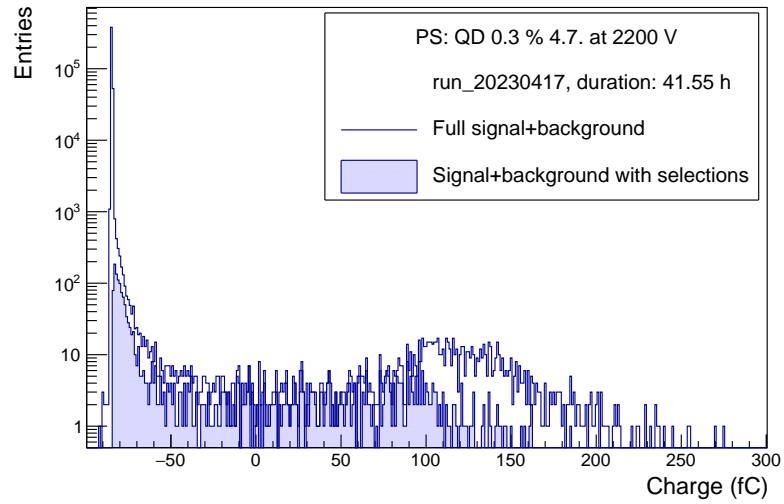


Figure B.5: Charge distribution for the QD 0.3 % 4.7. sample at 2200 V: signal+background (top), PMT background only (middle), charge distribution of the signal after PMT background subtraction (bottom).

Appendix C

Custom-made scintillator characterisation: silicone matrix

Table C.1 contains the full data of the characterisation of the silicone matrix samples. For the measurement of the silicone samples, the module sampleA with the PMT DA1417 was used. The supply voltage of the PMT was either 1800 V or 2000 V as denoted in the table. Depending on the supply voltage, a different set of parameters was used for the data analysis, such as the background run, the binning, and the charge window used for the integration of the events relevant for the effective rate calculation.

For runs at 1800 V, the used background run that was subtracted from the data was the run 0328. The charge interval for the analysis was chosen as $[-99.5, 200.5]$ with 300 bins. In order to count the number of entries and subsequently the effective rate, a minimum charge threshold of -53 fC was set. To show the resulting signal spectra after the background subtraction, the distributions were rebinned with $N_{rebin} = 5$.

Regarding the measurements at supply voltages of 2000 V, the used background run was 0322. The charge interval for the analysis was increased to $[-99.5, 300.5]$ with 400 bins. As the tail of the pedestal charge measured by the PMTs at higher voltages is wider, the minimum charge threshold for the integration was shifted to -42 fC. The rebinning constant stayed the same as for 1800 V, i.e. $N_{rebin} = 5$.

Characterised sample	HV	run ID	$R_{\text{eff,S+B}}$ (1/h)	$R_{\text{eff,B}}$ (1/h)	R_{SB}
NO QD NO PPO 12.7.	1800	0217	25.5 ± 0.6	6.8 ± 0.5	3.74 ± 0.30
NO QD PPO 1 % 12.7.	1800	0216	26.5 ± 1.0	6.8 ± 0.5	3.88 ± 0.33
QD 0.005 % NO PPO 7.7.	1800	0331	10.1 ± 0.4	6.8 ± 0.5	1.48 ± 0.13
QD 0.01 % PPO 1 % 6.7.	1800	0224	8.9 ± 0.4	6.8 ± 0.5	1.31 ± 0.11
NO QD NO PPO 12.7.	2000	0420	28.0 ± 1.0	8.4 ± 0.4	3.35 ± 0.21
NO QD PPO 1 % 12.7.	2000	0419	30.7 ± 1.1	8.4 ± 0.4	3.67 ± 0.23

Table C.1: Characterisation results of the silicone matrix samples, where the characterised sample is described, HV denotes the supply voltage (module sampleA), run ID marks the identification of the run with the sample, $R_{\text{eff,S+B}}$ denotes the effective rate of muons per hour for measurement with the sample, $R_{\text{eff,B}}$ denotes the effective rate of muons per hour for the background measurement with the PMT only, and R_{SB} is the ratio of the signal to background effective rates.

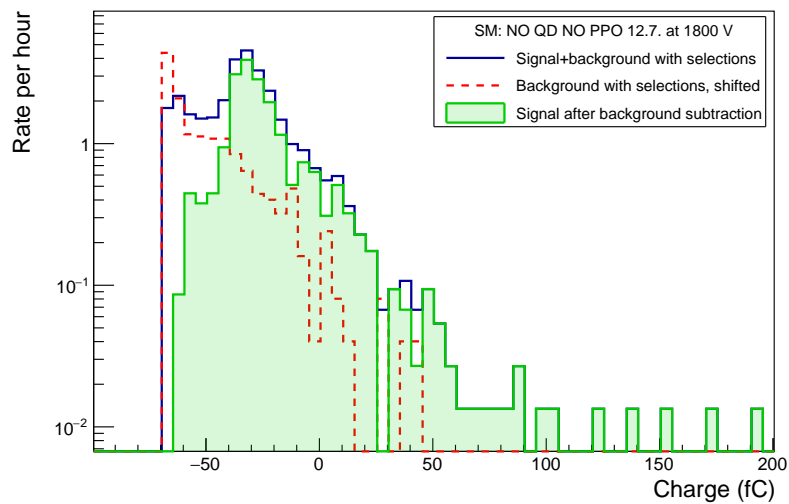
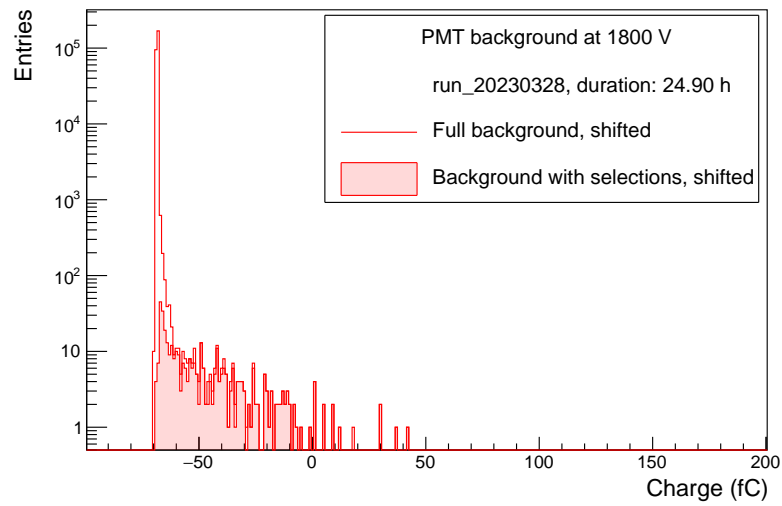
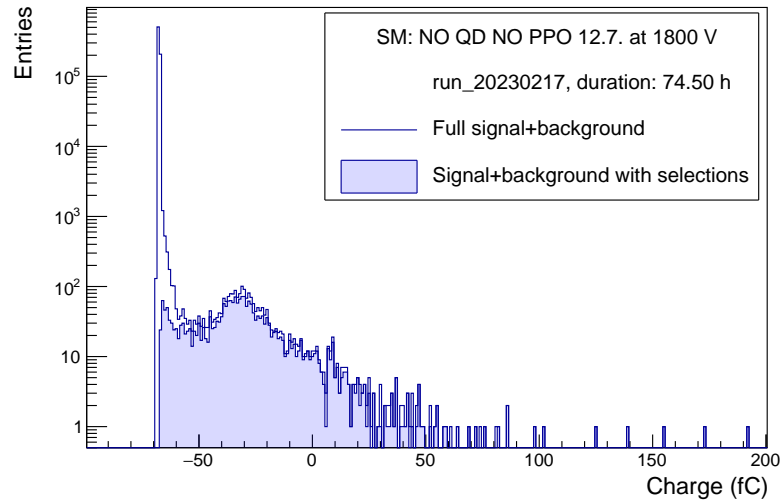


Figure C.1: Charge distribution for the NO QD NO PPO 12.7. sample at 1800 V: signal+background (top), PMT background only (middle), charge distribution of the signal after PMT background subtraction (bottom).

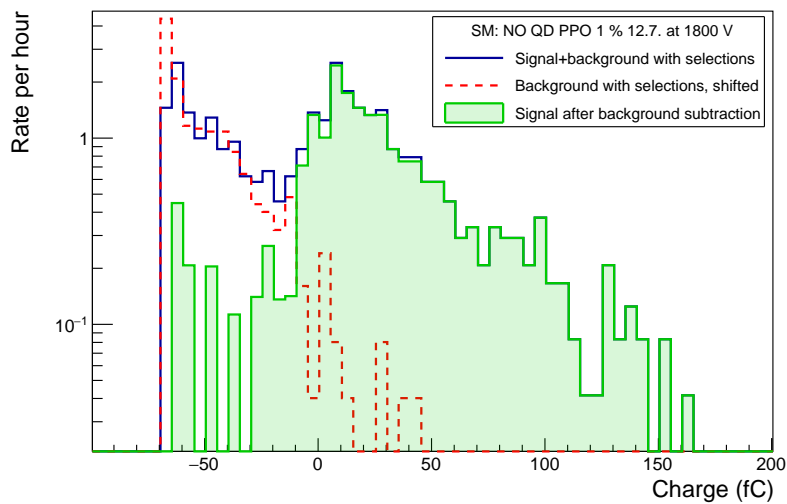
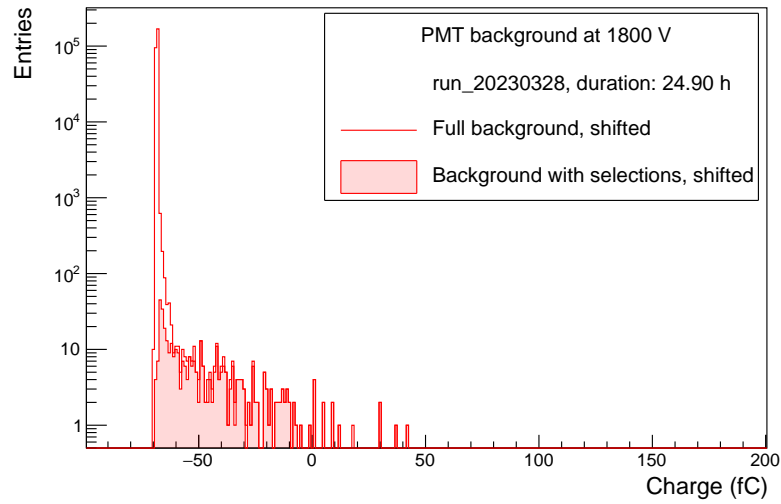
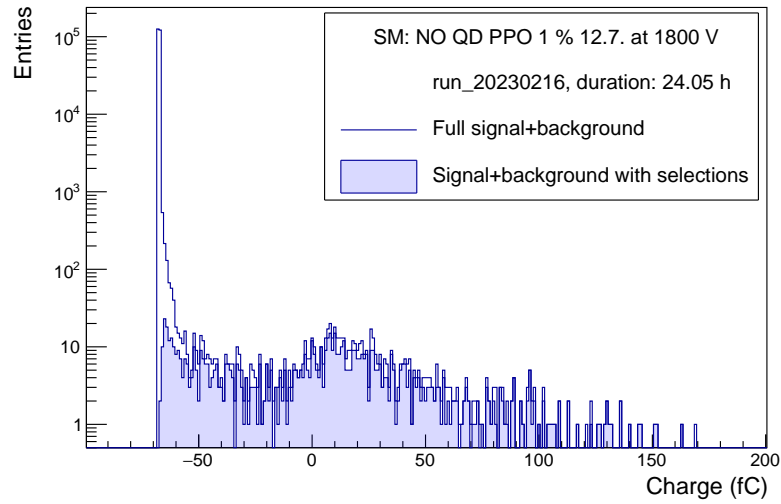


Figure C.2: Charge distribution for the NO QD PPO 1 % 12.7. sample at 1800 V: signal+background (top), PMT background only (middle), charge distribution of the signal after PMT background subtraction (bottom).

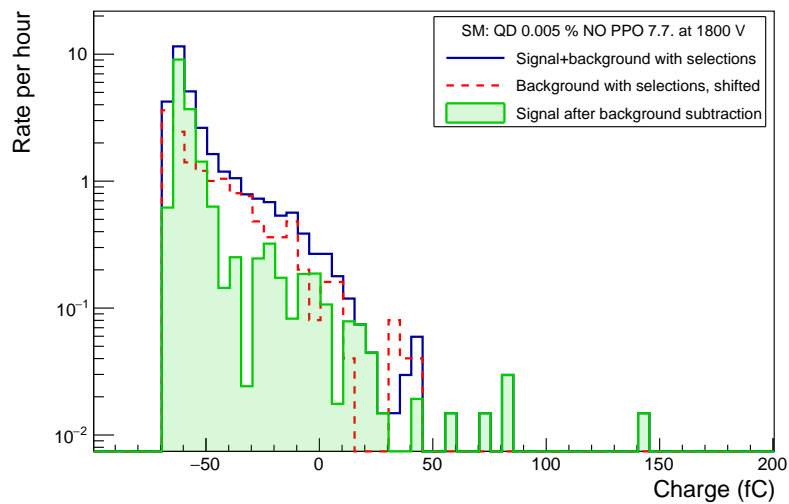
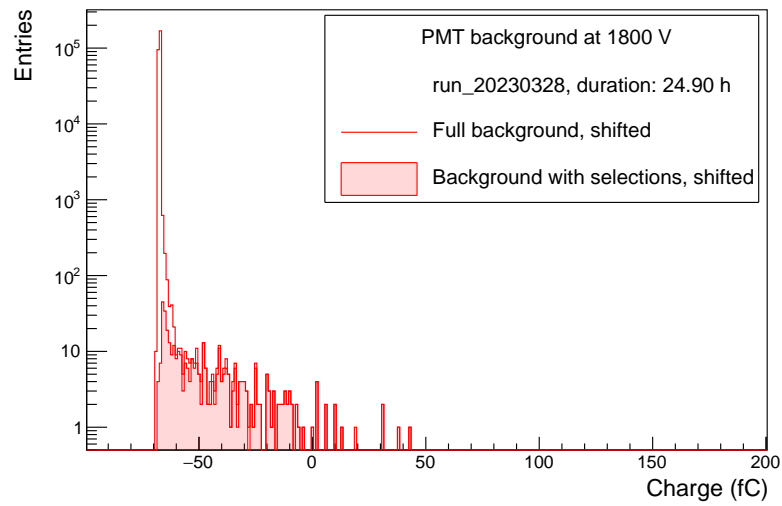
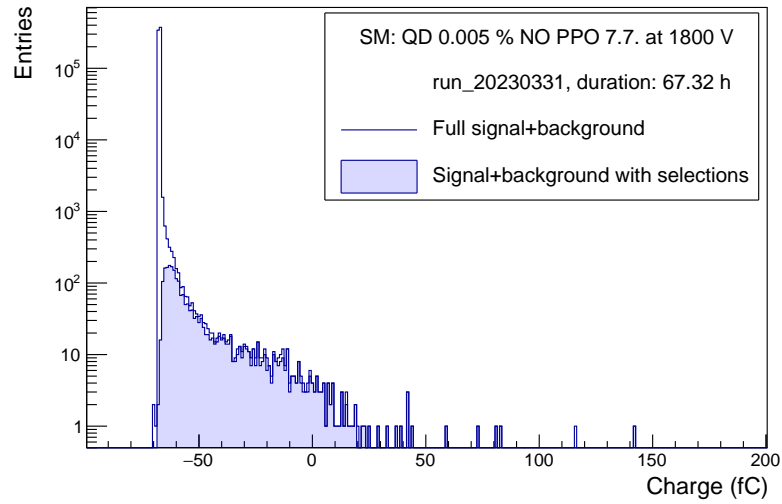


Figure C.3: Charge distribution for the QD 0.005 % NO PPO 7.7. sample at 1800 V: signal+background (top), PMT background only (middle), charge distribution of the signal after PMT background subtraction (bottom).

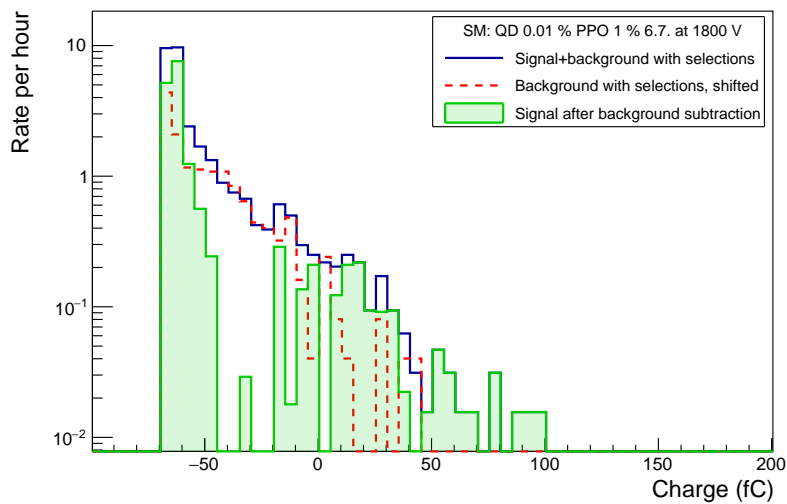
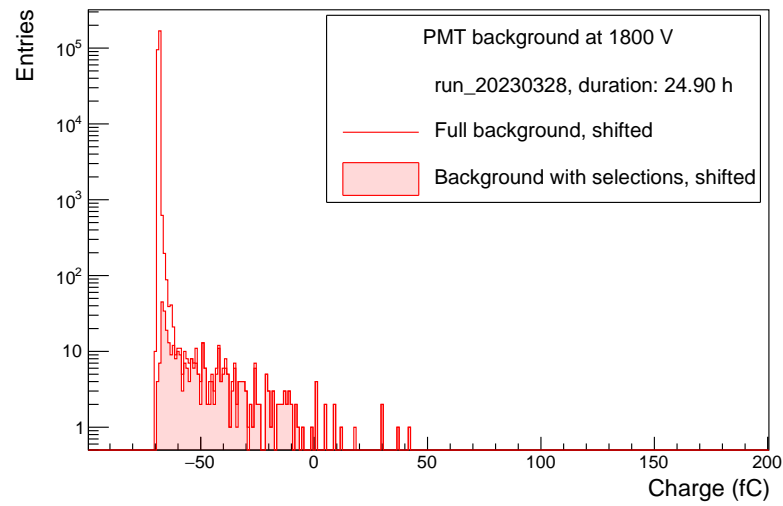
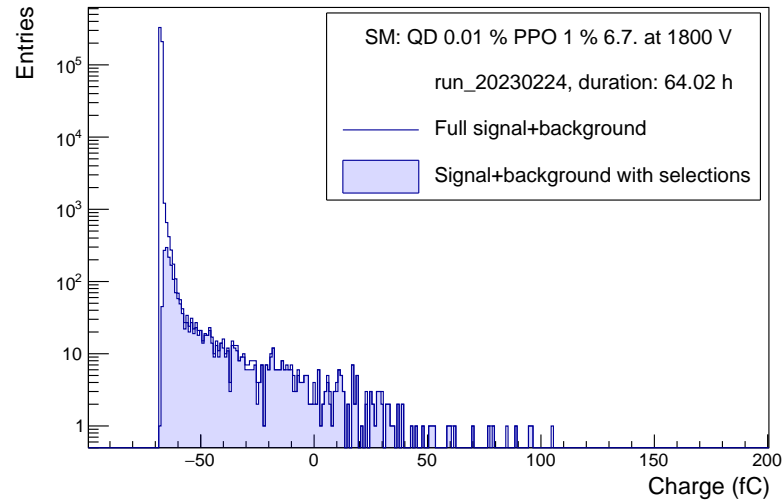


Figure C.4: Charge distribution for the QD 0.01 % PPO 1 % 6.7. sample at 1800 V: signal+background (top), PMT background only (middle), charge distribution of the signal after PMT background subtraction (bottom).

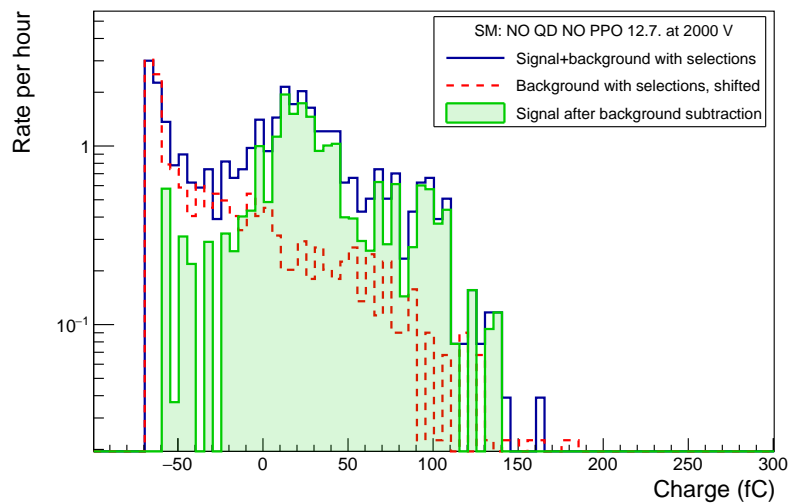
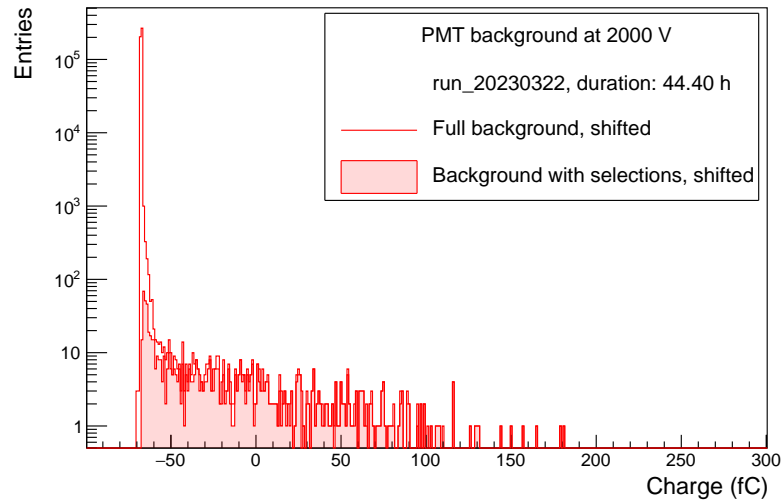
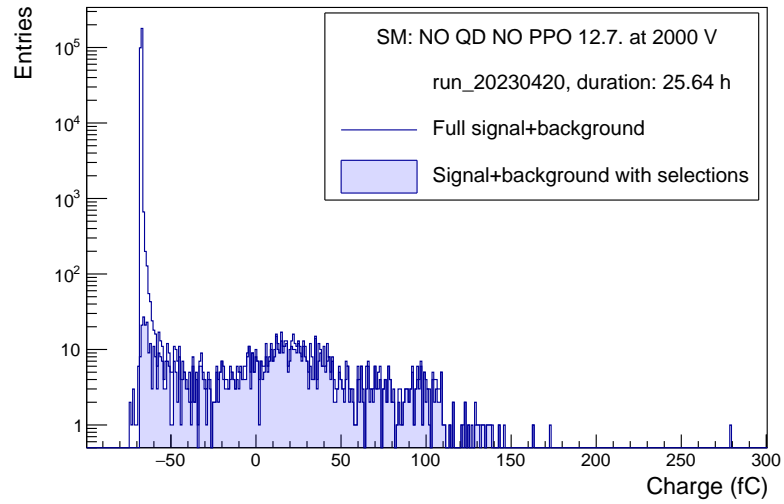


Figure C.5: Charge distribution for the NO QD NO PPO 12.7. sample at 2000 V: signal+background (top), PMT background only (middle), charge distribution of the signal after PMT background subtraction (bottom).

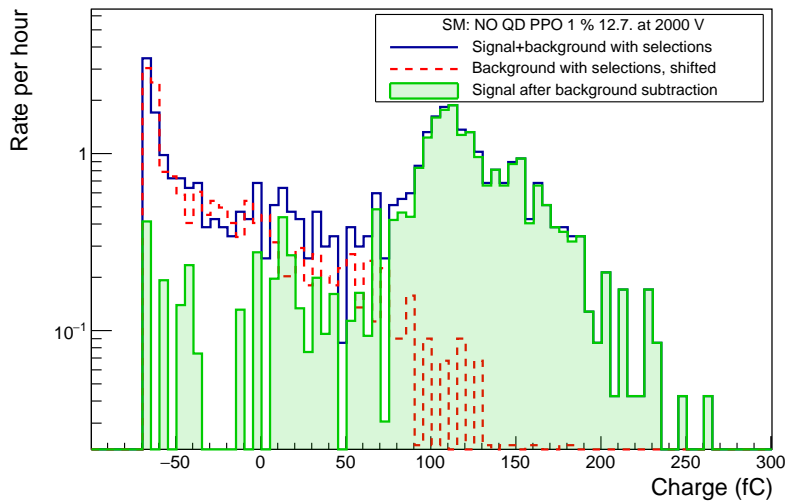
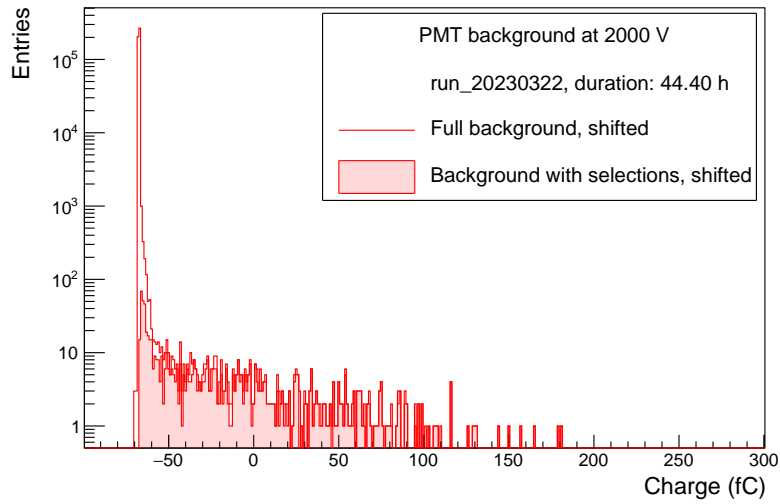
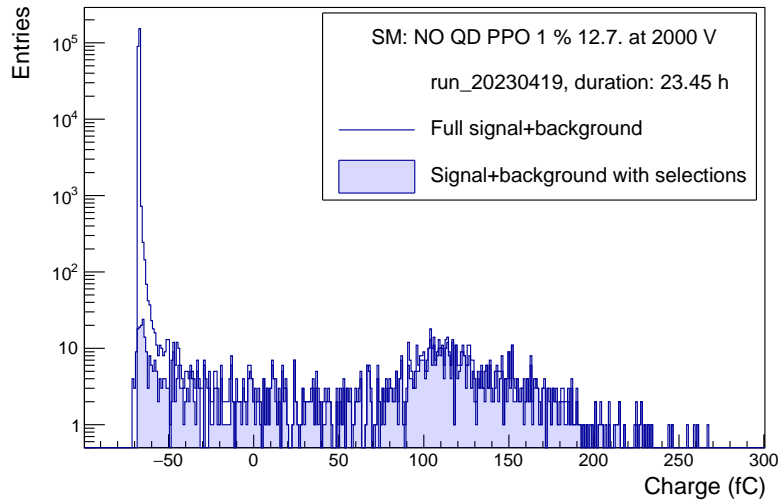


Figure C.6: Charge distribution for the NO QD PPO 1 % 12.7. sample at 2000 V: signal+background (top), PMT background only (middle), charge distribution of the signal after PMT background subtraction (bottom).

Appendix D

FDD performance: crosstalk test

During this test, it is key to see the effect of the induced signal in a signal cable of one of the channels on the other channels of the FDD. The set-up is the following: the LCS irradiates all of the PMTs, but only one PMT is supplied with voltage. It is then recorded what are the time and charge distributions for this channel and all of the other channels on the same side of the FDD. The test is done for all 16 detector channels as well as for both of the reference PMTs. The operational high voltage (Oper. HV) is summarised in Table D.1, it is chosen as the nominal high voltage (Nom. HV) + 200 V.

The results of the crosstalk test are shown in Fig. D.1. One can see that the signal in the fourth channel (Ch3) induced crosstalk in 3 other channels of the detector. This phenomenon is of course undesirable, so a metal shielding in a form of a mesh tape was installed around all of the signal cables. The result of the test after installation of the shielding is in Fig. D.2. It can be seen, that the induced charge in the other channels disappeared, however, the collected charge during the test after the installation of the shielding seems to be much lower. This is not yet explained. One reasoning could be the use of different FEE settings, such as the intensity of the laser, during the tests, but both of the test were performed with the same settings. To avoid this in the future, the reference PMT for the LCS can be switched on to measure the real-time laser intensity, which can be later compared.

Side	Layer	Quad.	Channel	Serial no.	Nom. HV	Oper. HV
FDD-C	0	0	FDDC_0_0	DA1586	1250	1450
		1	FDDC_0_1	DA1592	1330	1530
		2	FDDC_0_2	DA1574	1220	1420
		3	FDDC_0_3	DA1596	1240	1440
	1	0	FDDC_1_0	DA1555	1225	1425
		1	FDDC_1_1	DA1566	1170	1370
		2	FDDC_1_2	DA1595	1290	1490
		3	FDDC_1_3	DA1588	1385	1585
	Reference		FDDC_Ref	DA1427	1000	1200
FDD-A	2	0	FDDA_2_0	DA1562	1170	1370
		1	FDDA_2_1	DA1564	1160	1360
		2	FDDA_2_2	DA1603	1290	1490
		3	FDDA_2_3	DA1563	1180	1380
	3	0	FDDA_3_0	DA1551	1205	1405
		1	FDDA_3_1	DA1550	1205	1405
		2	FDDA_3_2	DA1593	1245	1445
		3	FDDA_3_3	DA1580	1430	1630
	Reference		FDDA_Ref	–	1200	1400

Table D.1: Summary of the layout of the channels within the FDD including the serial numbers of the corresponding PMTs and their nominal high voltage used during the data-taking with pp collisions (Nom. HV) and the operational voltage used for the electrical crosstalk test (Oper. HV).

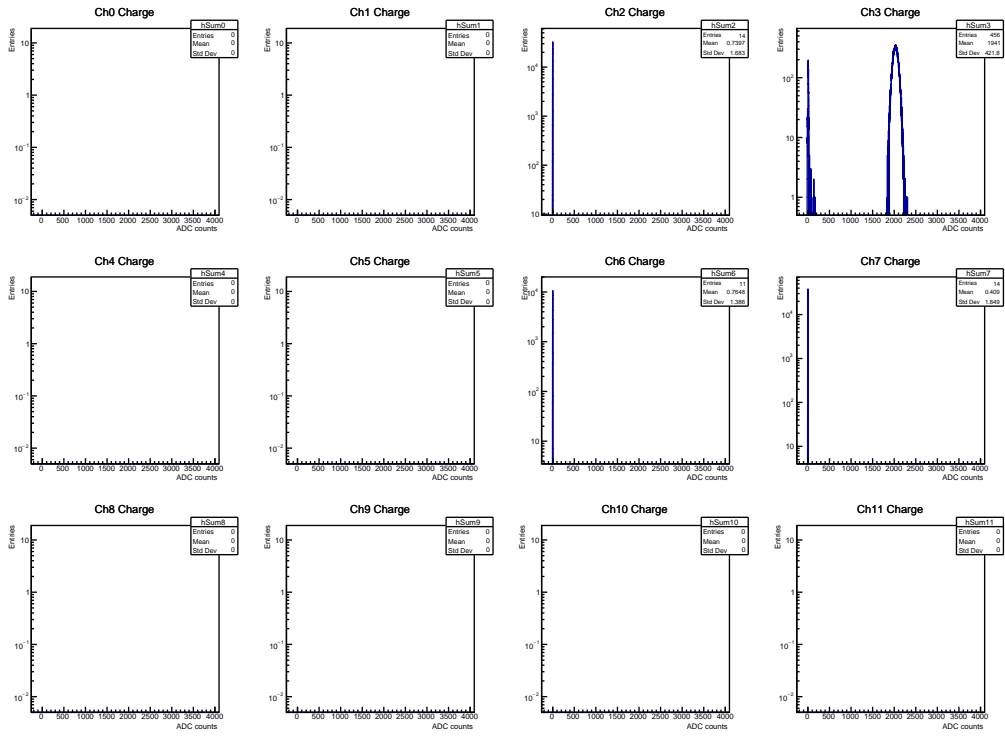


Figure D.1: Charge distribution for FDD-A side during the electrical crosstalk test before the installation of a metal shielding. Special attention should be paid to channels 2, 6 and 7, where a signal is induced because of the electrical crosstalk.

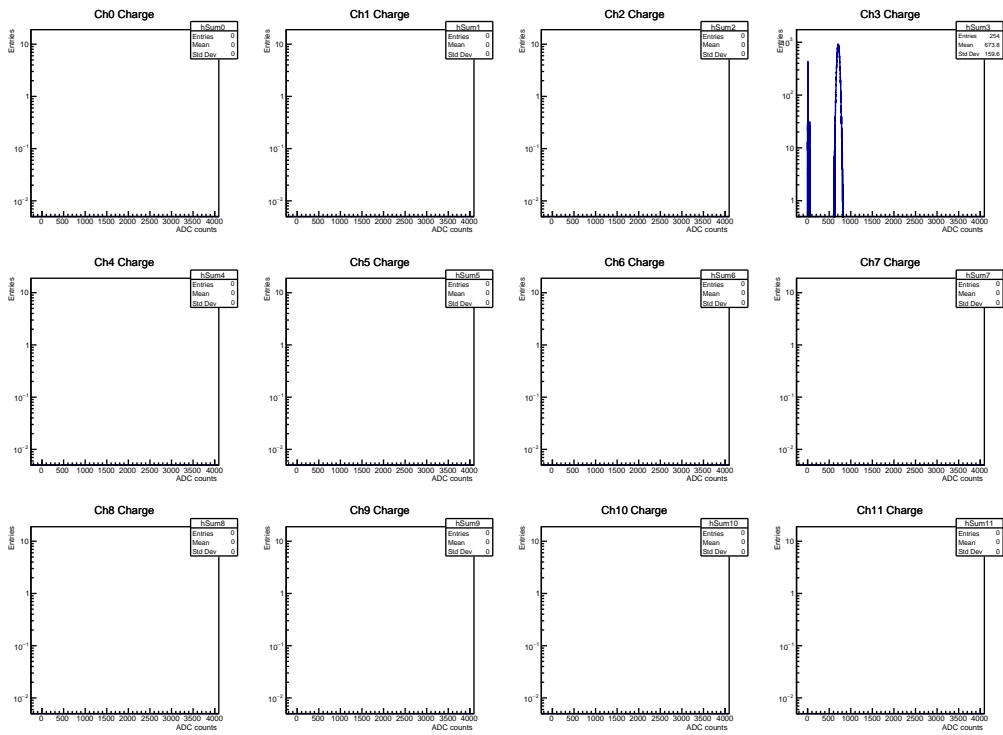


Figure D.2: Charge distribution for FDD-A side during the electrical crosstalk test after the installation of a metal shielding.